CO_2 Reduction Reaction in a Modified Zero-Gap Electrolyzer

Zur Erlangung des akademischen Grades einer
DOKTORIN DER INGENIEURWISSENSCHAFTEN (DR.-ING.)

von der KIT-Fakultät für Chemieingenieurwesen und Verfahrenstechnik des
Karlsruher Instituts für Technologie (KIT)
genehmigte

DISSERTATION

von
M. Sc. Siyu Zhong
aus Hunan, China

Tag der mündlichen Prüfung: 30.09.2025

Erster Gutachter: Prof. Dr.-Ing. Roland Dittmeyer
Zweitgutachterin: Prof. Dr. Francesca Toma

Acknowledgments

I would like to express my sincere gratitude to all those who supported me throughout my doctoral studies and contributed to the successful completion of this dissertation.

First and foremost, I would like to thank my supervisor, Prof. Dittmeyer, for his continuous guidance, encouragement, and trust. His scientific vision and strategic foresight laid the foundation of my work on the CO_2RR project. I am particularly grateful for his openness to discussion and his constructive advice, especially during challenging phases of the project, which helped maintain both scientific progress and personal motivation.

I am deeply grateful to all colleagues at the Institute of Micro Process Engineering (IMVT) for the highly collaborative and supportive working environment. My sincere thanks go to the group leaders Peter, Alex, and Micha for their clear guidance and valuable technical insights. I particularly thank Paul, David, Sara, Timo, Xiang, Dongxu, Gen, and Laura for their continuous assistance with experimental setups and troubleshooting, especially during demanding GC measurements. I also thank Mr. Lambach and the ADD team for designing and manufacturing the reactor system, which exceeded expectations and enabled reliable experimental operation. Furthermore, I would like to acknowledge Sijia, Mery, Melis, Mertcan, Mo, and Lutong for many encouraging discussions that provided motivation throughout this work. I also gratefully acknowledge the contributions of the students Mengtian, Ilyes, and Shengzhi, whose participation significantly accelerated laboratory progress. Special thanks go to Mrs. Krämer and Lara for their efficient and reliable administrative support.

Financial support from the German Helmholtz Association within the program Materials and Technologies for the Energy Transition (MTET) (Theme 3: Chemical Energy Carriers) and the Helmholtz Initiative Climate Adaptation and Mitigation (HI-CAM II, Cluster I, Net Zero 2050) is gratefully acknowledged. I further thank the Karlsruhe House of Young Scientists (KHYS) for supporting my research visits to the University of Alberta and the University of Sydney. I am grateful to the professors and

researchers at both institutions for their valuable scientific discussions and openness to collaboration, which led to a joint publication. I sincerely thank all co-authors for their commitment and contributions. In addition, I thank Prof. Simon Thiele and his research group at the Helmholtz Institute Erlangen Nürnberg for Renewable Energy (HIERN) for hosting me and for their support in addressing experimental challenges. I also acknowledge Dr. Michael Zimmermann for SEM and EDS measurements and Dr. Peter G. Weidler for XRD measurements.

I would also like to thank my friends, especially Daniel, for their companionship and support, which greatly enriched my time in Germany beyond academic life. Finally, I express my deepest gratitude to Ms. Li for her selfless maternal love and patience.

Abstract

The global transition toward carbon neutrality hinges on innovative technologies that efficiently reduce CO_2 emissions. Electrochemical reduction of CO_2 presents a promising pathway for producing valuable chemical feedstocks and thereby addressing climate change. This doctoral work explores novel strategies to optimize CO_2RR efficiency, focusing on enhancing energy conversion, maximizing product selectivity, and addressing the operational challenges associated with electrolyzers. Through a series of well-designed experiments and novel methodologies, this research advances the understanding of key parameters such as temperature, pressure, electrolyte composition, and catalyst performance in shaping the efficiency of CO_2 electroreduction systems.

At the core of this work is the optimization of electrochemical reactor design and reaction process. Zero-gap electrolyzers, employing anion exchange membrane (AEM) or cation exchange membrane (CEM) systems, serve as the primary platform for investigating the effects of operating conditions on CO_2 reduction. Under alkaline conditions with 1 M KOH, the AEM system demonstrated remarkable energy efficiency, achieving up to 48% at a current density of 100 mA/cm^2, while maintaining Faradaic efficiency for CO (FE_{CO}) above 90%. In contrast, the CEM system provided valuable insights into the role of electrolyte concentration, with energy efficiencies improving to 32% under a 2 M $KHCO_3$ solution. This finding underscores the significance of tailoring electrolyte conditions to enhance CO_2RR performance.

Catalyst selection and modification were pivotal in steering the reaction pathways toward desired products. Silver catalysts were predominantly used for CO production, achieving consistent FE_{CO} above 90% across varying operational conditions. Meanwhile, copper-based catalysts in the AEM-MEA systems enabled the production of higher-value C_{2+} products. However, their efficiency was constrained by competing hydrogen evolution reactions and limited C_{2+} Faradaic efficiency (26%-38%) in alkaline environments. In addition, tandem Cu/Ag catalysts, enhanced CO selectivity but reduced C_2-C_3 product yields due to the rapid desorption of CO intermediates. This highlights the

trade-off between selectivity and productivity, offering valuable insights into catalyst design.

Operating conditions were systematically varied to enhance reaction performance, including temperature, pressure, and electrolyte concentration. Elevated temperatures and pressures proved crucial in improving both reaction kinetics and thermodynamics. For instance, in AEM-MEA systems, energy efficiency improved by over 10% when operating at high temperatures and under pressure compared to ambient conditions. In CEM-MEA systems, energy efficiency increased from 28% to 37% at 75 °C, and pressurization (1-5 bar) led to nearly 95% FE_{CO} and energy efficiencies stabilizing at around 35%. These findings reveal that optimizing operational conditions is essential for scaling up CO_2RR processes to meet industrial demands. However, challenges such as carbonate precipitation and membrane fouling remain, requiring further innovations in reactor design and material development.

The results of this study demonstrate the significant potential of CO_2RR as a sustainable approach for carbon dioxide utilization. By optimizing reactor design, catalyst performance, and operational conditions, this research contributes to the ongoing efforts to reduce CO_2 emissions while producing valuable chemical products. The work provides a comprehensive framework for developing more efficient, stable, and scalable CO_2 electroreduction technologies, with the promise of advancing carbon-neutral solutions in the energy and chemical sectors. Ultimately, the methodologies and findings presented in this thesis provide practical insights for the next generation of electrochemical systems that can play a pivotal role in mitigating climate change and promoting a sustainable future.

Kurzfassung

Der globale Übergang zur Klimaneutralität hängt maßgeblich von innovativen Technologien ab, die CO_2-Emissionen effizient reduzieren. Die elektrochemische Reduktion von CO_2 bietet einen vielversprechenden Ansatz, um wertvolle chemische Grundstoffe nachhaltig herzustellen und dadurch den Klimawandel zu bekämpfen. Diese Doktorarbeit untersucht neuartige Strategien zur Optimierung der CO_2-Reduktions-Effizienz (CO_2RR), wobei der Fokus auf der Steigerung der Energieumwandlung, der Maximierung der Produktselektivität sowie der Bewältigung betrieblicher Herausforderungen in Elektrolyseuren liegt. Durch eine Reihe sorgfältig konzipierter Experimente und innovativer Methoden trägt diese Forschung zum besseren Verständnis entscheidender Parameter wie Temperatur, Druck, Elektrolytzusammensetzung und Katalysatorleistung bei, die die Effizienz von CO_2-Elektroreduktionssystemen beeinflussen.

Im Zentrum dieser Arbeit steht die Optimierung des elektrochemischen Reaktordesigns und des Reaktionsprozesses. Nullspalt-Elektrolyseure mit Anionenaustauschmembranen (AEM) order Kationenaustauschmembranen (CEM) dienen als primäre Plattformen, um den Einfluss der Betriebsbedingungen auf die CO_2-Reduktion zu untersuchen. Unter alkalischen Bedingungen mit 1 M KOH zeigte das AEM-System eine bemerkenswerte Energieeffizienz von bis zu 48 % bei einer Stromdichte von 100 mA/cm^2, wobei die Faraday-Effizienz für CO (FE_{CO}) über 90 % lag. Im Gegensatz dazu lieferte das CEM-System wertvolle Erkenntnisse zur Rolle der Elektrolytkonzentration, wobei die Energieeffizienz in einer 2 M $KHCO_3^-$Lösung auf 32 % anstieg. Dieser Befund unterstreicht die Bedeutung einer maßgeschneiderten Elektrolytzusammensetzung zur Verbesserung der CO_2RR-Leistung.

Die Auswahl und Modifikation von Katalysatoren spielten eine entscheidende Rolle bei der Steuerung der Reaktionspfade hin zu den gewünschten Produkten. Silberkatalysatoren wurden vorwiegend für die CO-Erzeugung eingesetzt und erreichten unter verschiedenen Betriebsbedingungen konstant eine FE_{CO} von über 90 %.

Kupferbasierte Katalysatoren in AEM-MEA-Systemen ermöglichten dagegen die Produktion höherwertiger C_{2+}-Produkte. Allerdings wurde ihre Effizienz durch konkurrierende Wasserstoffentwicklungsreaktionen und eine begrenzte C_{2+}-Faraday-Effizienz (26–38 %) in alkalischer Umgebung eingeschränkt. Tandem-Kupfer/Silber-Katalysatoren steigerten zwar die CO-Selektivität, reduzierten jedoch die Ausbeute an C_2–C_3-Produkten aufgrund der schnellen Desorption von CO-Zwischenprodukten. Dies verdeutlicht den Zielkonflikt zwischen Selektivität und Produktivität und liefert wertvolle Erkenntnisse für das Katalysatordesign.

Um die Reaktionsleistung zu verbessern, wurden die Betriebsbedingungen systematisch variiert, darunter Temperatur, Druck und Elektrolytkonzentration. Erhöhte Temperaturen und Druck erwiesen sich als entscheidend für die Verbesserung von Reaktionskinetik und Thermodynamik. Beispielsweise stieg die Energieeffizienz in AEM-MEA-Systemen unter erhöhten Temperaturen und Druck im Vergleich zu Umgebungsbedingungen um über 10 %. In CEM-MEA-Systemen erhöhte sich die Energieeffizienz bei 75 °C von 28 % auf 37 %, und ein Druck von 1–5 bar führte zu einer FE_{CO} von nahezu 95 % bei stabiler Energieeffizienz von etwa 35 %. Diese Ergebnisse zeigen, dass die Optimierung der Betriebsbedingungen entscheidend ist, um CO_2RR-Prozesse für industrielle Anforderungen hochzuskalieren. Dennoch bleiben Herausforderungen wie Karbonat-Ausfällungen und Membranverschmutzung bestehen, die weitere Innovationen im Reaktordesign und in der Materialentwicklung erfordern.

Die Ergebnisse dieser Studie demonstrieren das beträchtliche Potenzial der CO_2RR als nachhaltigem Ansatz zur Kohlenstoffdioxidnutzung. Durch die Optimierung von Reaktordesign, Katalysatorleistung und Betriebsbedingungen leistet diese Forschung einen Beitrag zu den laufenden Bemühungen, CO_2-Emissionen zu reduzieren und gleichzeitig wertvolle Chemikalien zu produzieren. Die Arbeit liefert einen umfassenden Rahmen für die Entwicklung effizienterer, stabilerer und skalierbarer CO_2-Elektroreduktionstechnologien, die klimaneutrale Lösungen in der Energie- und Chemieindustrie vorantreiben können. Letztlich bieten die in dieser Dissertation vorgestellten Methoden und Erkenntnisse praktische Ansatzpunkte für die nächste

Generation elektrochemischer Systeme, die eine Schlüsselrolle bei der Bekämpfung des Klimawandels und der Förderung einer nachhaltigen Zukunft spielen können.

Abbreviations and symbols

CCUS	Carbon capture, utilization, and storage
CEM	Cation exchange membrane
AEM	Anion exchange membrane
OER	Oxygen evolution reaction
CO_2RR	CO_2 reduction reaction
PCET	Proton-coupled electron transfer
HER	Hydrogen evolution reaction
IEM	Ion exchange membrane
GDE	Gas diffusion electrode
GDL	Gas diffusion layer
PEM	Proton exchange membrane
MEA	Membrane electrode assembly
BPM	Bipolar membrane
P&ID	Process and instrumentation diagram
LSV	Linear sweep voltammetry
CP	Chronopotentiometry
CA	Chronoamperometry
EIS	Electrochemical impedance spectroscopy
FE	Faradaic efficiency
EE	Energy efficiency
MFC	Mass flow meter
HPLC	High-performance liquid chromatography
HTPEM	High-temperature proton exchange membrane

SHE	Standard hydrogen electrode
RHE	Reversible hydrogen electrode
XRD	X-ray diffraction
SEM	Scanning electron microscopy
EDS	Energy-dispersive spectroscopy
EDX	Energy dispersive X-ray spectroscopy
GC	Gas chromatography
TCD	Thermal conductivity detector
FID	Flame ionization detector
AWE	Alkaline water electrolysis
SOEC	Solid oxide electrolysis cells
DAC	Direct air capture
P2X	Power-to-X
CPET	Coordinated proton-electron transfer
PBI	Polybenzimidazole
DMAC	Dimethylacetamide

Nomenclature

A	Electrode area
F	Faradaic constant
FE	Faradaic efficiency
I	Current value
j	Current density
n	Number of electrons
V	Volume of electrolyte
m	Concentration of liquid product
Q_{total}	Total charge
Q_i	Electrons stored in the products
P	Pressure
R	Universal gas constant
E_{cell}	Cell voltage
E_{rev}	Thermodynamic voltage
E_{tn}	Thermoneutral voltage
v	Flow rate of CO_2 gas
x	Volume fraction of product
ΔS	Entropy change
ΔH	Enthalpy change
ΔG	Change of Gibbs free energy
barg	Bar gauge

Table of Contents

1 Introduction

1.1 Carbon dioxide reduction

1.1.1 CO_2 capture and utilization

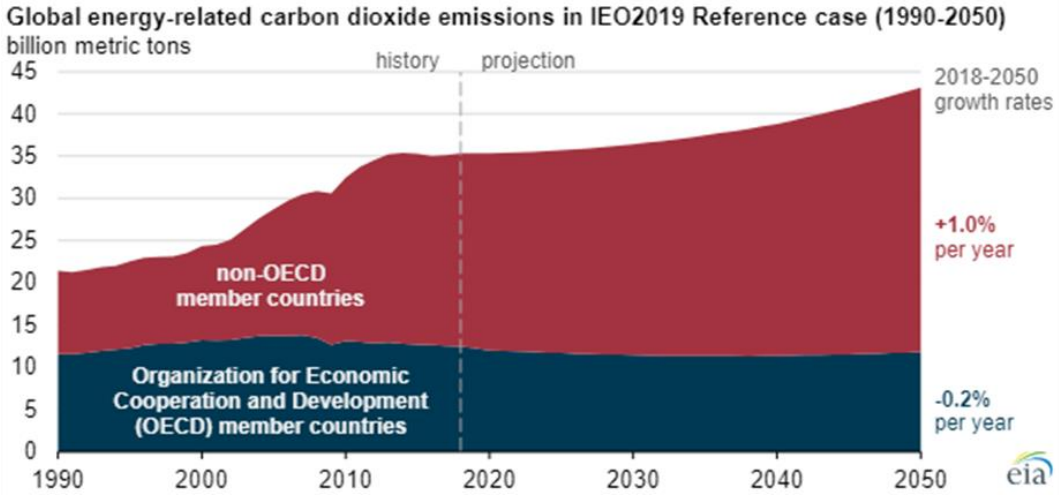

Figure 1.1: Projection from the U.S. Energy Information Administration that global CO_2 emissions will continue to grow in the coming decades [4].

With the continuous expansion of the economy and thriving urbanization, coupled with global population growth and increased affluence, human society continually demands more energy [1]. Fossil fuels such as coal, oil, and natural gas have consistently served as the primary sources of energy. However, the widespread use of these traditional energy sources, along with intensive agricultural and industrial activities, has led to the anthropogenic over-emission of greenhouse gases, including carbon dioxide [2]. As of May 2023, the global atmospheric CO_2 concentration has reached a record high of 424 ppm, surpassing the pre-industrial range of 180 to 280 ppm [3]. The U.S. Energy Information Administration (EIA) anticipates that in the coming decades, CO_2 emissions from global energy-related sources will continue to escalate. According to the EIA International Energy Outlook 2019 (IEO2019) in Figure 1.1, it is projected that from 2018 to 2050, global energy-related CO_2 emissions will increase by 0.6% annually [4]. If these

emissions continue to increase at the current rate without effective governance until the normal carbon cycle in nature is thoroughly disrupted, it will lead to irreversible changes in the climate and ecosystems. For example, the greenhouse effect has been intensifying over the past few decades, with each successive decade warmer than the previous one, according to data from the World Meteorological Organization (WMO) [5, 6]. This irreversible environmental impact has resulted in widespread ecological destruction, prompting an urgent need for sustainable development and energy transition.

In response to the escalating global greenhouse effect, 195 countries signed the Paris Agreement in 2015, marking the inception of a profoundly significant international accord [7]. The accord aims at a concerted global effort to address the challenges posed by greenhouse gas emissions and climate change. As stipulated by the agreement, nations pledged to take actions to ideally limit the global average temperature increase to within 1.5 °C, with a commitment to restrain it below the catastrophic 2°C. Simultaneously, endeavors are directed toward achieving carbon neutrality by 2050 [8]. This collective goal urgently calls for more proactive measures across diverse global sectors to expedite the reduction of greenhouse gas concentrations in the atmosphere, thereby reversing the trend of global climate change. To realize this objective, one of the pivotal measures involves reducing reliance on fossil fuels while actively seeking more renewable energy sources and pathways for the efficient utilization of carbon dioxide resources [9]. In this process, it is imperative to ensure the attainment of "zero carbon emissions" goals while fostering economic growth as Figure 1.2 shows [10]. This undertaking not only requires the impetus of technological advancements and innovation but also necessitates the establishment of cooperative mechanisms on a global scale, prompting collaborative efforts among nations to share resources and knowledge, ultimately realizing a more sustainable and environmentally friendly development path [11]. Only through coordinated global efforts can the threats of climate change be effectively addressed, paving the way for a healthier and more sustainable ecological environment for future generations [12].

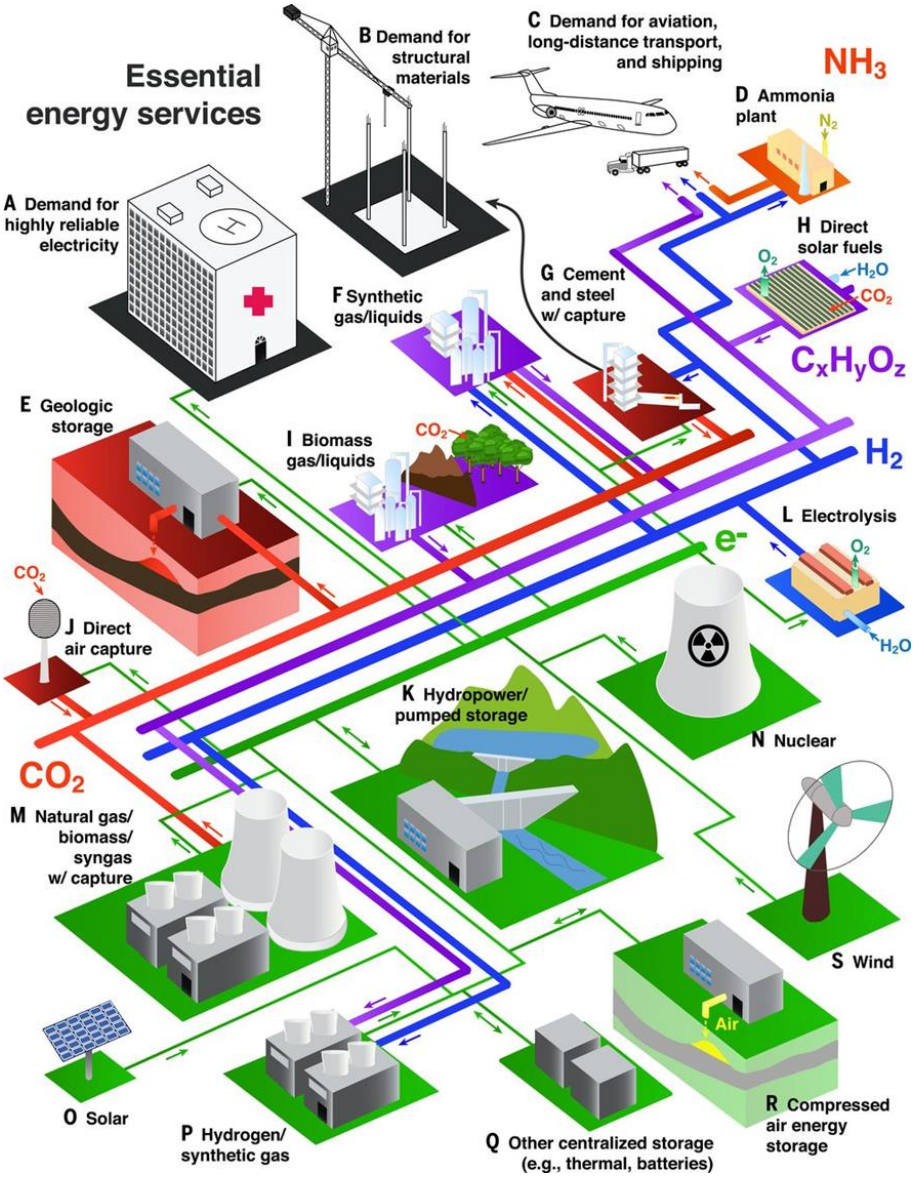

Figure 1.2: Diagram illustrating an integrated system capable of delivering vital energy services while ensuring a carbon-neutral impact on the atmosphere [10].

Given the current inability of global human activities to be completely free from the reliance on fossil fuels in the short term, utilizing natural resources and technological processes to extract carbon dioxide emissions from the atmosphere presents a viable pathway towards achieving carbon neutrality. Carbon capture, utilization, and storage (CCUS) technologies encompass various stages, including the separation of CO_2 from emission sources, conversion into valuable materials or fuels, transportation, and long-term subterranean storage for isolation from the atmosphere, as illustrated in Figure 1.3.

Of particular significance is CO_2 conversion technology, as it not only transforms CO_2 into valuable materials or fuels but also concurrently mitigates emissions. This field holds tremendous potential for future development [13].

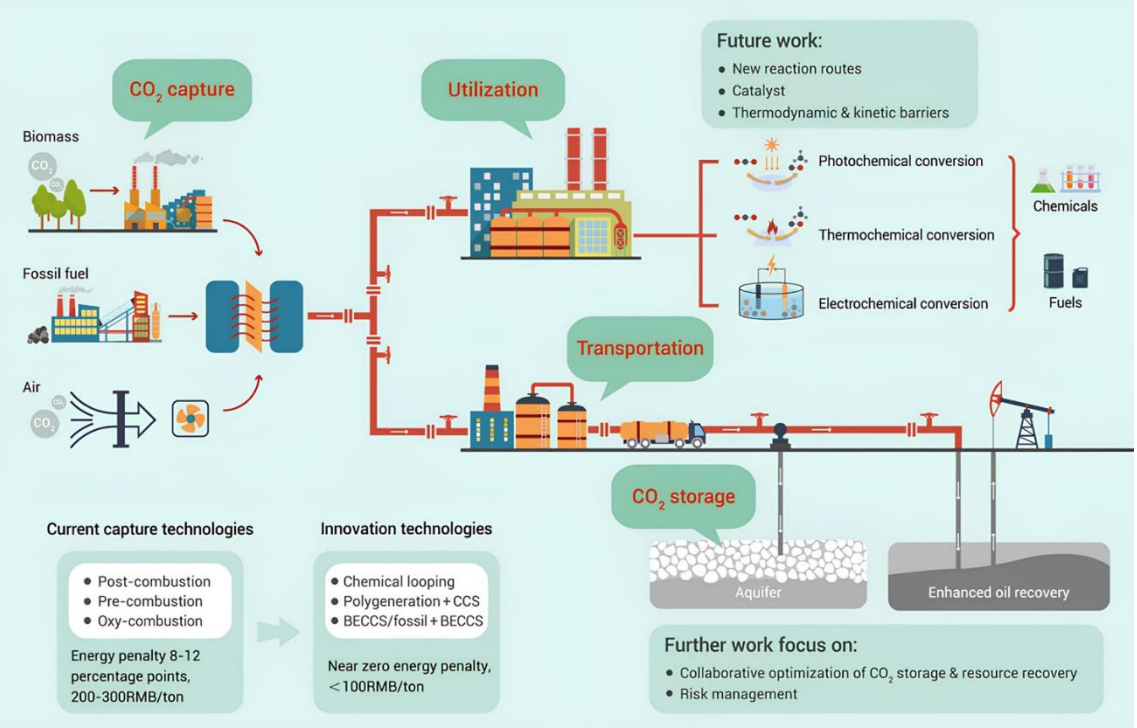

Figure 1.3: The roadmap for CO_2 capture, utilization, and storage technology development [11].

As an integral component of CCUS strategy, carbon utilization plays a crucial role in generating revenue streams sufficient to offset the costs associated with carbon capture. The direct chemical conversion of CO_2 refers to the process in which carbon dioxide, under specific conditions of temperature, pressure, and catalysis, is transformed into other high-value chemical substances [14]. In recent years, CO_2 reduction methods, including thermochemical catalysis [14], photochemical catalysis [15], electrochemical catalysis [16], enzymatic catalysis [17], and plasma-enhanced catalysis [18], have advanced in tandem and achieved progressive developments. These approaches have significantly progressed by mutually influencing each other.

The use of electricity allows for the reduction of carbon dioxide at the cathode of an electrolyzer, while oxygen is produced at the anode and released into the atmosphere [19]. This process of electrolysis technology effectively converts carbon dioxide into a useful product. By utilizing electricity as a renewable resource, the reduction of carbon dioxide is facilitated as an environmentally friendly and sustainable method. Compared to the demanding conditions of thermochemical CO_2 hydrogenation, the electrochemical carbon dioxide conversion process takes place under milder environmental conditions [14]. Furthermore, in contrast to photocatalytic processes with lower solar energy utilization efficiency, the electrochemical method allows for finer control of reaction rates and selectivity through applied voltage, making them easier to scale up [20]. The CO_2 reduction reaction (CO_2RR) utilizes water as a proton source, eliminating the need for an external H_2 supply. More importantly, the electrochemical CO_2 reduction pathway enables the integration of intermittent renewable energy and non-peak electricity storage into higher-priced and larger-scale chemicals and fuels, thereby closing the carbon cycle and reducing CO_2 emissions. This provides a viable approach to achieving sustainable energy and carbon neutrality.

1.1.2 Electrochemistry in decarbonization networks

The scientific community and industrial sectors are actively exploring Power-to-X technology, which facilitates the conversion of electrical power generated from renewable energy sources into various utilizable forms, including gases, liquids, or thermal energy, among others [21, 22], thereby enabling the production of chemical energy or synthetic energy carriers [23-25]. In such contexts, the production of fuels synthesized from clean electricity and carbon dioxide may represent an optimal approach for achieving a carbon-neutral economy [26]. This not only introduces novel possibilities for the efficient utilization of renewable energy sources but also contributes to advancing environmental conservation and sustainable development goals.

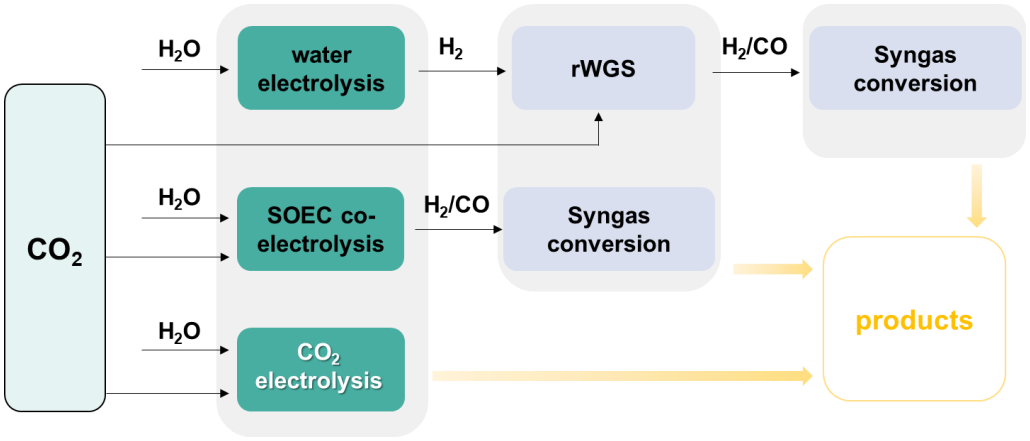

Figure 1.4: Different power-to-X process options for CO_2 conversion into products.

Figure 1.4 illustrates three distinct options for valorization of CO_2 via power-to-X (P2X) routes. The conventional pathway leads to the formation of syngas (a mixture of CO and H_2) and its derivatives. The primary routes include a) the generation of green hydrogen through water or steam electrolysis, followed by the production of syngas via the reverse water-gas shift (RWGS) reaction; or b) the production of green syngas through high-temperature co-electrolysis of steam and carbon dioxide, subsequently establishing pathways for conversion into fuels and chemicals, such as Fischer-Tropsch synthesis or methanol synthesis, and further methanol-to-olefin, gasoline, or jet fuel processes [27]. In these cases, multi-stage methods are employed, involving processes like heat transfer and energy-intensive gas compression processes [28]. Therefore, low-temperature electrochemical activation of CO_2 offers a promising alternative, addressing both traditional pathways and introducing a third option, c) directly converting CO_2 electrochemically into organic products or other valuable compounds. This strategy aims to reduce energy and heat losses and simplify reaction pathways, thereby enhancing efficiency and lowering costs [29].

1.2 CO_2 electroreduction

1.2.1 Fundamentals of CO_2 electroreduction

The electrochemical conversion of CO_2 has been widely recognized for its great potential, mainly because it would provide a more elegant and direct way to carbon-based

fuels and chemicals compared to pathways involving green hydrogen or syngas as intermediates. CO_2RR make it possible to produce the commodities and fuels currently predominantly derived from carbon-intensive fossil fuel methods as Figure 1.5 shows [30, 31]. In an ideal scenario, a pivotal step in the electrochemical reduction of the carbon dioxide process can directly yield fuels or chemicals like carbon monoxide [32], formic acid [33], methane [34, 35], ethylene [36, 37], and methanol [38], with the additional potential for synthesizing longer carbon-chain hydrocarbons [39, 40].

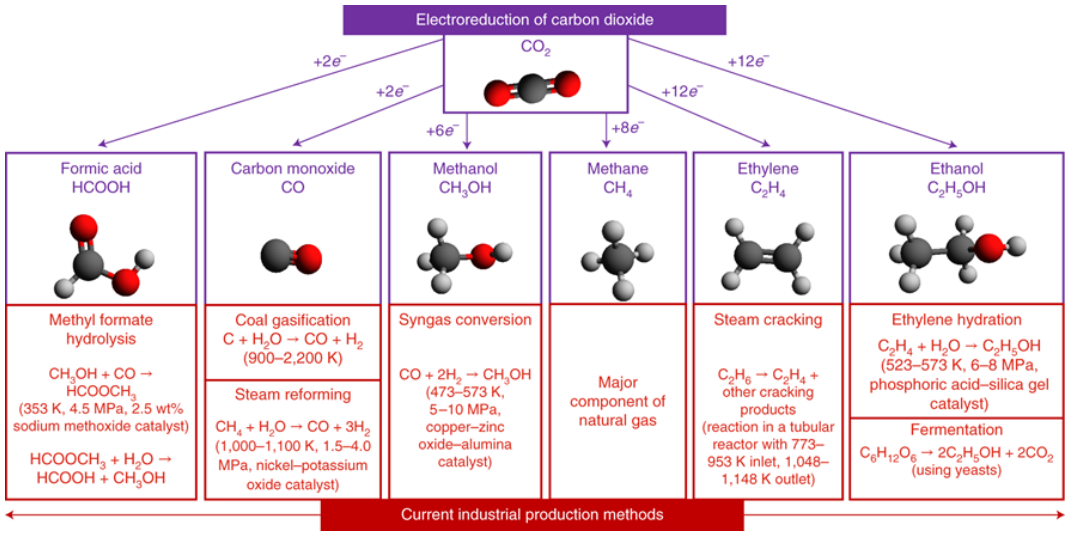

Figure 1.5: Overview of key CO_2 electroreduction products and the corresponding industrial production methods [31].

Notable features of CO_2RR technology include: (1) operation at ambient temperature and pressure, affording significant flexibility in practical applications; (2) the ability to convert and store fluctuating renewable energy such as solar, tidal and wind power in chemical products to extend power reserves [41]. The implementation of the CO_2 electroreduction process is poised to contribute to a reduction in global demand for fossil fuels, thereby propelling the transition towards more sustainable energy and chemical production paradigms. Due to its intriguing prospects, the electrochemical reduction of CO_2 has garnered considerable attention in the scientific community and stands as a significant subject requiring further investigation.

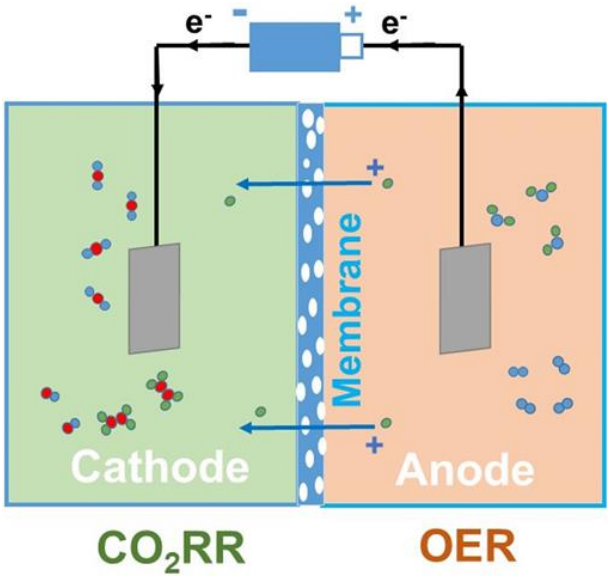

Figure 1.6: Schematic illustration of a typical reaction unit of electrochemical reduction of CO_2 [42].

A typical electrolyzer for CO_2 reduction structurally comprises a cathode, anode, electrolyte, and separator as Figure 1.6 shows [42, 43]. To drive the reaction, electrical energy input is required. Based on the types of shuttle ions, there are roughly two reaction models. In the cation exchange system [44], the anode undergoes the oxygen evolution reaction (OER), splitting water into gaseous oxygen, electrons, and protons. Electrons travel along the external circuit to the cathode, while protons traverse the membrane and electrolyte to reach the cathode. The anode reaction is as follows:

$$2H_2O \rightarrow O_2 + 4H^+ + 4e^- \quad (1.1)$$

In an anion exchange membrane system, electrons reach the cathode while the main energy carrier ion OH^- shuttles from the cathode to the anode [45]. OER occurs on the anode side, producing gaseous O_2, electrons, and H_2O.

$$4OH^- \rightarrow O_2 + 2H_2O + 4e^- \quad (1.2)$$

Either way, CO_2 molecules combine electron transfer and/or proton migration at the cathodic electrocatalyst surface to cleave C-O bonds and form related intermediates [46]. The main half reactions at the cathode are listed in Table 1 in Section 1.2.2. Finally, these intermediates rearrange to form products and desorb from the catalyst surface to

form different products [42, 47]. The use of a separator membrane can be to prevent product crossover [48].

1.2.2 Thermodynamics and kinetic theory

Table 1.1: Half electrochemical thermodynamic reactions of selected CO_2RR products, together with their corresponding standard redox potentials (V vs. RHE) [49, 50].

	Acid		**Base**	
Products	**Equation**	***E*(V)**	**Equation**	***E*(V)**
Hydrogen	$2H^+ + 2e^- \rightarrow H_2$	0.000	$2H_2O + 2e^- \rightarrow H_2 + 2OH^-$	−0.828
Carbon monoxide	$CO_2 + 2H^+ + 2e^- \rightarrow CO + H_2O$	−0.104	$CO_2 + H_2O + 2e^- \rightarrow CO + 2OH^-$	−0.932
Methane	$CO_2 + 8H^+ + 8e^- \rightarrow CH_4 + 2H_2O$	0.169	$CO_2 + 6H_2O + 8e^- \rightarrow CH_4 + 8OH^-$	−0.659
Methanol	$CO_2 + 6H^+ + 6e^- \rightarrow CH_3OH + H_2O$	0.016	$CO_2 + 5H_2O + 6e^- \rightarrow CH_3OH + 6OH^-$	−0.812
Formic acid	$CO_2 + 2H^+ + 2e^- \rightarrow HCOOH$	−0.171	$CO_2 + H_2O + 2e^- \rightarrow HCOO^- + OH^-$	−0.639
Ethylene	$2CO_2 + 12H^+ + 12e^- \rightarrow C_2H_4 + 4H_2O$	0.085	$2CO_2 + 8H_2O + 12e^- \rightarrow C_2H_4 + 12OH^-$	−0.743
Ethane	$2CO_2 + 14H^+ + 14e^- \rightarrow C_2H_6 + 4H_2O$	0.144	$2CO_2 + 10H_2O + 14e^- \rightarrow C_2H_6 + 14OH^-$	−0.685
Ethanol	$2CO_2 + 12H^+ + 12e^- \rightarrow CH_3CH_2OH + 3H_2O$	0.084	$2CO_2 + 9H_2O + 12e^- \rightarrow CH_3CH_2OH + 12OH^-$	−0.744
Acetic acid/acetate	$2CO_2 + 8H^+ + 8e^- \rightarrow CH_3COOH + 2H_2O$	0.098	$2CO_2 + 5H_2O + 8e^- \rightarrow CH_3COO^- + 7OH^-$	−0.653
***n*-Propanol**	$3CO_2 + 18H^+ + 18e^- \rightarrow CH_3CH_2CH_2OH + 5H_2O$	0.095	$3CO_2 + 13H_2O + 18e^- \rightarrow CH_3CH_2CH_2OH + 18OH^-$	−0.733

Electrochemical CO_2RR encounters two intrinsic challenges during its development: the relatively high thermodynamic stability of CO_2 molecules and the high overpotential due to the sluggish reduction kinetics [51]. The CO_2 molecule is a stable linear molecule with a strong C=O bond (750 kJ mol^{-1}) [52-54], and its reduction requires overcoming a high energy barrier, resulting in a significant overpotential. Despite

appearing more positive in potential compared to hydrogen evolution, the reduction process of carbon dioxide molecules is almost always accompanied by the first step of the activation of the CO_2 molecule, with the corresponding electrode potential for this reaction being -1.90 V (vs. SHE) [54, 55]. In this process, the first electron transfer to form CO_2* intermediate has a very negative redox potential, leading to high energy consumption and unfavorable electrochemical reduction reactions [56]. Table 1.1 summarizes the half electrochemical thermodynamic reactions of selected CO_2RR products, including CO, methane (CH_4), methanol (CH_3OH), formic acid (HCOOH), ethylene (C_2H_4), and ethanol (CH_3CH_2OH), and the corresponding standard redox potentials [49].

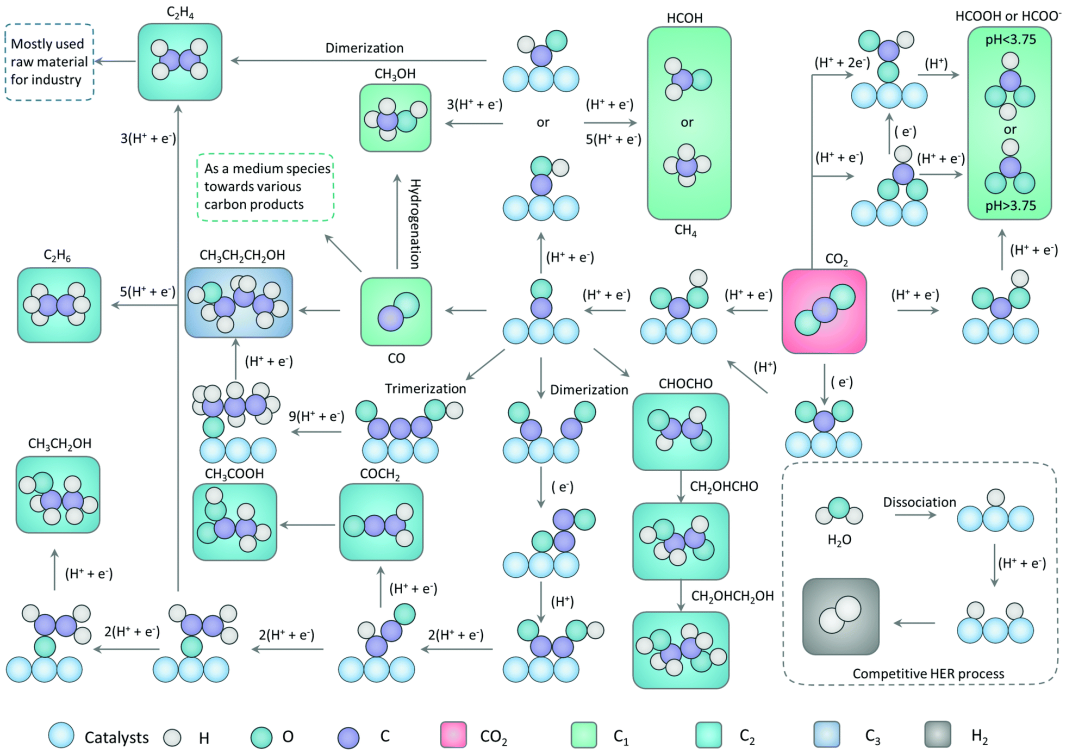

Figure 1.7: Overview of reaction pathways for CO_2RR towards different products [56, 57].

Furthermore, the carbon dioxide reduction reaction involves multiple reaction pathways, which offers the potential to generate diverse and valuable products while limiting the selectivity of specific products, as shown in Figure 1.7 [56]. CO_2RR electrocatalysis is a complex, multi-step process involving various proton-coupled

electron transfer (PCET) events that require the sharing of crucial intermediates among these reaction pathways [50]. An indispensable intermediate in this context is *CO, playing a pivotal role in carbon monoxide production and equally crucial in the synthesis of numerous hydrocarbons and oxygenates, including methane, ethylene, methanol, and ethanol. The pathways to methane and methanol rely on different *CHO intermediates after the previous *CO intermediate [57]. Additionally, CO_2RR requires the involvement of protons or proton donors (such as HCO_3^-) to disrupt the C=O bonds, leading to inevitable side reactions competing with the hydrogen evolution reaction (HER) [58]. Achieving efficient specific-product generation, particularly when targeting C_{2+} chemicals, poses a highly challenging task due to internal competition. This needs a profound understanding of reaction pathways and the design of efficient catalysts and reaction conditions to maximize the selectivity toward the desired products.

1.3 Components of CO_2RR systems

1.3.1 Catalysts

Catalysts are essential in chemical reactions because they can effectively reduce the activation energy of a reaction and speed up the reaction. As a matter of fact, many large-scale applications use precious metal catalysts. Furthermore, to ensure favorable economic benefits, in particular for large-scale applications, catalysts should be made from cheap, readily available ingredients [59, 60].

Cathode catalysts

The selection of cathodic catalyst materials significantly determines the distribution of products and conversion efficiency. In the previous work by Hori et al., a comprehensive summary of various transition metal cathodic catalysts has been provided, revealing their activity in the electrocatalytic CO_2 reduction reaction and the properties of the resultant products, as Figure 1.8a shows [61]. Electrocatalysts should possess active sites with high turnover frequencies and appropriate binding energies [62], facilitating the rapid generation of desired products while achieving the reaction at low overpotentials. Figure 1.8b reveals the binding energy characteristics between the intermediate species

CO* and H* for various metal catalysts [63]. Among them, copper (Cu) material is considered to be a unique and promising catalyst due to its property of showing moderate binding energy for both intermediates at the same time [64].

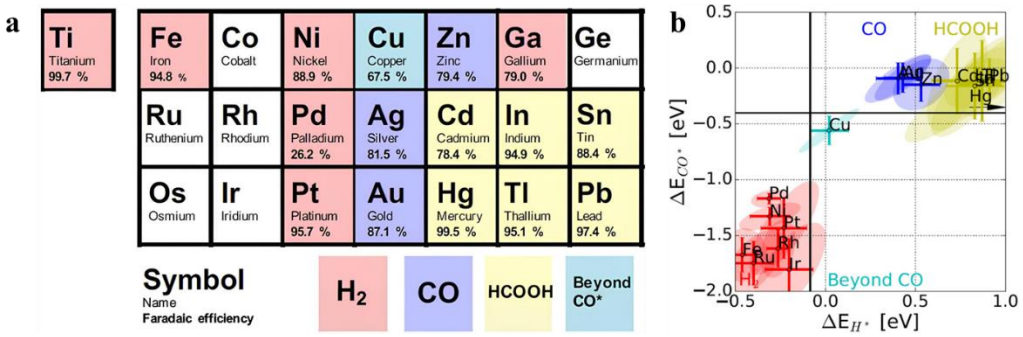

Figure 1.8: (a) Classification of metal catalysts affecting the main products of CO_2 electroreduction. (b) The binding energy of the catalyst for the intermediates CO* and H* [63].

The performance of various catalysts has been significantly improved by optimizing active sites or adjusting structure and morphology [51, 65, 66]. For example, extensive attention has been paid to crystalline facets [67], morphological features [68], support effect [69], alloy effects [70], and surface modification [71]. Some non-copper materials have emerged to generate C_{2+} products, introducing novel possibilities to this field [72-74]. In addition, bimetallic catalysts are believed to be able to regulate surface adsorption energy and reaction pathways through electronic coupling and synergistic effects between metals [75]. Moreover, the bifunctional catalyst system can be applied to both electrocatalysis and low-temperature thermal catalysis by designing multiphase interfaces and active center coordination environments, providing new possibilities for realizing the integrated production of long chain hydrocarbons through a more complex reaction sequence which involves electro- and thermo-catalysis [76].

Anode catalysts

The utilization of anodic electrocatalysts effectively mitigates the overpotential required for the oxygen evolution reaction. IrO_2 and RuO_2-based catalysts are widely acknowledged for their superior activity and stability in this regard [77, 78]. Some

investigations have commenced exploring cost-effective alternatives to precious metal catalysts, including transition metals such as nickel, cobalt, and iron [79]. In the electrolysis of carbon dioxide reduction reactions under alkaline conditions, commercial nickel foam can be employed as an anodic OER catalyst [80, 81]. However, it is crucial to note that the proton generation during the reaction process induces local pH variations, potentially further impacting the OER kinetic activity of low-cost transition metal catalysts. Therefore, more in-depth research is imperative to comprehensively understand and optimize these processes for enhancing the performance of economic catalysts [82].

1.3.2 Ion exchange membranes

Ion exchange membranes (IEMs) play a crucial role in studying CO_2RR analysis [83], as they effectively isolate the cathode and anode, preventing crossover between electrolyte and products while maintaining ionic charge balance within the membrane electrode assembly (MEA) electrolyzer. Currently, three main types of membranes are commonly employed in electrochemical reactions, namely, anion exchange membranes, cation exchange membranes, and bipolar membranes [84, 85]. These membranes facilitate the transmission of anions (e.g., OH^-), cations (e.g., H^+), as well as scenarios involving simultaneous transport of both cations, shown in Figure 1.9.

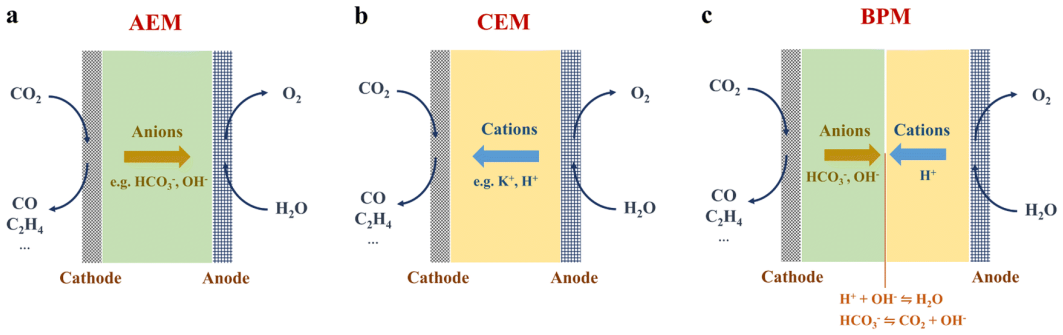

Figure 1.9: Schematic representation of different types of ion exchange membranes [86].

The cation exchange membrane is favored due to its outstanding proton transfer performance. Opting for acidic or neutral anode electrolytes assists in controlling proton concentration but imposes constraints on the selection of OER anode catalysts, typically involving expensive noble metals such as Ru and Ir [55]. Conversely, an additional

consideration is the potential promotion of the HER at the cathode due to an excess of protons [87]. Furthermore, a stringent requirement for enhanced stability is posed on the materials utilized for anode and cathode electrocatalysts, particularly in a strongly acidic environment [88]. Huang and colleagues demonstrated the electroreduction of CO_2 in a highly acidic electrolyte ($pH \leq 1$) by leveraging both the confinement effect and cation effect to collaboratively adjust the local microenvironment. As a result, they achieved an Faradaic efficiency of 83.7% and a single-pass carbon efficiency of 54.4% and maintained stable electrolysis for 30 hours in a flow cell for hydrocarbon production [89].

The application of anion exchange membranes with alkaline electrolytes has gained widespread prominence in CO_2 reduction reaction electrolysis cells [90]. In this system configuration, anions such as OH^- in the cathode compartment are transported to the anode compartment, impeding the transfer of protons and hindering the hydrogen evolution reaction. Alkaline electrolytes usually exhibit lower overpotentials and higher conductivity compared to neutral conditions. The Sargent group demonstrated that utilizing 1 M KOH electrolyte in the AEM electrolysis cell can achieve current densities exceeding 1 A/cm^2 and Faradaic efficiency exceeding 65% for C_{2+} products [91]. Furthermore, they conducted sustained performance tests for CO_2 reduction to ethylene over 150 hours using a 7 M KOH electrolyte [92]. However, in alkaline CO_2 reactors, particularly at high current densities, OH^- may rapidly react with CO_2 to form HCO_3^- and CO_3^{2-}, which cross over to the anode, thus causing CO_2 loss [93, 94]. This also leads to the precipitation of carbonates on the cathode, covering the effective sites for CO_2 reduction reactions [95]. Despite these challenges, AEM remains one of the most promising candidates for CO_2RR due to its highly stable current efficiency and energy efficiency.

The Bipolar membranes (BPM) are composed of a cation exchange membrane, an anion exchange membrane, and an interface connecting layer [96]. BPM enables cathode and anode to operate in different electrolytes or pH environments and effectively prevents product from crossing through the membrane. During the reaction process, water molecules in the membrane dissociate into OH^- and H^+, migrating to the anode and cathode, respectively. However, the migration of OH^- and H^+ also induces changes in the

pH around the electrodes, affecting the selectivity of CO_2 reduction. Consequently, it is typically necessary to introduce a buffer layer electrolyte separating the gas diffusion electrode from the BPM to suppress the hydrogen evolution reaction and maintain the stability of the reaction microenvironment. Moreover, the delamination of membranes results in poor stability, even at low current densities [97]. Furthermore, compared to well-known AEM-MEA and CEM-MEA zero-gap configurations, the inclusion of additional membranes in a BPM-MEA unavoidably increases the ohmic resistance of the cell and with it the energy losses.

1.3.3 Electrolyzers with ion exchange membranes

Well-designed electrolyzers and efficient electrocatalysts are both crucial to the performance of CO_2RR systems. The geometric design of the electrolyzer has an important influence on the current density and gas-liquid distribution [98]. There are three main shapes of electrolyzers with ion exchange membranes: H-type electrolyzer, flow electrolyzer, and zero-gap electrolyzer, as shown in Figure 1.10. H-type and flow reactors have been widely used in laboratories, and the MEA electrolyzer is gradually expanding its influence [99]. The development of electrolyzers has been slow compared to the large amount of attention paid to materials/catalysts and reaction mechanisms. Engineering innovation of electrolyzers is an inevitable road to CO_2RR technology development [100].

H-cell

The commercially available H-type cell has been the preferred choice in laboratory research, as it facilitates the assessment of catalyst performance in solution systems [101]. In such cells, the anode and cathode are completely immersed in a liquid electrolyte in the cathode and anode compartments, respectively, separated by an ion exchange membrane. However, due to the relatively low solubility of CO_2 in aqueous solution (about 35 mM at 25 °C, 1 atm) [53, 102], the dissolved CO_2 exhibits low concentration and long diffusion distance when migrating in the electrolyte, which limits the reactivity and generally lead to low current density [103].

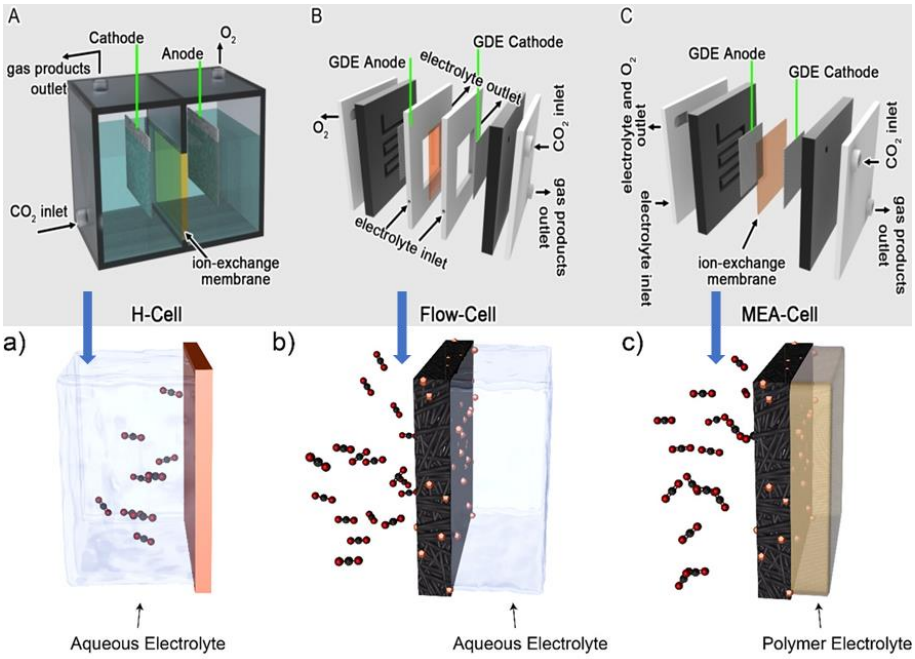

Figure 1.10: Three main electrolyzer structures: H-cell, flow electrolyzer, and MEA electrolyzer [100]. And the corresponding CO_2 gas and electrolyte transport pathways [104].

Flow electrolyzer

Flow electrolyzers enable continuous flow of reactants and products and enhanced mass transport. CO_2 gas penetrates the highly porous gas diffusion electrode (GDE) directly to the cathode, allowing for higher CO_2 concentrations on the catalyst surface [105]. The cathode electrocatalyst is firmly anchored on a gas diffusion layer (GDL), which is in contact with the flowing cathode electrolyte on one side and directly supplied with CO_2 gas on the other side. The unique design of the GDE structure effectively isolates the electrolyte and gaseous reactants, ensuring that CO_2 participates in the reduction reaction in gaseous form [83]. It is worth noting that due to the direct contact between the catalyst layer and the electrolyte, GDEs with insufficient hydrophobicity seem to be unable to block the electrolyte penetration, resulting in cathode flooding and thus aggravating the HER [106]. In addition, high ohmic impedance, carbonate formation, and crossover oftentimes observed in flow cells are also quite troublesome. Despite this advancement, further attention is needed to improve the energy conversion efficiency and long-term performance of such liquid-phase flow electrolyzers.

MEA electrolyzer

In the MEA electrolyzer configuration, the cathode gas diffusion layer with the catalyst layer is placed directly adjacent to the exchange membrane, and humidified CO_2 is directly supplied to the catalyst layer from the back of the GDL [107]. Theoretically, by reducing the distance between the two electrodes in an MEA electrolyzer, the resistance between the cathode and anode in the electrolyzer will be minimized as undesired electrolyte ohmic losses are eliminated. If properly designed, the zero-gap electrolyzer can operate at lower cell voltages, thereby yielding higher electrolysis efficiency. Additionally, it is more feasible to pressurize or scale up systems based on this more compact design.

Overall, the design optimization of the electrolyzer can effectively improve the overall performance of CO_2RR and affect the final product selectivity, efficiency, and system stability. In the future, the development of electrolyzers will move towards more efficient, more compact, and more suitable ones for large-scale industrial applications.

1.4 Status and development

Until now, significant and rapid progress has been achieved in CO_2 electrolysis for the production of valuable fuels and chemical raw materials. The evolution of this technology can be attributed to relentless efforts in various domains such as the revelation of reaction mechanisms, the design of electrocatalysts, modification of electrodes, and optimization of electrolytic cells over the past few decades. These endeavors have demonstrated the feasibility of storing energy intermittent from renewable energy sources as carbon fuels. Furthermore, the configuration of the electrolytic cell plays a crucial role in CO_2 electrolysis systems, directly impacting the efficiency and stability of the CO_2 electrolysis process. With ongoing developments and improvements in ion exchange membranes, there is a prospect of enhancing the efficiency and product selectivity of the CO_2 electrolysis process. Innovations in this regard not only contribute to the reliability and sustainability of CO_2 electrolysis technology but also propel the commercialization efforts of this technology.

- Electroreduction of CO_2 to CO with Au and Ag catalysts, and to formate with Sn and Bi catalysts, have demonstrated commercial possibilities with catalysts. Dioxide Materials Inc. has commenced operational activities for a commercial-scale electrolytic cell designed for the conversion of carbon dioxide into formic acid. Det Norske Veritas (DNV), Norway, demonstrated a semi-pilot-size reactor for electrochemical reduction of CO_2 to formate/formic acid with Sn as catalysts [108, 109].
- Dioxide Materials Inc. has introduced Sustainion™, an alkaline-stable imidazole-based anion exchange membrane, and related polymers, achieving commercial success and widespread application [110]. Other commonly used AEMs include the Fumasep® FAA series (Fumatech) and Aemion™ (Ionomr Innovations), both offer good chemical resistance and operational stability. Additionally, CEMs such as Nafion® (Chemours) and Aquivion® (Solvay) have also exhibited outstanding performance and durability in catalytic applications for CO_2RR [111].

In contrast to direct CO_2RR, which converts CO_2 into fuels or chemicals in a single-step, low-temperature electrochemical process, the electrofuel (e-fuel) route represents an indirect but industrially mature pathway for carbon-neutral fuel production. E-fuel production, by comparison, leverages well-established downstream synthesis routes and benefits from high energy density, compatibility with existing fuel infrastructure, and easier storage and transport of liquid products.The e-fuel process typically begins with the capture of CO_2 from air (via direct air capture, DAC) or point sources such as industrial flue gases. Concurrently, renewable electricity is used to produce H_2 via water electrolysis. This can be performed through low-temperature technologies such as alkaline water electrolysis (AWE) and proton exchange membrane (PEM) electrolysis, or via high-temperature solid oxide electrolysis cells (SOEC), which offer improved efficiency and can utilize industrial-grade heat sources. The generated H_2 is then reacted with CO_2 to produce syngas, either via the RWGS reaction or directly through high-temperature co-electrolysis of CO_2 and H_2O. This syngas serves as a precursor for fuel synthesis through catalytic processes such as Fischer–Tropsch synthesis or methanol synthesis, yielding a variety of liquid products including synthetic gasoline, diesel, jet

fuel, methanol, or dimethyl ether. These products are subsequently refined and can be directly used in existing combustion engines and infrastructure.

- Twelve (USA, https://www.twelve.co/) develops modular electrolyzer systems that use renewable electricity to convert CO_2 and green hydrogen (sourced from water) into hydrocarbon fuels and chemicals via an electrochemical process called Power-to-X, or Power-to-Liquid for fuels. Carbon Recycling International (Iceland, https://carbonrecycling.com/) is a pioneer in Power-to-Methanol technology, turning CO_2 and renewable hydrogen into methanol. The company is integrating electrochemical CO_2 conversion into its systems and has demonstrated large-scale feasibility through its Emissions-to-Liquids® plants. Air Company (USA, https://www.aircompany.com/) produces ethanol used in consumer products like perfumes and sanitizers, combining CO_2RR with renewable hydrogen. Siemens Energy (Germany, https://www.siemens-energy.com/) has collaborated with several companies to develop integrated electrolyzer-CO_2RR systems, focusing on large-scale production, process integration and renewable energy compatibility, and is a model for the transformation of the traditional energy industry to carbon recycling. For example, Siemens Energy and Evonik launched the Rheticus project in 2018 to produce carbon monoxide through low-temperature electrolysis and combine it with gas fermentation to produce hexanol.
- The high-temperature co-electrolysis cell, which effectively converts carbon dioxide and water into syngas, has been established at system level. For instance, at KIT's Energy Lab (https://www.elab.kit.edu/) within the Copernicus P2X project, a 220 kW high-temperature SOEC cell developed by Sunfire (Germany, https://sunfire.de/) is employed for hydrogen or synthesis gas production, subsequently utilized in the production of aviation fuels.

The optimistic developments regarding industrial applications of CO_2RR are predominantly centered around C_1 compounds or syngas products. The selectivity towards multi-carbon species remains a challenge in CO_2 reduction reactions, as the ultimate product selectivity is influenced by intricate and diverse reduction pathways,

accompanied by difficulties in regulating reaction routes and enhancing process intensification.

Overall, the progression from laboratory fundamental research to the scale-up of CO_2 electrolysis cells needs comprehensive discussion. It is imperative to address the ideal low-temperature CO_2 electroreduction reaction within the electrolysis cell, with a high current density (> 200 mA/cm^2), elevated Faradaic efficiency (e.g., FE_{CO} > 90%), and efficient energy utilization (cell voltage, E_{cell} < 3.0 V) to promote economic feasibility in replacing traditional energy sources with renewable alternatives [112]. While integrating all advantages into a single electrolysis cell architecture is challenging, low transfer resistance, excellent thermal stability, and good conductivity are crucial and indispensable when designing advanced CO_2RR electrolysis. Particularly, energy efficiency stands out as a primary challenge to be overcome during the transition to industrialization. Laboratory efforts must emphasize this parameter, considering potential greater energy losses upon scaling up. Therefore, it is crucial to rationally design and adjust the reaction chain and process conditions of the entire CO_2RR electrolysis system. In the construction of a coherent process chain, further research and optimization of heat management systems, operational conditions, water management, and flow field plates are paramount.

1.5 Research structure of this dissertation

The primary objective of this research is to enhance the efficiency of CO_2RR for synthesizing C_1-C_3 products, with a focus on overcoming multiple challenges in ensuring the stable operation of electrolyzers. The key is to strike a balance between maintaining a low voltage and high current, achieving high Faradaic efficiency, optimizing energy efficiency, and ensuring long-term operational stability. To attain this objective, a set of optimization strategies has been implemented.

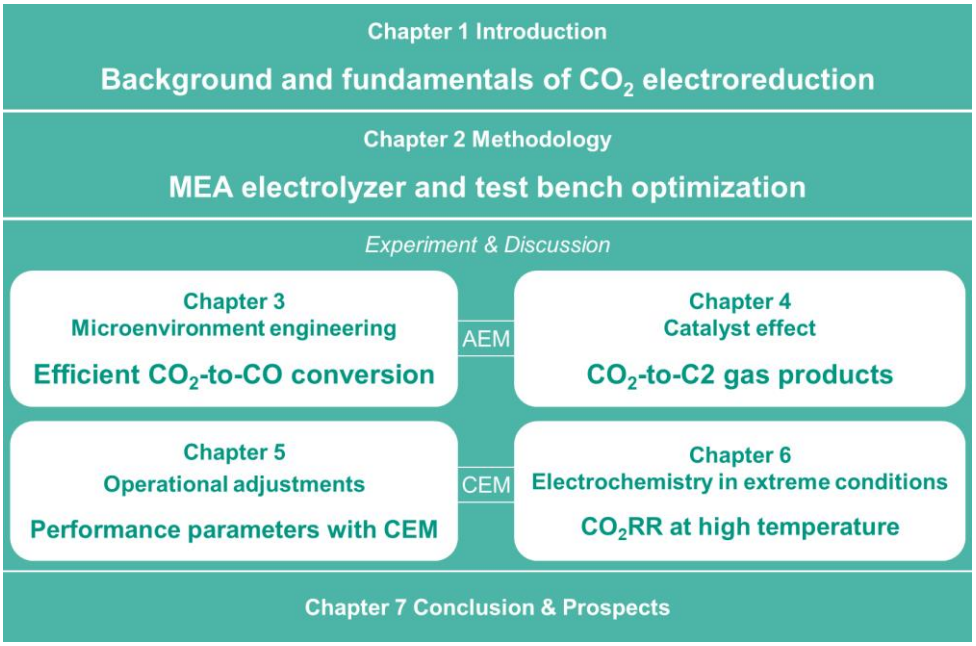

Figure 1.11: The structure and scope of this dissertation.

Initially, adjustments to the engineering characteristics and structure of the electrochemical reactor are made to minimize the distance between electrodes and reduce electrolyzer impedance. This serves to enhance energy efficiency and stability by minimizing internal resistance and improving reaction efficiency through electrolyzer design optimization. In addition, improvements in engineering properties ensure the electrolyzer operates stably over a longer period. Subsequently, industrial current density tests were conducted on conventional catalysts utilizing abundant materials. By manipulating external environmental conditions, such as electrolyte concentration, pH, catalyst loading, and cathode overpotential, a balanced internal microenvironment is maintained, facilitating prolonged efficient and stable operation. This strategy aims to uphold an ideal reaction environment under varying conditions, ensuring optimal catalytic effects and enhancing the selectivity and efficiency of CO_2RR synthesis products. Moreover, the impact of temperature and pressure on overall energy efficiency is investigated and validated. Systematic experiments and data analysis determine the most suitable temperature and pressure ranges, maximizing CO_2RR efficiency and promoting a more sustainable energy conversion process.

Divided into 7 chapters, this dissertation systematically and step by step introduces a series of electrochemical reduction operation strategy optimizations, which is expected to provide some inspiration and technical support for the development of electrochemical carbon dioxide reduction.

2 Methodology and Experiments

2.1 Overview

Despite the enormous potential of the electrochemical conversion of CO_2, major technological breakthroughs are still required to make the process economically viable. Mass transport limitations in H-cells limit the current density, thus requiring significant external drive voltage. In addition, challenges faced by electrolyte flow cells include high ohmic losses in the electrolyte, catalyst contamination by electrolyte impurities, and electrolyte overflow problems [101, 113]. Therefore, this study aimed to optimize CO_2 electrochemical conversion by adopting a zero-gap catholyte-free electrolyzer, to achieve high selectivity operation at low input voltage for long-term experiments.

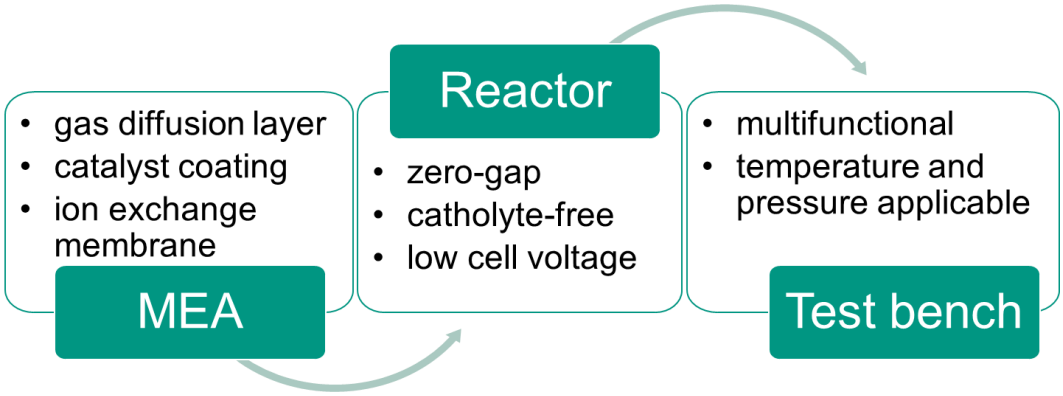

Figure 2.1: Engineering approach adopted to improve CO_2RR.

Figure 2.1 shows the optimization method and engineering layout for the CO_2RR in this doctoral work. Different commercial catalysts were sprayed onto the gas diffusion layer and formed into membrane electrode assemblies with several ion exchange membranes. By expanding the electrode surface area, increasing the reaction sites, using a setup without a cathode-side electrolyte, and combining with a zero-gap design, the mass transport is significantly enhanced, and the system resistance is reduced. Experiments showed that the current density of the zero-gap reactor was about two orders of magnitude higher than that of a conventional H-type electrolyzer. In addition, a versatile and compatible electrochemical testing platform was established, allowing rapid

switching of liquid, gas, or gas-liquid mixed reactants, suitable for a variety of electrocatalytic reactions such as CO_2RR, water electrolysis, nitrogen reduction, and even fuel cell operation. The combination of a back pressure regulator and an electronic pressure controller allowed the reactor to be operated at pressures up to 25 bar, limiting the anode-cathode pressure difference to within 0.1 bar. The thermostat and heat exchanger could adjust the experimental temperature up to 200 °C. These configurations enable the adaptation to variations in the internal reaction conditions environment, including pH, flooding, and carbonate precipitation, by adjusting external environmental parameters such as temperature, pressure, and flow rate. Subsequent sections will elaborate on the improvements made to the electrolysis cell and the utilization of the experimental apparatus designed for long-term operation.

2.2 Zero-gap electrolyzer assembly

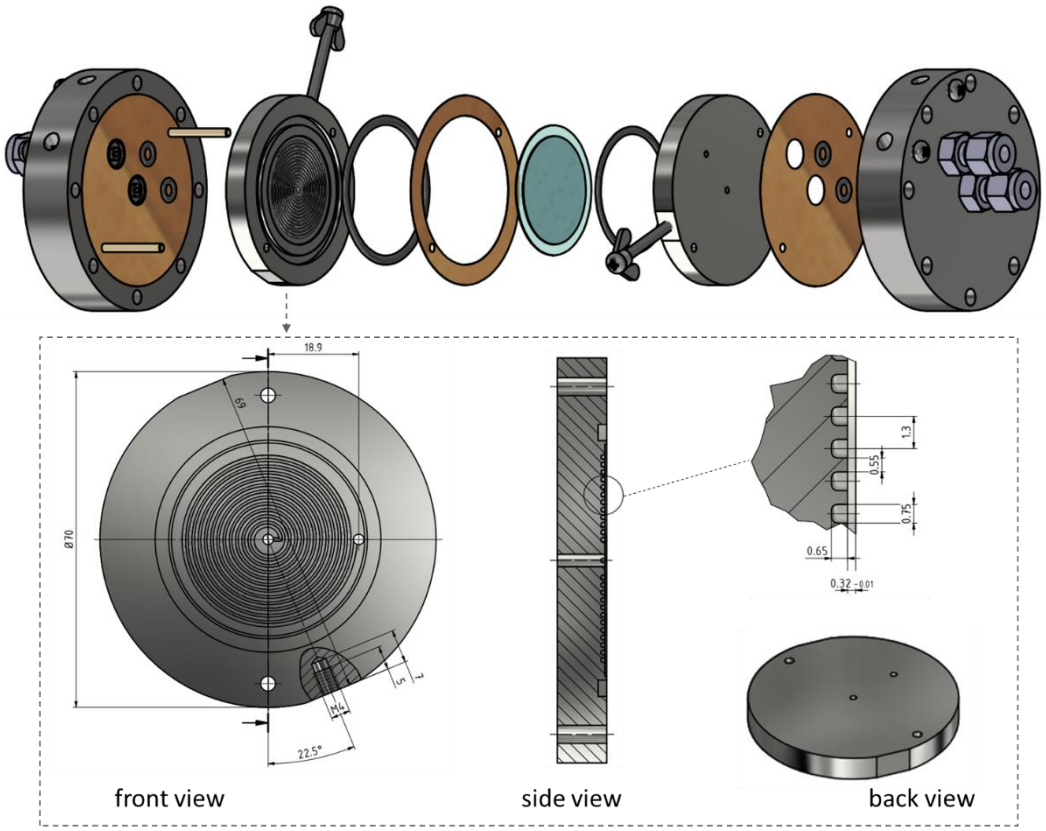

Figure 2.2: Diagram of the modified zero-gap electrolyzer [114].

The zero-gap membrane electrode assembly reactor is adapted from a commercial electrolyzer (Parr Instruments). For the modification, the original external housings, supporting nuts, and bolts are retained. As illustrated in Figure 2.2, the core MEA comprises a cathode and an anode directly pressed against opposite sides of the ion exchange membrane. Liquid and gas feeds are delivered through the housings to the anode and cathode respectively and can be heated by inserting heat cartridges from the side of the housings. Here, titanium flow field plates containing spiral channels with a width of 0.75 mm, a depth of 0.65 mm, and a pitch of 1.3 mm were fabricated by the milling process. Gaps of appropriate depth are reserved on the headspace over the flow channels to accommodate the membrane and gas diffusion layers so that the MEA can be properly compressed in the reactor. Titanium bolts inserted and tightened from the side of the flow field plate here function as current collectors. The entire assembly is sandwiched between two stainless steel shells and fastened by eight 6.35 mm diameter bolts, with Kapton foils placed as the insulator between each layer. Photos of the improved zero-gap electrolytic cell and its unfolded components are shown in Figure 2.3.

The MEA composition encompasses cathodes and anodes directly placed on either side of the ion exchange membrane, aiming to minimize ohmic losses between the electrodes. The aqueous electrolyte is delivered to the anode for the oxygen evolution reaction, while the cathodic side allows the absence of liquid electrolyte. The inlet for reactants forms at the center of the circular current collector, with outlet channels located peripherally. A continuous CO_2 stream diffuses along the microchannel flow field into the gas diffusion electrode and settles at the cathode, establishing a condensed distribution of CO_2 reactants within the catalytic layer, promising enhanced reaction rates. Additionally, stainless steel casing, O-rings, and insulating foils complete the sealing and insulation of the reactor, facilitating reasonable pressurization and uniform heating for electrocatalytic reactions.

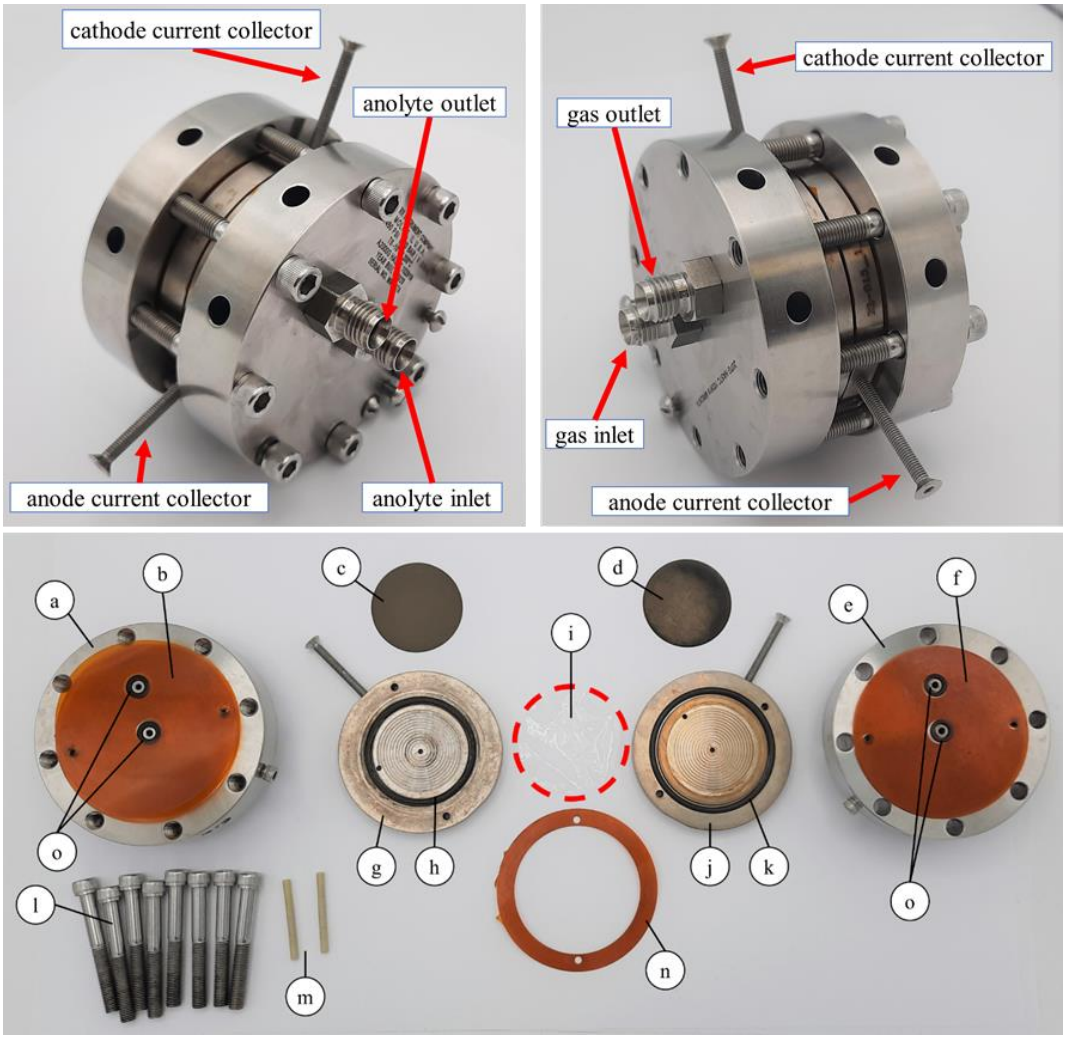

Figure 2.3: Photos of the modified zero-gap electrolyzer. Exploded parts photo includes: (a) cathode side housing, (b, f, n) insulation, (c) cathode, (d) anode, (e) anode side housing, (g) cathode electrolyte plate, (h, k, o) O-rings, (i) membrane, (j) anode electrolyte plate, (l) screws, and (m) locating pins.

2.3 Test bench construction

The MEA system based on ion exchange membranes with micrometer-scale thickness and fragile gas diffusion electrodes needs the maintenance of a stable interface to ensure sustainable operation, particularly when reactants show in different phases. For example, the cathode reactants are in the gas phase, the anode reactants are in the liquid phase, and gaseous products are produced on both sides. Therefore, it is crucial to precisely control the inlet flow rates of various gases and liquids in the electrolyte channel

and the dynamic equilibrium pressure within the reactor. The integrated process and instrumentation diagram (P&ID) is shown in Figure 2.4.

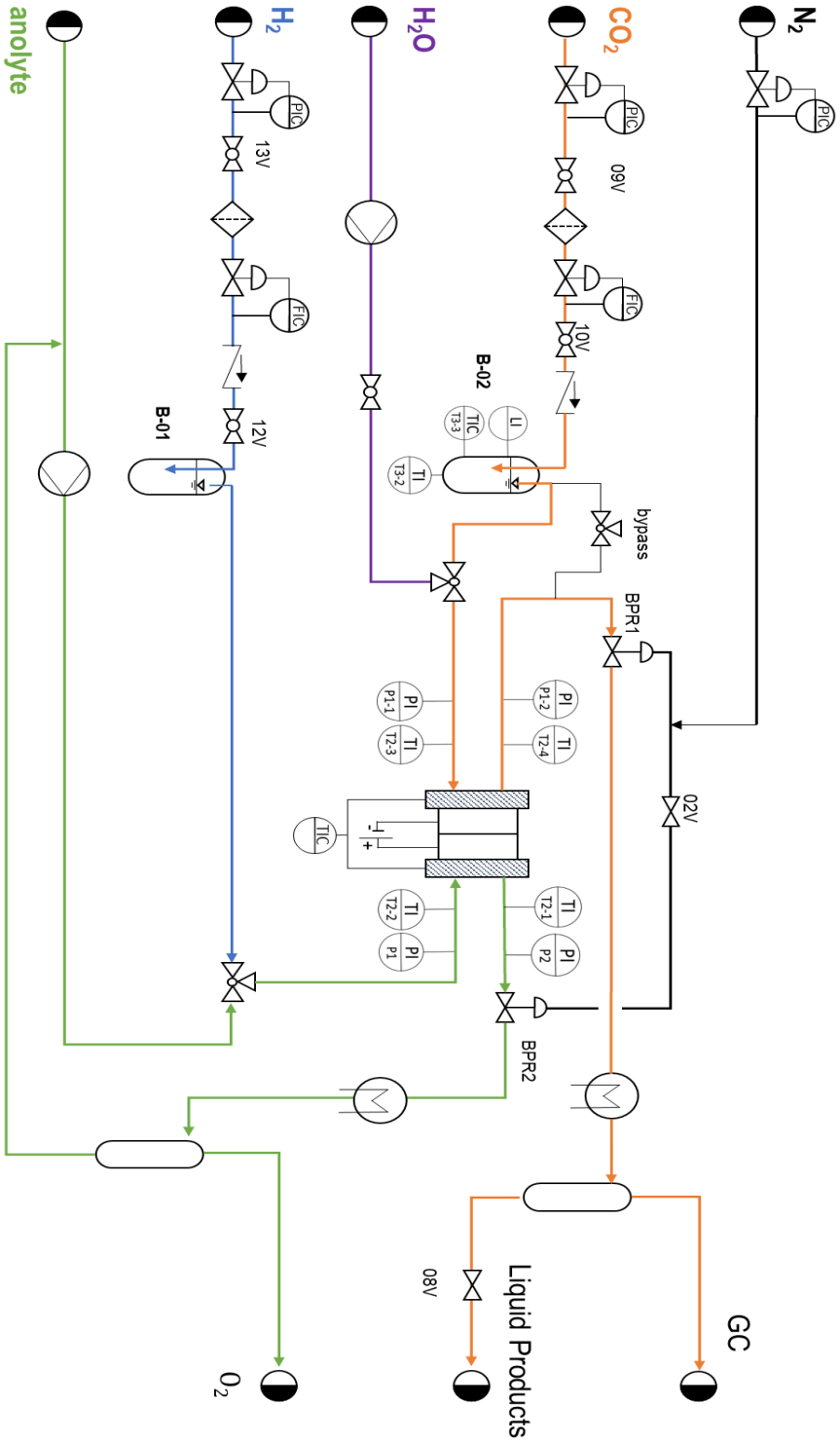

Figure 2.4: Multifunctional test bench integrated design and construction.

In this designed experimental setup, a combination of back pressure regulators and an electronic pressure controller was employed to balance the pressure on both sides of the membrane within the electrolysis cell, with nitrogen utilized as a balancing buffer gas for the electronic pressure controller, which does not pass through the reactor. At the outlets of the cathode and anode, two back pressure valves were installed respectively. The pressure was maintained at the same value by the same pressure controller to ensure consistent pressure on both sides of the ion exchange membrane. Typically, in pressurized experiments, the electronic pressure controller is software-controlled to ramp up to the target pressure at a rate of 0.2 bar/min, with a maximum value of 25 bar. Four electronic pressure sensors were installed at the inlet and outlet of the cathode and anode of the electrolysis cell, enabling real-time pressure change detection and control.

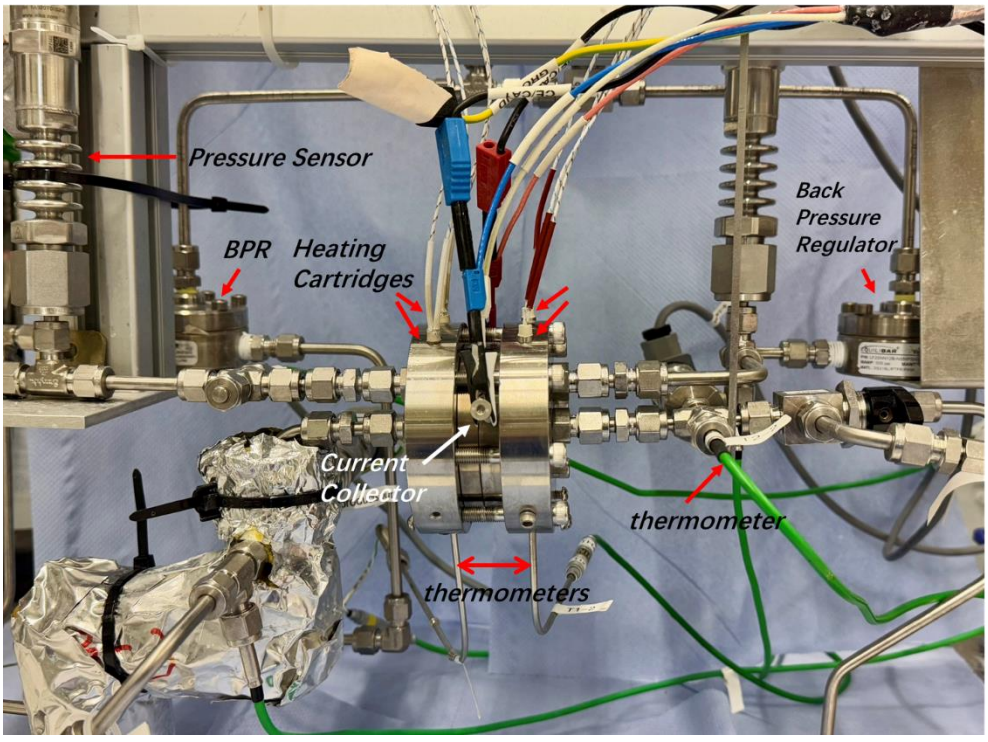

Figure 2.5: Photo of the reactor and key components.

The temperature distribution of the entire system was controlled by calibrated thermocouples and temperature controllers. Four heating cartridges inserted into the casing of the electrolysis cell were mainly used to heat the cell, with a maximum temperature of up to 200 °C. Four electronic temperature sensors were installed at the

inlet and outlet of the cathode and anode of the electrolysis cell, enabling real-time temperature change detection. Additionally, the pipelines and the moistening cylinder were heated by heating cables wrapped around their surfaces. The two tube-in-tube heat exchangers downstream of the outlet are specifically employed for high-temperature reactions exceeding 80 °C. A photograph of the reactor and key components is shown in Figure 2.5.

On the anode side, a three-way valve was used to provide two options for reactant entry: (1) using an HPLC pump to continuously pump the anode electrolyte stored in a reservoir through the electrolysis cell and flow back for recirculation (green line), or (2) using gas reactant; for example, hydrogen for fuel cell (blue line). The product from the anode passed through a back pressure valve to return to atmospheric pressure, and the electrolyte was collected for recycling, while the product oxygen could be directly released into a fume hood. Similarly, on the cathode side, a three-way valve was used to provide two options for reactant entry. Carbon dioxide gas passed through a gas flow meter and was then introduced into the electrolysis cell after being moistened in a self-assembled liquid cylinder with a volume of 1 liter. The resulting cathode product passed through a back pressure valve to return to atmospheric pressure and was then separated. The cathode gas product enters the GC directly, while the liquid product is collected (yellow line). Another option was for the liquid to be introduced directly into the electrolysis cell via another HPLC pump, serving as a possible cathode electrolyte or rinse solution (purple line).

The long-term stability of electrolysis systems is crucial for practical applications and commercialization. Maintenance and replacement of components may incur high costs and endanger the economic viability of the technology. Long-term stability also contributes to enhancing the overall reliability of the system and its ability to operate continuously in industrial environments. Therefore, the adoption of a compatible multi-channel, multi-functional test bench facilitates better realization of long-term stability experiments. A photo of the constructed CO_2RR test bench is shown in Figure 2.6.

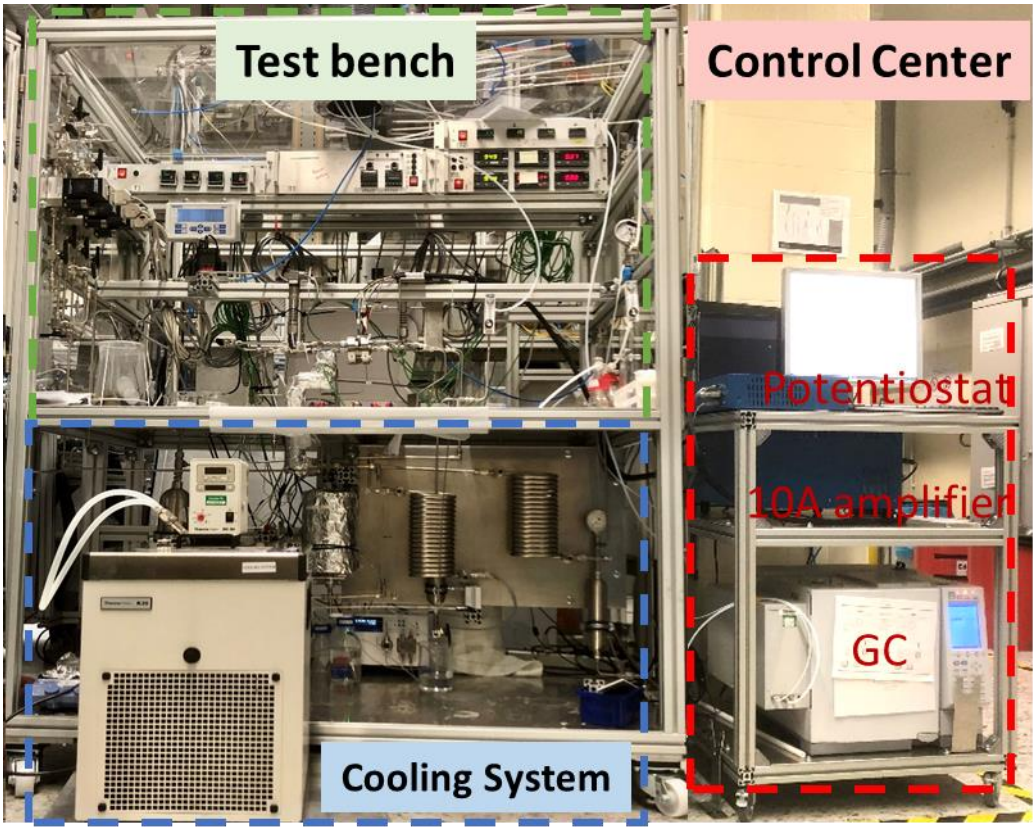

Figure 2.6: Photo of the CO_2RR test bench in the laboratory.

2.4 Experimental preparation

2.4.1 Chemical and gas specifications

The following chemicals were procured from Thermo Fisher Scientific™: potassium bicarbonate (analytical grade, purity 99.5%), potassium hydroxide (analytical reagent grade), silver nanopowder (Ag, average particle size 20-40 nm, purity 99.9%), copper nanopowder (Cu, average particle size 20-50 nm, purity 99.9%); from Sigma-Aldrich: Nafion 117 perfluorinated solution, sulfuric acid (0.5 mol/L). All chemicals were of analytical grade and required no further purification before use. Nafion®212 membranes were sourced from Ion Power GmbH; Sustainion® 37-50 membrane from Dioxide Materials; Celtec® membrane from BASF. Carbon paper (thickness: 325 ± 25 µm, Sigracet 39BB) and platinized titanium fiber felt (porosity: 53–56%, thickness: 200–300 µm) were procured from the Fuel Cell Store (https://www.fuelcellstore.com/);

deionized water was obtained from a Millipore Autopure system. CO_2 (99.999%), N_2 (99.999%), Ar (99.999%), and H_2 (99.999%) were all supplied by Air Liquide company.

2.4.2 Electrode preparation

Figure 2.7 outlines a common electrode preparation process to provide a general guide for using air spraying in MEA manufacturing. First, the gas diffusion layer is cut according to the size of the electrolyzer. Subsequently, the catalyst and the appropriate solvent ratio are mixed by ultrasound to form a uniform catalyst ink, and the selected solvent can be isopropyl alcohol or other compatible solvents. The air spray gun settings are adjusted, and the appropriate amount of catalyst ink is loaded into the gun container. The desired spray range and atomization effect are achieved by adjusting the carrier gas pressure (1-3 bar). The air spray gun nozzle is then suspended and aimed at the GDL placed on the heat source at a distance of about 10 cm, and then the catalyst ink is sprayed on the GDL surface multiple times until the solvent is dry, following the recommended drying temperature for different catalysts and adhesives. It is recommended to set up a fence around the perimeter of the GDL to establish a boundary to limit the spray area to help spray control and prevent excessive splashing. If necessary, the spraying process can be repeated to achieve the desired catalyst loading on the substrate.

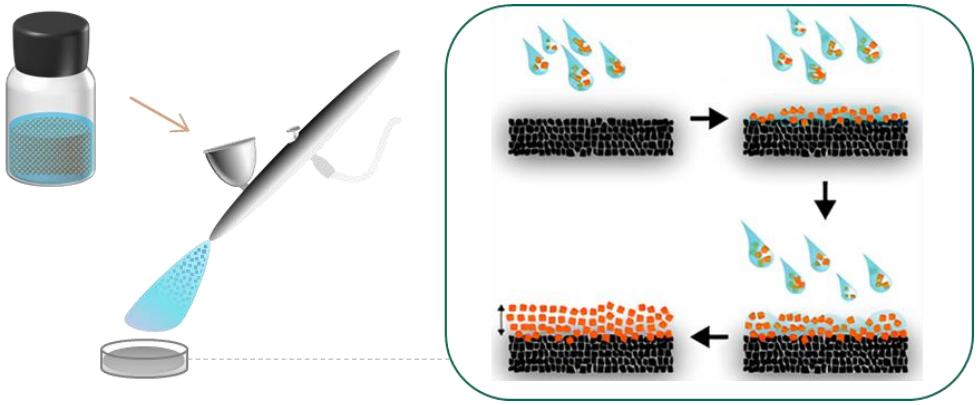

Figure 2.7: Schematic diagram of electrode preparation by the air spray method, adapted from reference [115].

All electrodes used in this work were prepared based on the above method by manually spraying the catalyst ink on the GDL via an Infinity CRplus spray gun (Harder

& Steenbeck) with nitrogen (99.99%, liquefied air) as a carrier gas. For the cathode, the catalyst ink was prepared by ultrasonically mixing 5 wt% Nafion solution (40 µL) and Ag or Cu nanopowder (30 mg) in isopropanol (2 mL) for 20 min. The ink was then manually sprayed onto carbon paper placed on a warm plate, which would form a catalyst mass loading of approximately 1.5 mg/cm^2. The area of the electrodes was 12 cm^2. For the anode, the catalyst ink was prepared by ultrasonically mixing 5 wt% Nafion solution (40 µL) and iridium oxide nanopowder (30 mg) in isopropanol (1 mL) and deionized water (1 mL) for 20 min. The ink was then manually sprayed onto platinum titanium fiber felt placed on a warm plate at 60 °C with a catalyst mass loading of approximately 1.5 mg/cm^2. The area of the electrodes was again 12 cm^2.

2.4.3 Membrane electrode assembly

The membrane electrode assembly, MEA, is the core component in a zero-gap electrolyzer. It usually consists of a cathode and an anode attached to both sides of a polymer electrolyte membrane, as shown in Figure 2.8. To increase the conductivity of the membrane, the membrane is usually pretreated, such as by immersing it in deionized water. Then the two electrodes coated with two catalysts prepared according to the previous description are placed in the gap of the cathode and anode spiral flow plates respectively, and then the pre-treated membrane is directly attached to the surface of the anode catalyst layer. In this way, the entire MEA is compacted directly in the reactor.

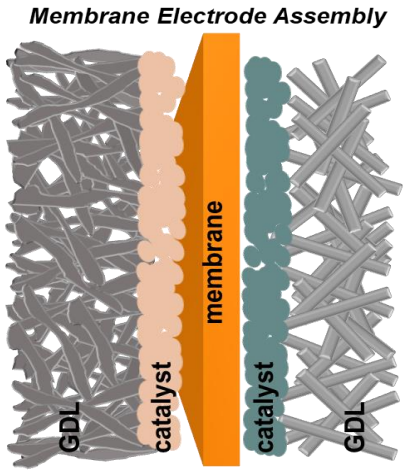

Figure 2.8: Schematic diagram of membrane electrode assembly components.

In this doctoral thesis work, three commercial ion exchange membranes were used to assemble MEAs for use in CO_2RR electrolyzers, including the Celtec proton exchange membrane, Nafion proton exchange membrane, and Sustainion anion exchange membrane. Their characteristics and pretreatment methods are shown in Figure 2.9. The cation exchange membrane Nafion 212 was immersed in the 5 wt.% H_2O_2 aqueous solution at 80 °C for 1 hour to eliminate organic impurities within the membrane. Subsequently, the membrane was rinsed repeatedly with deionized water and kept in deionized water at 80 °C for 1 hour to completely remove residual H_2O_2. Then, the membrane was immersed in a 1.0 M H_2SO_4 solution at 80 °C for 1 hour to convert the membrane to the H^+ form through ion exchange. Finally, the membrane was rinsed repeatedly with deionized water and soaked in deionized water for storage. The anion exchange membrane Sustainion X37-50 was fully immersed in a 0.5 M KOH solution for 12 hours until it separates from the substrate. It was then immersed in a bicarbonate solution for 48 hours to completely convert the membrane into carbonate or bicarbonate form. Before each use, the membrane was rinsed with deionized water.

Feature	Celtec Membrane	Nafion	Sustainion X37-50 Grade RT
Type	Cation exchange membrane	Cation exchange membrane	Anion exchange membrane
Chemical structure	Polybenzimidazole (PBI) doped with phosphoric acid	Perfluorosulfonic acid polymer (PFSA)	Cross-linked quaternary ammonium anion exchange polymer
Ionic conductivity	H^+/Phosphoric acid	H^+	OH^-
Maximum Operating Temperature	200°C	90°C	90°C
Pretreatment	No	Yes	Yes

Figure 2.9: Characteristics of the three ion exchange membranes used.

2.4.4 Physical characterizations

Surface morphology and microstructure of catalyst materials: Scanning Electron Microscope (SEM) can observe the surface structure and morphology of samples with high precision, including the particle size, morphology, and arrangement of the material. It can also perform qualitative and quantitative analysis of the chemical elements on the

surface of the sample through the energy-dispersive X-ray spectrometer (EDS or EDX). The surface characterization of the samples was carried out on a Gemini SEM 500 (Zeiss) instrument with a thermal Schottky field emission cathode, and energy dispersive X-ray spectrometer (EDS) mappings were obtained in a JEM-2100F (JEOL) Transmission instrument. SEM can be used to observe the cross-section of the material to understand the interface and bonding of materials at different levels. The thickness of the coating can be evaluated by scanning the cross-section of the sample. The cross-section images of the coated sample were collected from SEM (JXA 8530F, JEOL) instrument with different magnifications.

Crystal structure of materials: X-ray Diffraction (XRD) is a technique used to analyze the crystal structure of a substance. It detects the crystal structure of a material by irradiating X-rays onto the sample and analyzing the intensity and distribution of the scattered X-rays at different angles. The XRD experiments were conducted on a Bruker D8 Advance instrument equipped with a Sistrip detector (PSD Lynxeye©). The XRD data was acquired over a 2θ range of 10 to 90° with Cu Kα 1,2-radiation (λ= 0.154018 nm).

Distribution of catalysts: Wavelength Dispersive X-ray Spectroscopy (WDX) is a technique used to analyze the composition of materials. WDX testing determines the chemical composition of a sample by measuring the wavelength of characteristic X-rays emitted by elements in the sample. This method uses the unique wavelengths of X-rays emitted by different elements to achieve qualitative and quantitative analysis of elements. WDX (JXA 8530F, JEOL) was used to investigate the characterization of the cross-section of the catalyst layer on the GDL.

Wettability of electrode surface: Water Contact Angle Measurement is a technique used to evaluate the wettability of solid surfaces. Measuring the contact angle formed by a droplet on a solid surface can provide information about the hydrophilicity or hydrophobicity of the surface. If the water contact angle is greater than 90°, the droplet maintains a relatively rounded shape on the surface, indicating that the surface is hydrophobic. Apparent contact angles were measured using a Krüss Drop Shape Analyzer.

To measure surface wettability, a 5 μL droplet of deionized water was applied to the catalyst layer side for photographing and angle calculation.

2.5 Electrochemical performance

2.5.1 Electrochemical measurements

In this modified zero-gap MEA electrolyzer described above, the cell voltage is the potential difference between the cathode and the anode with no iR compensation. Linear scan voltammetry (LSV) was used to explore the working voltage of both half reactions in the electrolyzer and the response of the reaction rate (expressed as current) to changes in applied voltage. Chronopotentiometry (CP) was used to study the voltage input requirements of an electrolyzer at specific given currents, as well as its stability and Faradaic efficiency in long-term operation. All electrochemical CO_2 reduction tests in a zero-gap electrolyzer were recorded on a Biologic VSP-300 potentiostat with a 10 A booster. The aqueous anolyte was circulated by an HPLC pump with a flow rate of 30 mL min^{-1}. CO_2 was bubbled through a cylinder filled with water before entering the reactor, and the CO_2 was fed for 10 minutes before each electrolysis experiment to remove residual air. The flow rate of the CO_2 gas running into the cathode flow field was regulated by a mass flow controller (SLA5800 Series, Brooks) and another float-type flowmeter as outlet reference. Electrochemical impedance spectroscopy (EIS) measurements were performed at various currents with a voltage amplitude of 5 mV, and the frequency limits were set in the range from 100 kHz to 1 Hz. Fresh electrodes, membranes, and anolytes were used for each experiment to exclude deactivation effects from previous experiments.

2.5.2 CO_2RR product quantification

The composition of the output gas was analyzed by a gas chromatograph (SHIMADZU 2010 plus) with a packed HP-PLOT Q column. Ultra-high purity Ar gas (99.9999%) was used as the make-up gas. A flame ionization detector (FID) for C_1-C_3 gas quantification and a thermal conductivity detector (TCD) for H_2 quantification were installed in the gas chromatograph. The cathodic gas product was injected 3 times into

the GC at each applied voltage/current to obtain an average value. The signal response of the TCD and FID had been fixed by a range of commercial calibration standard gases.

2.5.3 Figures of merits

In the context of CO_2 electrochemical reduction, a comprehensive evaluation of process performance is conducted through the utilization of multiple quality factors, encompassing current density, Faradaic efficiency, energy efficiency, stability, and economic considerations.

Cell voltage

In an electrolyzer, the voltage is the potential difference between the anode and cathode, driving the electrochemical reaction of CO_2 reduction during electrolysis. The theoretical voltage refers to the minimum voltage required to complete the electrolysis reaction under ideal conditions, without accounting for any losses. However, in practical operation, the actual voltage is typically higher than the theoretical voltage due to various losses in the system, including Ohmic losses, electrode polarization, and bubble effects. Therefore, a lower electrolyzer voltage indicates fewer overall voltage losses and reduced energy consumption at the same current density, which improves the energy efficiency of the electrolysis process and lowers production costs.

Current density

The current density in CO_2RR serves as a characterization of the kinetics of a specific electrocatalytic reaction, effectively reflecting the reaction rate under given conditions [86]. This parameter is determined by measuring the current value per unit area of the working electrode at a specific operating voltage.

$$j = \frac{I}{S} \tag{2.1}$$

where I is the total current value (A) and S is the area of the working electrode (cm^2). Higher current density means faster reaction rate per unit area of the electrode, allowing for more products to be generated in a shorter time. Therefore, an electrolyzer that can

sustain higher current density will have greater production capacity. In summary, the design goal of an electrolyzer is to achieve high current density at low voltage, thereby increasing output while maintaining high energy efficiency.

Faradaic efficiency

Faradaic efficiency (FE) reflects the selectivity of the current to a specific CO_2RR product. It quantifies the ratio of the charge transferred to the specified target product to the total charge consumed during the reaction. It can be calculated using the following equation:

$$FE_i = \frac{Q_i}{Q_{total}} \times 100\% = \frac{n_i \times v \times x_i \times \frac{Fp}{RT}}{I \times t} \times 100\% \quad (2.2)$$

where n_i is the number of transferred electrons for each product *(i)*; 2 for CO, 8 for CH_4, 12 for ethylene, and 18 for propene. And v is the flow rate of outlet gas, x_i is the volume fraction of specific product determined by gas chromatography, F is the Faradaic constant, p is the pressure, T is the room temperature and R is the ideal gas constant with a value of 8.314 J/(mol·K), I is the applied current and t is the time. A high Faradaic efficiency implies that the current is more effectively utilized for the generation of the desired products, enhancing reaction selectivity and efficiency. This concurrently reduces the total current required for achieving the target production rate, consequently mitigating additional costs associated with product separation and purification.

Energy efficiency

The energy efficiency (EE) of an electrolyzer provides a quantitative measure of how effectively electrical energy is converted into chemical energy stored in the reaction products. In electrochemical systems, energy efficiency can be defined with respect to different thermodynamic reference states, depending on whether only electrical work or the total reaction energy demand is considered. In general, two approaches are commonly employed in literature [86, 116]. One is based on the Gibbs free energy change (ΔG), corresponding to the reversible cell voltage E_{rev} (E_{rev}=ΔG/nF), while another one is based on the reaction enthalpy (ΔH), corresponding to the thermoneutral voltage E_{tn}

(E_{tn}=ΔH/nF). The relationship between ΔG and ΔH is expressed as ΔH=ΔG+TΔS, with T being the absolute temperature and ΔS the entropy changes of the reaction. The ΔG-based formulation represents the minimum electrical energy required under ideal reversible conditions and is therefore commonly used to assess the intrinsic electrochemical efficiency of an electrolyzer. In contrast, the ΔH-based formulation accounts for the total reaction energy demand, including both electrical and thermal contributions, and corresponds to operation under thermoneutral conditions, where reaction heat is fully compensated by electrical input. In practical electrochemical systems, side reactions are unavoidable, and not all transferred charge contributes to the formation of the desired product [117]. The energy efficiency can therefore be expressed as

$$EE_i = \frac{E_{rev}}{E_{cell}} \times FE_i = \frac{\Delta G \times FE_i}{nFE_{cell}} \tag{2.3}$$

when referenced to ΔG, and

$$EE_i = \frac{E_{tn}}{E_{cell}} \times FE_i = \frac{\Delta H \times FE_i}{nFE_{cell}} \tag{2.4}$$

when referenced to ΔH; where E_{cell} denotes the measured cell voltage and n is the number of electrons transferred to form the product (i). The choice between these two definitions depends on the system configuration and the intended scope of analysis. The ΔG-based efficiency reflects purely electrical performance and is appropriate when thermal effects are negligible or when external heat input is explicitly accounted for. The ΔH-based approach, on the other hand, is typically employed for system-level energy assessments, particularly in thermally integrated or high-temperature electrolyzers.

In this dissertation, the electrolyzer operated under externally controlled temperatures ranging from 25°C to 180°C, with thermal energy supplied independently from the electrochemical workstation. Throughout this dissertation, energy efficiency is calculated based on the reaction enthalpy, corresponding to the thermoneutral voltage. As the external thermal input was not quantified, the reported values do not represent purely electrical efficiency but rather an apparent thermoneutral energy metric, providing an

upper-bound estimate of the overall system performance. This definition is applied consistently across all experiments to enable meaningful comparison between different operating conditions.

System stability

The stability of CO_2RR demonstrates the ability of the electrolyzer, especially the catalysts, to maintain high activity and selectivity under prolonged constant current or potential polarization. However, comprehensive investigations into the long-term CO_2RR performance remain limited, with most reports indicating testing durations typically less than 100 hours [118, 119]. It is noteworthy that achieving high stability in CO_2RR requires the durability of all components within the electrolysis cell, encompassing the catalyst, electrodes, electrolyte, ion-exchange membrane, and the cell itself. Specifically, the cathode may undergo gradual loss of active sites, poisoning, or irreversible structural degradation under rigorous CO_2RR conditions. Long-term stability is crucial for minimizing maintenance and replacement costs, as well as reducing associated downtime of the electrolysis cell, particularly when scaling up reactor operations [120].

3 Microenvironment Engineering

3.1 Insights of CO_2-to-CO with anion exchange membrane

The product carbon monoxide (CO) from CO_2RR serves as a versatile and fundamental industrial feedstock, with applications in the synthesis of various chemicals. It is the main constituent of syngas, which can be converted into methanol and even sustainable aviation fuels [121-123]. However, the current development of CO_2RR technology still faces the issue of excessive energy consumption, and it is necessary to improve the efficiency of converting electrical energy into chemical energy as well as the activity and selectivity of the reaction and the stability of the electrodes.

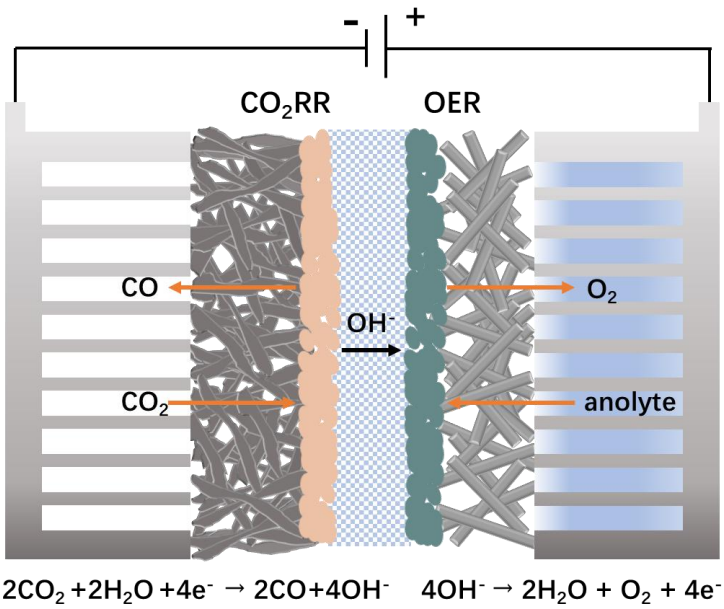

Figure 3.1: Schematic representation of a zero-gap AEM-MEA electrolyzer.

A schematic representation of a zero-gap AEM-MEA electrolyzer is shown in Figure 3.1. The main function of the anion exchange membrane is to allow hydroxide ions (OH^-) to pass through the membrane from the cathode region to the anode while preventing unnecessary substances (such as gases, and liquids) from passing through. This maintains the charge balance in the system so that the electrolysis reaction can continue. The AEM also effectively separates the reaction areas of the anode and cathode,

preventing the generated gases (such as O_2 at the anode and CO at the cathode) from mixing and avoiding side reactions. This helps to improve the purity of the product and the selectivity of the reaction.

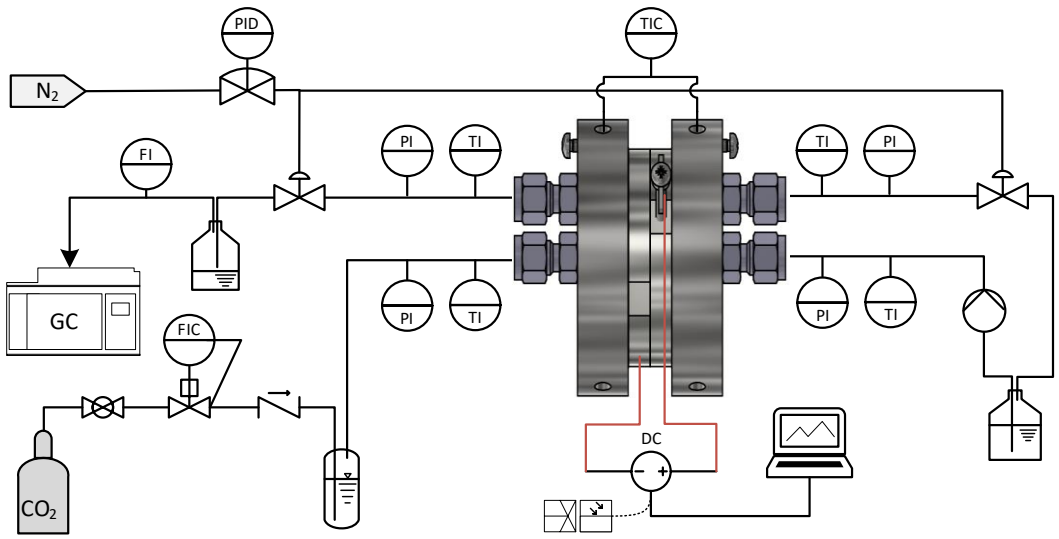

Figure 3.2: P&ID of the setup for electrocatalytic reduction of CO_2 with a zero-gap electrolyzer.

This zero-gap electrolyzer configuration featuring adjacent electrodes, in which the catholyte is omitted, is aimed to minimize ohmic resistance and activate catalytic reactions with a low overpotential [19, 124, 125]. This setup also permits direct contact between the catalyst and the ion exchange membrane, which not only improves mass transport dynamics but also preserves electrode integrity [45, 90, 126]. As gaseous CO_2 and liquid anolyte flow through the zero-gap electrolyzer, the formation of a stable three-phase contact at the solid catalyst interface emerges as the cornerstone for efficient and enduring CO_2 reduction reactions [91]. To provide long-term operational stability, it is nassessary to avoid flooding of the electrode and precipitation of solid carbonates in the cathode [64, 80]. Moreover, a comprehensive assessment of the overall energy efficiency of the zero-gap electrolyzer system is of significance. Both stability and energy efficiency are the key indicators for evaluating the scalability and economic feasibility of CO_2RR technology [53, 112]. The P&ID of the proposed CO_2 electroreduction system based on a zero-gap electrolyzer is shown in Figure 3.2.

3.2 Characterization of Ag and IrO_2 electrodes

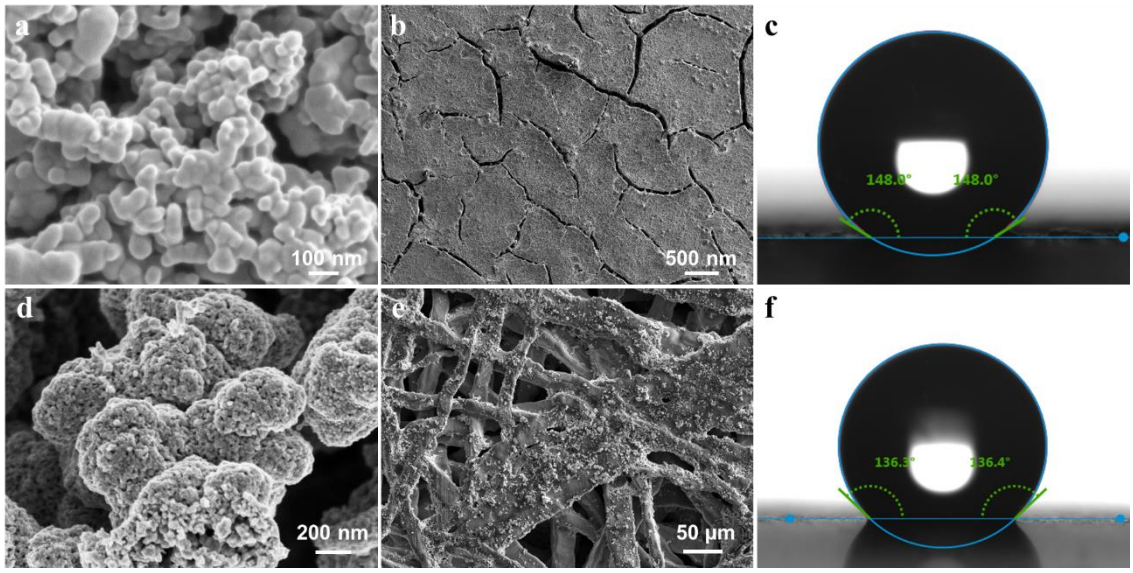

Figure 3.3: SEM photos of (a) silver nanocatalysts, (b) air-sprayed Ag@C electrode from the top view. (c) Water contact angle photo of fresh Ag@C electrode. SEM photos of (d) IrO_2 nanocatalysts, (b) Air sprayed IrO_2@Ti electrode from top view. (c) Water contact angle photo of fresh IrO_2@Ti electrode.

As depicted in Figure 3.3a, the commercial silver nanoparticle catalyst possesses a primary particle size ranging from approximately 50 to 100 nm, which can be clearly identified in the SEM image. The top-view SEM image of the cathode electrode (Figure 3.3b) demonstrates that the Ag catalyst is evenly distributed across the surface of the carbon GDL. Initially, the Ag@C electrode on the catalyst-facing side displays a water contact angle of 148° (Figure 3.3c), indicating strong hydrophobicity that facilitates efficient gas diffusion and promotes the formation of a stable three-phase interface at the cathode [127, 128]. SEM images presented in Figures 3.3d and 3.3e illustrate that IrO_2 catalyst nanoparticles are deposited onto the titanium fiber substrate via air spraying, thereby forming the IrO_2@Ti anode. On the catalyst-facing side of the fresh IrO_2@Ti electrode, the measured initial water contact angle is 136.3° (Figure 3.3f), which accelerates oxygen release through the porous framework.

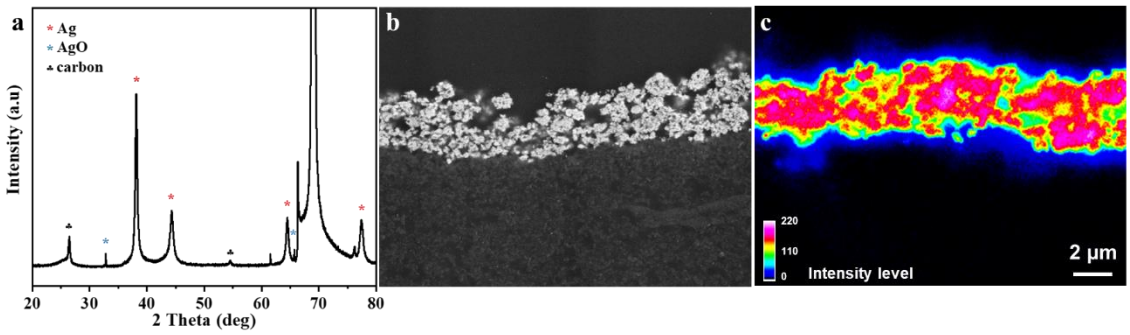

Figure 3.4: (a) XRD pattern, (b) cross-sectional SEM image, and (c) intensity distribution of air-sprayed Ag@C electrode.

The crystalline structure and phase composition of the catalysts were characterized using XRD, as depicted in Figure 3.4a. The diffraction peaks observed at 38.1°, 44.3°, 64.4°, and 77.4° correspond to the (111), (200), (220), and (311) planes of Ag, respectively, in accordance with JCPDS No. 04-0783 [129, 130]. Cross-sectional SEM imaging (Figure 3.4b) reveals that the spray-deposited Ag catalyst layer on the GDL exhibits a uniform thickness of approximately 5 μm, with no evident aggregation of catalyst particles. This uniformity is attributed to the fine dispersion of ink droplets and the rapid evaporation of solvent during the spraying process, which together promote the formation of a well-defined and homogeneous layer. Furthermore, the intensity profile shown in Figure 3.4e confirms a homogeneous vertical distribution of Ag nanoparticles relative to the GDL surface. An appropriately thick catalyst layer not only maximizes the number of electrochemically active sites for CO_2RR but also effectively prevents direct electrical contact between the ion-exchange membrane and the uncovered carbon substrate of the GDL [131].

3.3 Effect of temperature on the alkaline system

A catholyte-free MEA configuration utilizing 1 M KOH as the flowing anolyte demonstrates a high reaction rate, delivering a current of 4.5 A at a cell voltage of 4 V under ambient conditions, as shown in the LSV profiles in Figure 3.5. When the operating temperature is elevated to 80 °C, the current increases substantially to 7 A at the same cell voltage. It is important to note that the operating temperature for membranes should

remain below 90 °C to avoid reduced proton conductivity and potential flooding due to enhanced water crossover [120, 132].

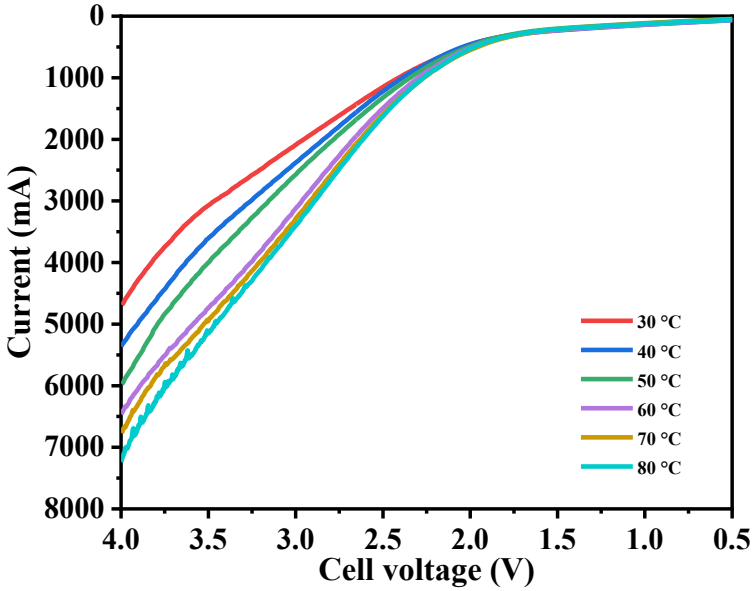

Figure 3.5: LSV curves of CO_2RR at a scan rate of 30 mV/s in the MEA catholyte-free system with 1 M KOH anolyte at different temperatures.

Figure 3.6a illustrates the influence of three typical operating temperatures on the cell voltage across a range of current densities, as determined by chronopotentiometric measurements. At ambient temperature (25 °C), the CO_2RR attains a total current of 1.2 A (equivalent to a current density of 100 mA/cm^2) at a cell voltage of 3.0 V. Elevating the temperature leads to a decrease in reaction overpotential, with the corresponding cell voltage reduced to 2.6 V at 50 °C and further to 2.4 V at 80 °C. At a higher total current of 3.0 A (250 mA/cm^2), the cell voltage required at room temperature is 3.63 V, whereas only 2.97 V is necessary at 80 °C. Figure 3.6b presents the CO volume fraction, determined by gas chromatography based on the effluent CO_2 stream. When operated at 100 mA/cm^2, the CO_2RR yields a comparable CO volume fraction of approximately 8% to 9% across the tested temperatures. As the current density rises, the CO volume fraction correspondingly increases, reaching up to 20%.

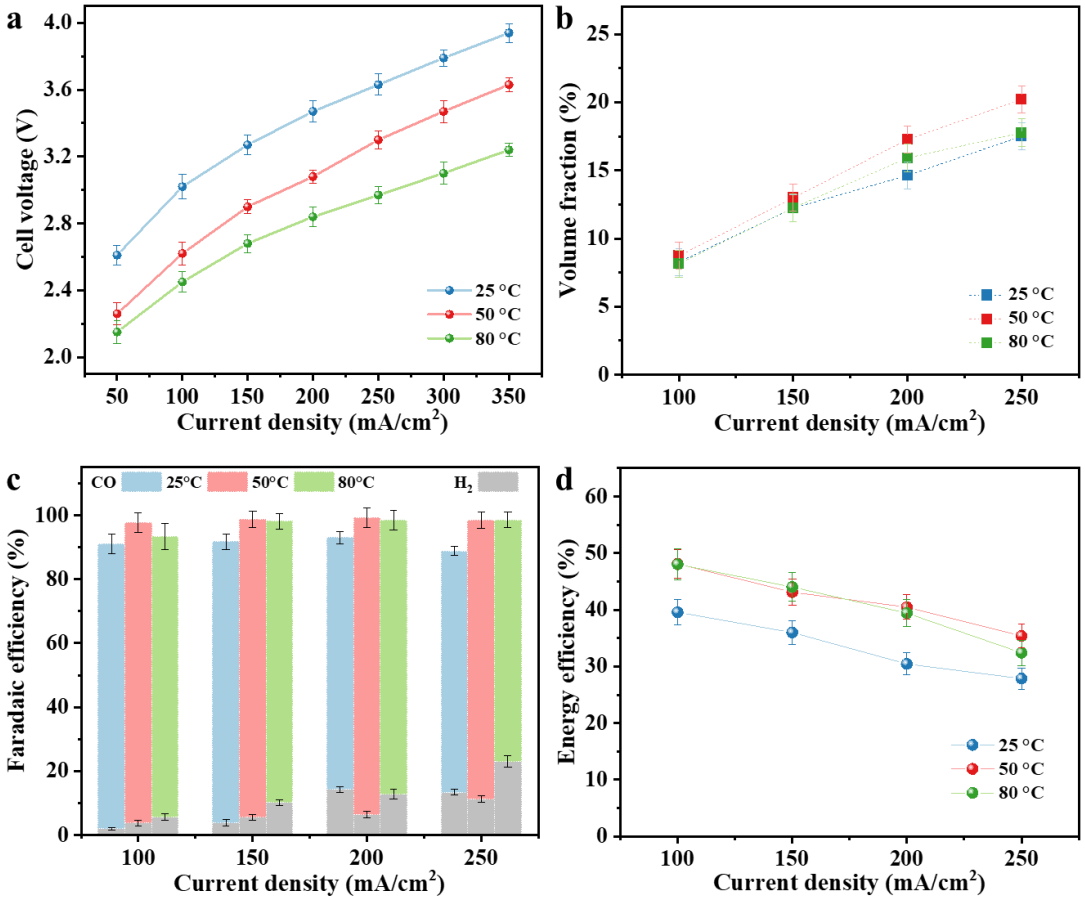

Figure 3.6: CO_2RR performance with 1 M KOH anolyte in the modified zero-gap electrolyzer at given temperatures. (a) Polarization curves. (b) Volume fractions of CO in the product gas. (c) Faradaic efficiencies of CO and H_2. (d) Calculated energy efficiency for CO production.

Figure 3.6c illustrates the FE_{CO} values at different temperatures, which are calculated based on the volumetric proportion of CO. At ambient temperature, the CO_2RR exhibits an FE_{CO} of 89.1% at a current density of 100 mA/cm^2. Although higher current densities promote the competing HER, an FE_{CO} of 75.4% is still maintained at 250 mA/cm^2. When the temperature is elevated to 50 °C, the system continues to demonstrate excellent selectivity toward CO, with FE_{CO} values ranging from 93.0% to 94.0% across 100–200 mA/cm^2, and a value of 87.1% at 250 mA/cm^2. At 80 °C, even with minimal applied voltage, FE_{CO} remains within 85.7%–88.0% for current densities between 100 and 200 mA/cm^2, and 76.5% at 250 mA/cm^2. In general, attaining high selectivity toward the desired product under reduced voltage conditions indicates an

improvement in the system's energy utilization (see Figure 3.6d). The absence of catholyte and the unobstructed mass transfer contribute to an energy efficiency of 43.3% and 33.3% for the CO_2RR at 100 and 200 mA/cm^2, respectively, at room temperature. At 50 °C, elevated FE_{CO} enhances energy efficiency to 52.6% at 100 mA/cm^2 and 44.3% at 200 mA/cm^2. Similarly, at 80 °C, comparable efficiencies of 52.5% and 43.1% are achieved under reduced voltage conditions.

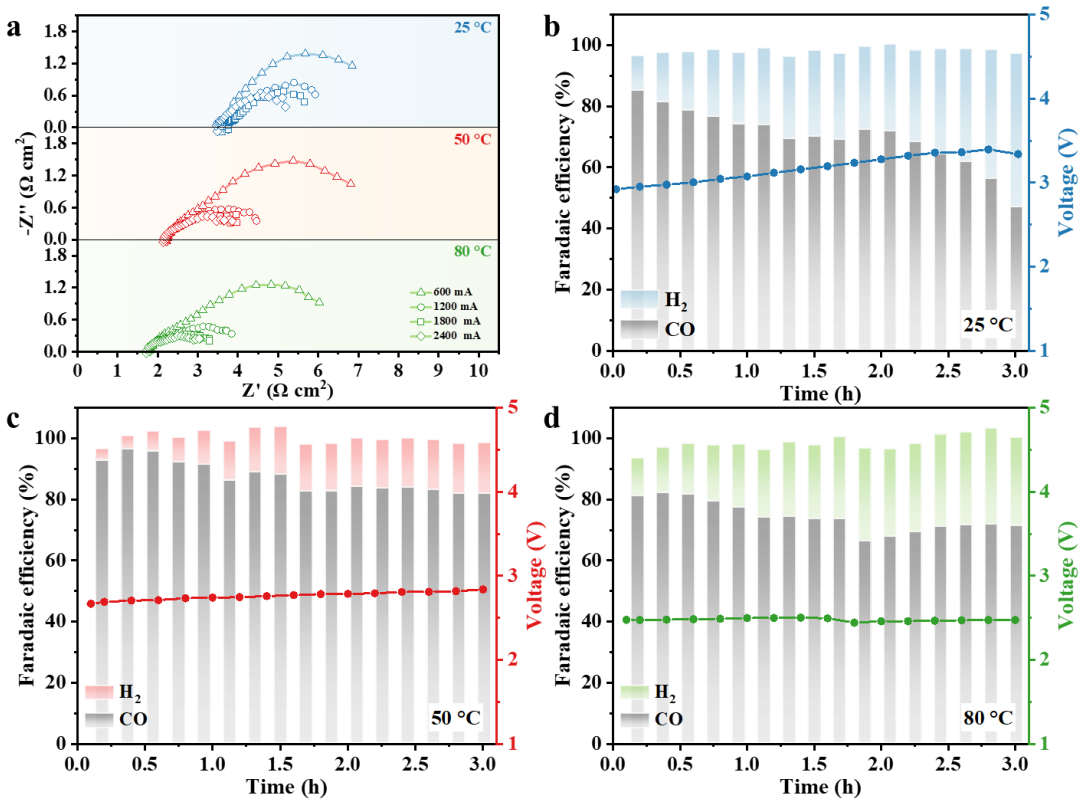

Figure 3.7: CO_2RR performance with 1 M KOH anolyte in the modified zero-gap electrolyzer at given temperatures. (a) Nyquist plots at each current density under operating temperatures of 25 °C, 50 °C, and 80 °C. Then the recorded cell voltages and corresponding FE_{CO} at a current level of 1.2 A during 3 hours of operation under operating temperatures of (b) 25 °C, (c) 50 °C, and (d) 80 °C.

To gain deeper insight into the temperature-dependent behavior of CO_2RR within the zero-gap electrolyzer, EIS measurements were carried out. As illustrated in Figure 3.7a, the high-frequency intercept on the real axis decreases with increasing temperature,

indicating a significant reduction in ohmic resistance. This behavior is mainly attributed to the enhanced ionic conductivity of the electrolyte at elevated temperatures, following Arrhenius-type thermal activation. In addition, higher temperature improves interfacial contact and accelerates charge carrier transport, further contributing to the decrease of ohmic resistance. The consistent observation that higher operational temperatures correspond to reduced cell voltages is advantageous for electrolyzers targeting commercial-scale current densities and improved energy efficiency in the future [133]. From a practical standpoint, residual heat from adjacent industrial processes is often sufficient to maintain CO_2 electrolyzer operation at temperatures up to 80 °C [134].

Table 3.1: EDX of Ag@Carbon electrodes after 3 hours with 1 M KOH anolyte at different temperatures.

	A%(C)	A%(O)	A%(F)	A%(K)	A%(Ag)
25 °C	36.3161	4.65	3.3218	4.64	51.0722
50 °C	16.2386	7.9322	4.6915	6.1788	64.9589
80 °C	16.9863	7.0324	2.7098	7.1605	66.111

Under a constant current of 1.2 A during CO_2RR, Figure 3.7 reveals a gradual reduction in FE_{CO} across all evaluated temperatures, whereas a notable increase in cell voltage is only observed at ambient conditions. Nevertheless, after approximately three hours, the reaction was interrupted due to pressure instability within the reactor, traced back to solid deposits obstructing the cathode flow channels. SEM analysis of the utilized Ag@Carbon electrodes, shown in Figure 3.8, indicates no substantial alteration in microscale morphology compared to the pristine state. However, surface EDX (Table 3.1) confirms the accumulation of potassium on the electrode, likely resulting from electrolyte infiltration driven by concentration and electric field gradients. This phenomenon promotes flooding and carbonate precipitation [135], ultimately disrupting the gas–liquid equilibrium during electrolysis. Simultaneously, the formation of carbonate species imparts hydrophilic characteristics to the electrode surface [136, 137]. This is reflected in the significant decrease in water contact angles on the catalyst-facing side of the Ag/C electrode after 3 h: 63° (25 °C), 83° (50 °C), and 64° (80 °C), as presented in Figure 3.8.

These findings indicate extensive flooding and an increasing dominance of the HER over time.

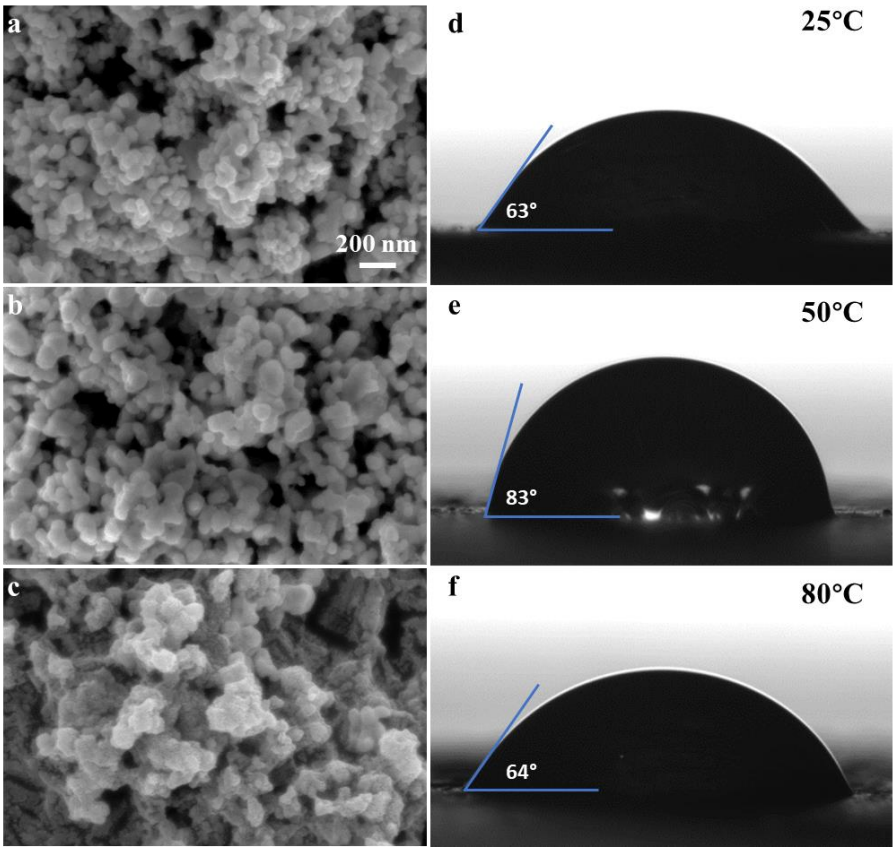

Figure 3.8: SEM of Ag@Carbon electrodes after 3 hours in the MEA reactor with 1 M KOH anolyte at (a) 25 °C, (b) 50 °C, and (c) 80 °C. Water contact angle photos of Ag@Carbon electrodes after 3 hours in the MEA reactor with 1 M KOH anolyte at (d) 25 °C, (e) 50 °C, and (f) 80 °C.

3.4 Effect of pressure on the alkaline system

It is important to note that numerous chemical processes employing CO as a reactant necessitate high-pressure conditions [138]. Alternatively, pressurizing the CO_2 feed can serve to increase the local CO_2 concentration within the catalyst layer [139], thereby inducing a positive shift in the onset potential observed in the LSV profiles (Figure 3.9), in contrast to those obtained under ambient pressure (Figure 3.5).

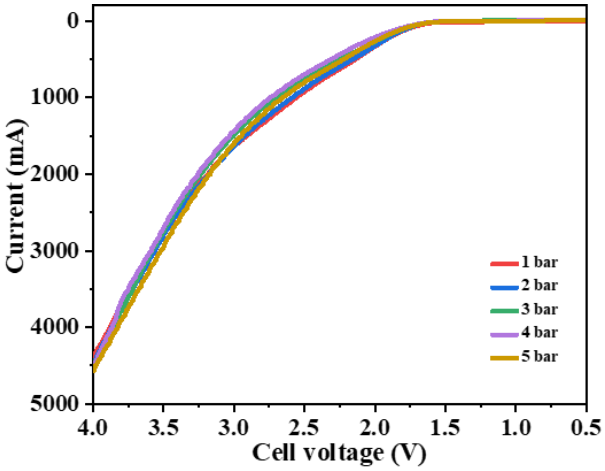

Figure 3.9: LSV curves of CO_2RR at a scan rate of 30 mV/s in the MEA reactor with 1 M KOH anolyte under different pressures.

This finding is further corroborated by galvanostatic tests, which reveal a reduction in cell voltage from 3.02 V at 100 mA/cm^2 under ambient conditions (see Figure 3.6a) to below 2.8 V upon the application of pressure (Figure 3.10a). In comparison to CO_2RR conducted at atmospheric pressure, the volume fraction of CO produced exhibits a noticeable increase within the 1–5 bar pressure range (Figure 3.10b). The enhancement in CO_2 concentration within the catalyst layer due to pressurization contributes to higher single-pass conversion rates and an elevated Faradaic efficiency for CO production [140]. As illustrated in Figure 3.10c, the total Faradaic efficiency approaches 100% across all examined current densities, indicating that the upgraded reactor design with a finely tuned sealing system supports stable performance and ensures the accuracy of measurements under rigorous operational conditions. Ensuring sufficient CO_2 availability is particularly critical at elevated current densities, where the demand for reactants is significantly increased to sustain efficient conversion. Moreover, as presented in Figure 3.10d, the energy efficiency under pressurized conditions ranges from 49.0% to 51.7% at 100 mA/cm^2 and from 31.2% to 35.4% at 250 mA/cm^2, which can be attributed to improved Faradaic efficiency and decreased cell voltage. Consequently, performing CO_2 electrolysis under pressure represents a promising strategy to directly obtain CO at the desired delivery pressure for subsequent utilization.

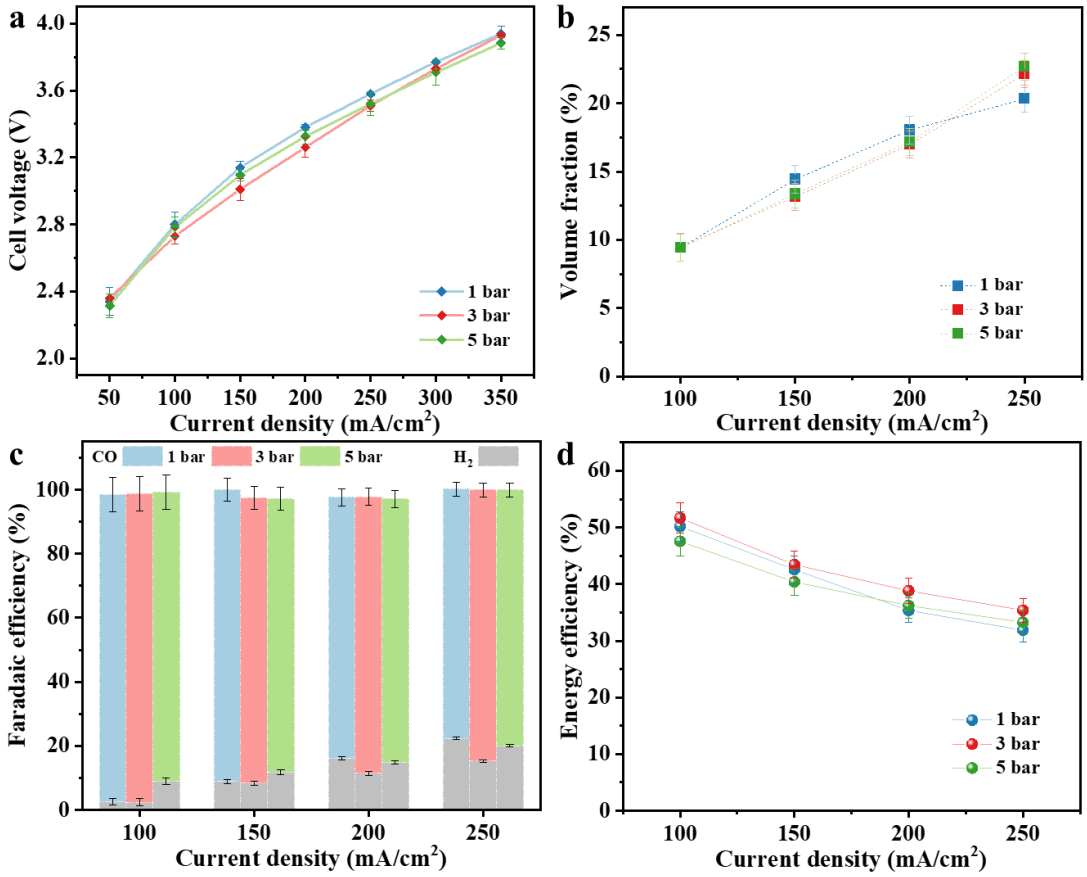

Figure 3.10: CO_2RR performance with 1 M KOH anolyte in the modified zero-gap electrolyzer at given pressures. (a) Polarization curves. (b) The volume fractions of CO product. (c) Faradaic efficiencies of CO and H_2. (d) Calculated energy efficiency for CO production.

The above evaluation suggests that CO_2RR conducted in a MEA configuration under alkaline conditions holds substantial promise for achieving higher catalytic activity. Enhancing system temperature and pressure has been widely acknowledged as a viable means to improve both CO selectivity and overall energy efficiency. Prior studies have demonstrated that alkaline electrolytes can effectively suppress the hydrogen evolution reaction, thereby favoring CO_2RR selectivity [92, 141]. However, it is important to consider that CO_2 is transformed into HCO_3^-/CO_3^{2-} species within alkaline media, leading to a gradual neutralization of pH. This process results in carbonate precipitation, which subsequently hinders CO_2 transport and diffusion, facilitates hydrogen evolution, and contributes to a progressive decline in current density over extended operation periods

[134, 142]. Given that alkali metal-containing electrolytes support the generation of comparable current densities at reduced applied voltages due to their high ionic conductivity [64], the potential for sustained operation is currently being investigated using mildly alkaline systems.

3.5 Long-term operation in neutral system

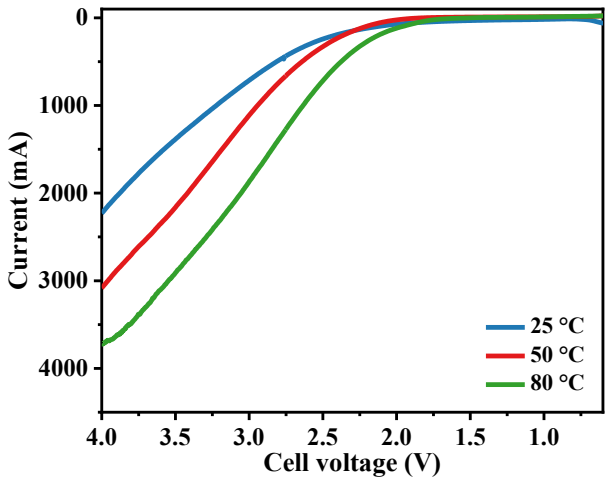

Figure 3.11: LSV curves of CO_2RR at a scan rate of 30 mV/s in the MEA reactor with 0.1 M $KHCO_3$ anolyte under different temperatures.

Employing a milder electrolyte appears to be a viable approach to mitigate carbonate precipitation issues in zero-gap electrolyzers. $KHCO_3$ solution represents another commonly utilized electrolyte, recognized for its superior buffering capacity [143]. According to the LSV curves shown in Figure 3.11, the catholyte-free MEA configuration utilizing 0.1 M $KHCO_3$ as the anolyte exhibits an increased reaction rate at elevated temperatures, with the current rising from 2.2 A at 25 °C to 3.7 A at 80 °C while maintaining a constant cell voltage of 4 V. The higher cell voltage observed compared to a 1 M KOH alkaline electrolyte is attributed to the reduced ionic conductivity of HCO_3^- relative to OH^- and the slower reaction kinetics occurring within a microenvironment characterized by lower cation concentration and pH [144, 145].

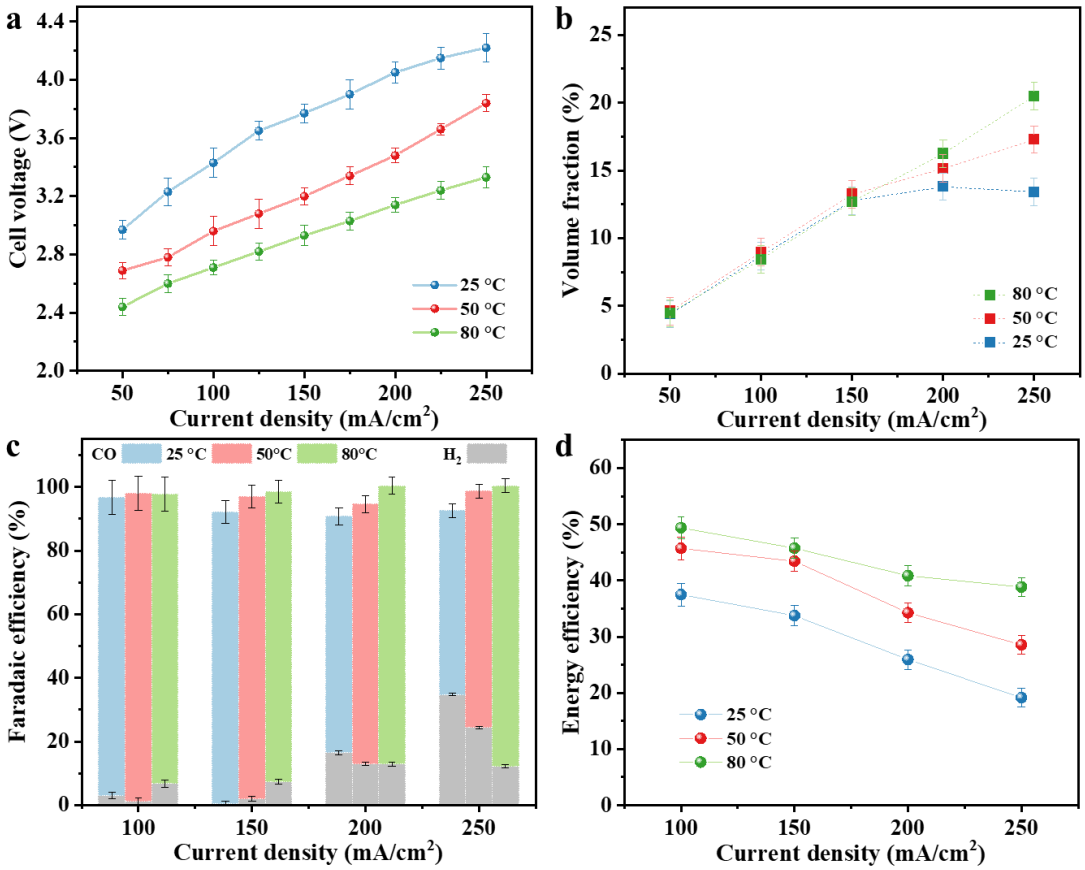

Figure 3.12: CO_2RR performance with 0.1 M $KHCO_3$ anolyte in the modified zero-gap electrolyzer at given temperatures. (a) Polarization curves. (b) Volume fractions of CO in the product gas. (c) Faradaic efficiencies of CO and H_2. (d) Calculated energy efficiency.

Operating the electrolyzer at a current density of 200 mA/cm^2 results in cell voltages of 4.05 V, 3.48 V, and 3.14 V at temperatures of 25 °C, 50 °C, and 80 °C respectively (Figure 3.12a), emphasizing the temperature sensitivity of the CO_2RR process. Figure 3.12b shows that the volume fraction of CO increases with increasing current density, and that higher CO yield can be maintained at higher temperatures under high current test conditions. Figure 3.12c reveals that FE_{CO} decreases from approximately 93.5% to 57.8% at room temperature when the operating current density rises from 100 to 250 mA/cm^2. Despite a modest increase in HER at higher current densities under elevated temperatures, the MEA maintained an FE_{CO} of 88.2% at 250 mA/cm^2 and 80 °C. Figure 3.12d indicates that energy efficiency improves with increasing temperature for

any given current density. Specifically, the MEA system's energy efficiency approaches 49.4% at 80 °C and 100 mA/cm^2, and remains above 40.8% at 200 mA/cm^2. When the elevated operating temperature adequately compensates the thermal demand for CO_2-to-CO conversion, the requirement for electrical energy correspondingly diminishes [146].

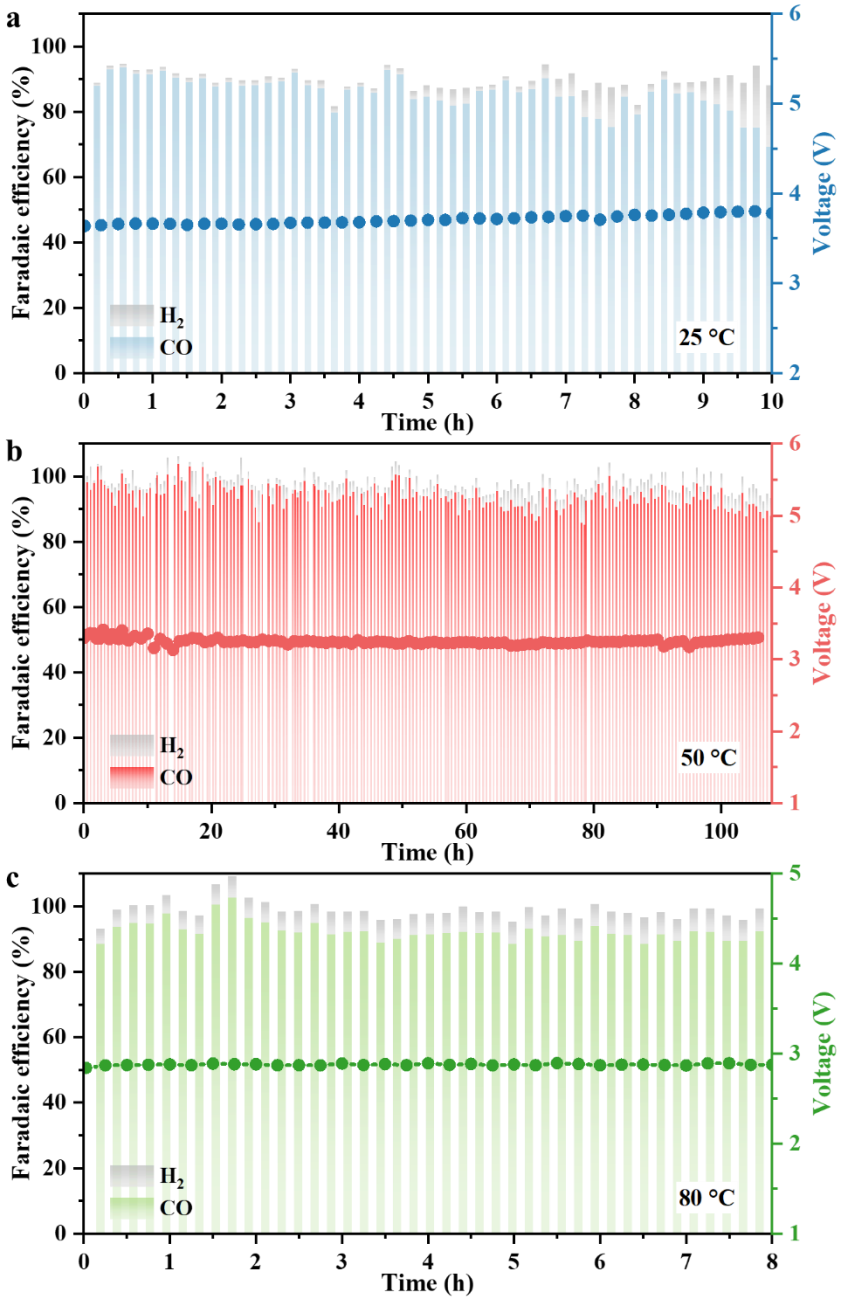

Figure 3.13: Electrochemical stability test at a working current of 1.2 A in 0.1 M $KHCO_3$ anolyte under operation temperatures of (a) 25 °C, (b) 50 °C and (c) 80 °C.

To verify the stability of neutral CO_2RR in a zero-gap electrolyzer, extended testing was performed at 100 mA/cm^2 (total current 1.2 A) with cycling of 0.1 M $KHCO_3$ anolyte. During 10 hours of operation at ambient temperature, the input voltage shows a gradual increase while FE_{CO} slightly decreases, as illustrated in Figure 3.13a. At 80 °C, the voltage stabilizes at approximately 2.9 V and FE_{CO} fluctuates near 90% over 8 hours (Figure 3.13c). Both experiments concluded due to a rising pressure difference inside the reactor. Further observations revealed cathode GDL flooding at room temperature after 10 hours, whereas carbonate accumulation blocked the microchannels after 8 hours at 80 °C. Notably, at 50 °C the system sustains a stable voltage of 3.2 V for more than 100 hours with FE_{CO} above 90% (Figure 3.13b).

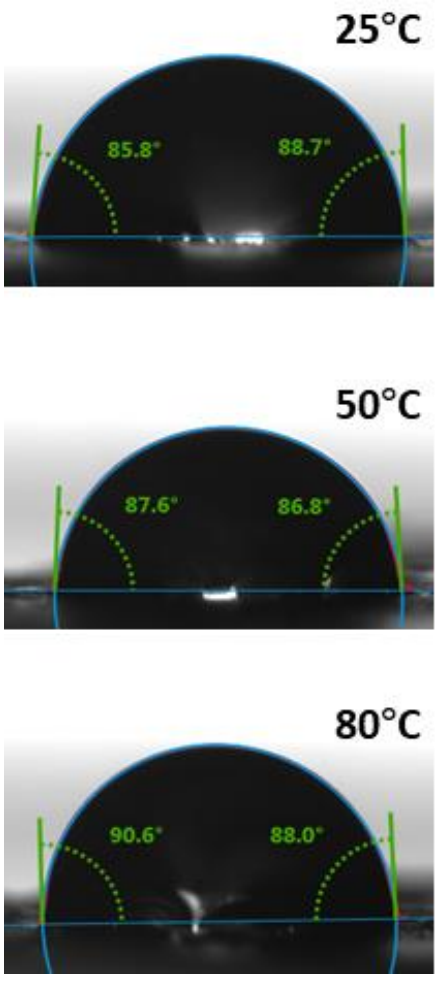

Figure 3.14: Water contact angle photos of the tested Ag@Carbon electrodes with 0.1 M $KHCO_3$ anolyte at 25 °C, 50 °C, and 80 °C.

Table 3.2: EDX of Ag@Carbon electrodes after 5 hours with 0.1 M $KHCO_3$ anolyte.

	A%(C)	A%(O)	A%(F)	A%(K)	A%(Ag)
25 °C	22.8888	6.0383	4.7801	3.4128	62.8799
50 °C	20.0099	11.0718	4.1443	3.9341	60.8399
80 °C	20.5304	11.1842	4.1674	4.1619	59.9561

The water contact angle measurement of the Ag@Carbon electrode after use confirms that hydrophobicity was preserved, as shown in Figure 3.14. EDX analysis (Table 3.2) detected trace potassium on the cathode GDL surface.

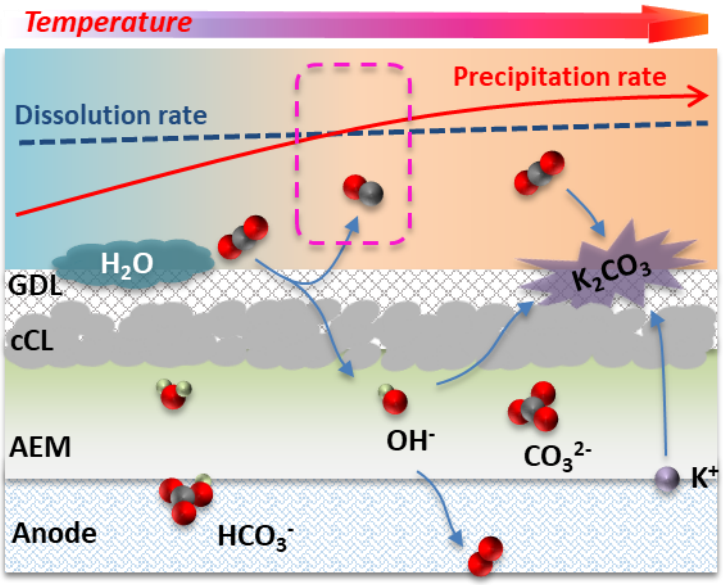

Figure 3.15: Schematic depiction of the dynamic dissolution and precipitation process.

Figure 3.15 presents a schematic representation of the dynamic processes within the zero-gap electrolytic cell, emphasizing temperature effects on dissolution and precipitation rates. During electrolysis, potassium ions migrate electrically to the cathode, interacting with the alkaline microenvironment and promoting carbonate formation. Concurrently, water vapor is introduced alongside a humidified CO_2 stream. At ambient temperature, some vapor condenses within cathode channels, which can dissolve carbonate deposits but also leads to flooding over time. Increasing temperature accelerates both electroreduction reactions and carbonate precipitation, while reducing vapor condensation at the cathode. Consequently, less carbonate dissolves, allowing

greater accumulation if the reactor temperature becomes excessive. At an optimal temperature, a steady-state balance between carbonate generation and dissolution is achieved, where the interplay of mass and heat transfer dynamics underpins the improved efficiency and long-term stability of the system. Therefore, precise temperature regulation to control the solid/gas/liquid microenvironment within the catalyst layer is critical for ensuring durable, efficient, and stable CO_2 electrolysis.

3.6 Effect of pressure on the neutral system

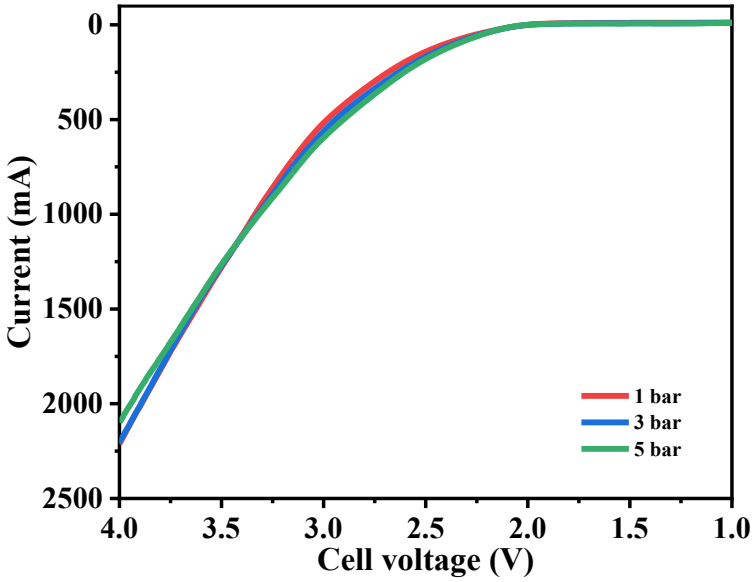

Figure 3.16: LSV curves of CO_2RR at a scan rate of 30 mV/s in the MEA reactor with 0.1 M $KHCO_3$ anolyte under different pressures at room temperature.

The LSV curves obtained in a neutral electrolyte indicate that elevating the pressure beyond atmospheric levels does not enhance the overall reaction rate, as illustrated in Figure 3.16. No substantial variation is observed in the CO_2RR reaction rate within the pressure range of 1 to 5 bar, as shown in Figure 3.17a, nor in the volume fraction of CO product depicted in Figure 3.17b. FE_{CO} remains nearly complete, alongside a pronounced suppression of the HER, particularly under conditions of high current density, as demonstrated in Figure 3.17c. The improved energy efficiency of pressurized CO_2RR systems, emphasized in Figure 3.17d, results from enhancements in Faradaic efficiency coupled with a reduction in cell voltage. This configuration achieves steady energy

efficiencies ranging from 43.1% at 1.2 A to 37.9% at 2.4 A, which surpass the efficiencies recorded at room temperature and atmospheric pressure (37% and 26%, respectively) in Figure 3.12d.

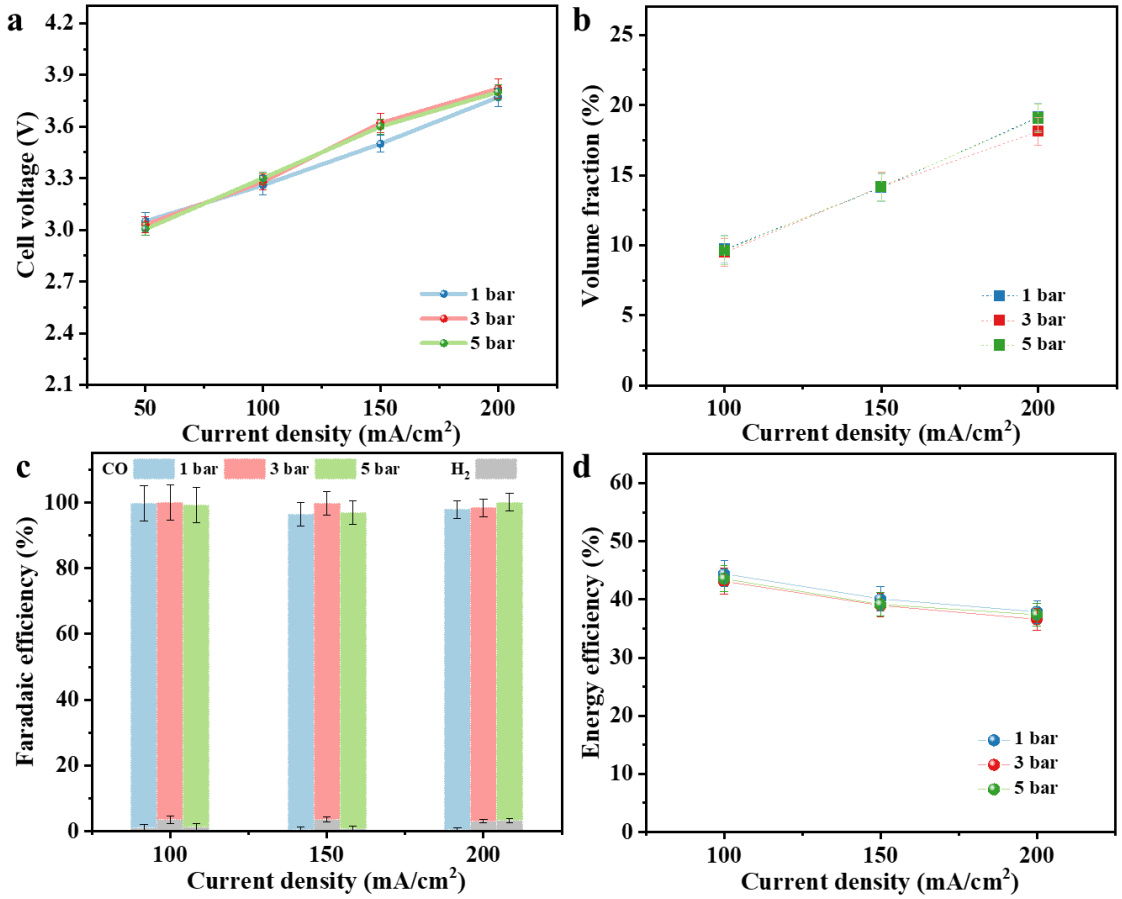

Figure 3.17: CO_2RR performance with 0.1 M $KHCO_3$ anolyte in the modified zero-gap electrolyzer at a given pressure. (a) Polarization curves. (b) Volume fractions of CO in the product gas. (c) Faradaic efficiencies of CO and H_2. (d) Calculated energy efficiency.

These compelling results imply that the direct introduction of pressurized CO_2 gas into the cathode effectively increases the local reactant concentration, thereby occupying a larger number of active sites and facilitating CO desorption. Experimental data confirm that the structured implementation of zero-gap electrolyzers, together with a carefully engineered microenvironment, can significantly enhance CO_2RR performance. Furthermore, elevating both operating temperature and pressure markedly accelerates

reaction kinetics and mass transport, contributing to improved energy efficiency in both alkaline and neutral electrolyte systems.

3.7 Conclusion

To address the challenges related to the scalability and economic feasibility of the CO_2 electroreduction reaction, this study proposes a pathway to enhance energy efficiency and extend operational durability. It is demonstrated that practical requirements for low cell voltage and high current density can potentially be met by tuning reactor temperature and pressure, which consequently elevate local gas concentration and accelerate the reaction rate. At an operating temperature of 50 °C, the energy efficiency reaches 48% at a current density of 100 mA/cm^2 and maintains 40% at 200 mA/cm^2 within alkaline electrolytes. When operated under a pressure of 3 bar, the energy efficiency sustains 47% at 100 mA/cm^2 and 35.5% at 200 mA/cm^2. Additionally, water vapor present in humidified CO_2 acts as a medium facilitating the dissolution of minor carbonate precipitates on the cathode surface. This synergistic effect is confirmed by stable system operation exceeding 100 hours with an FE_{CO} above 90% at 100 mA/cm^2 in a neutral anolyte environment. Modest adjustments to temperature or pressure result in an improvement of over 10% in the energy conversion efficiency of the MEA electrolyzer compared to conditions at room temperature and atmospheric pressure. The findings detailed in Chapter 3 have been published in Chemical Engineering Journal (2025) under the title “Robust and efficient electroreduction of CO_2 to CO in a modified zero-gap electrochemical cell.”

4 Cu-based Catalyst Effect

4.1 Insights of CO_2-to-C_{2+} with anion exchange membrane

Currently, the industrial production of carbon-based fuels predominantly depends on thermochemical processes that require high temperatures and pressures [40]. In contrast, the electrochemical reduction of CO_2 offers a promising route to decarbonized fuel synthesis, through the formation of carbon–carbon (C–C) bonds that enable the direct generation of high hydrocarbons (C_{2+}) [82, 147, 148]. These C_{2+} products are of particular significance due to their high energy densities and substantial economic value, making them attractive targets for large-scale energy storage and chemical manufacturing applications [53]. Electrochemical pathways, especially those powered by renewable electricity, represent a sustainable and potentially decentralized alternative to conventional energy-intensive processes, and have thus emerged as a focal point in the pursuit of carbon-neutral fuel technologies [64, 72, 80]. Nevertheless, achieving high selectivity toward C_{2+} species by CO_2RR remains a fundamental challenge, particularly in comparison to the relatively simpler formation of single-carbon (C_1) products [57]. This is primarily due to the inherent mechanistic complexity of C–C coupling reactions, which encompass multiple PCET steps, the generation and stabilization of key reaction intermediates, surface activation and binding phenomena on electrocatalysts, as well as the desorption dynamics of the resulting products [149-151].

Copper-based materials are recognized as among the most effective catalysts for producing higher hydrocarbons (C_{2+}) due to their distinctive ability to stabilize the reaction intermediate *CO during CO_2 reduction [61, 63, 153]. The most likely C_2 and C_3 pathways starting from *CO on Cu surfaces are shown in Figure 4.1 [152]. However, the distribution of products and the reaction efficiency are not solely dictated by catalyst properties but are also influenced by numerous operational factors within the electrolyzer. Variables such as electrolyte composition, electrode potential, temperature, and pressure play crucial roles in steering reaction pathways and energy conversion to favor specific products [81, 84, 93, 154, 155]. Furthermore, the design and operating conditions of the

electrolyzer, encompassing features like gas diffusion electrode design and fluid flow dynamics, significantly affect mass transport which in turn may influence both activity and selectivity [156-158]. A thorough understanding of the interplay between these parameters is vital for achieving optimal CO_2RR performance.

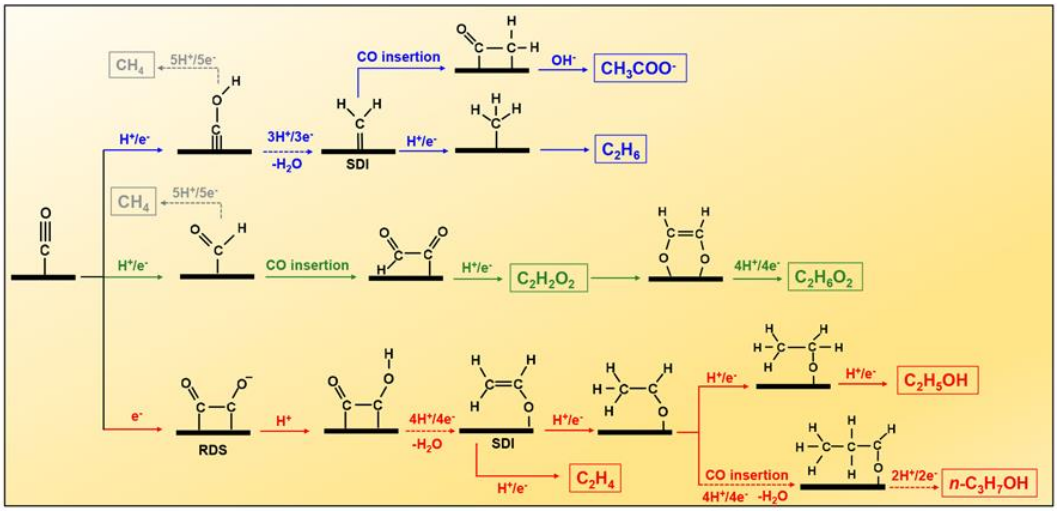

Figure 4.1: Most likely C_2 and C_3 pathways starting from *CO on Cu surfaces [152].

In CO_2RR, the AEM membrane can conduct anions (such as OH^- or HCO_3^-) rather than cations (such as H^+), which allows the reaction system to maintain an alkaline environment. This alkaline environment is conducive to the generation of C_2 products because it can reduce competition with H^+ and avoid the generation of H_2 gas, thereby improving the Faradaic efficiency and selectivity of CO_2 reduction. Conducting CO_2RR experiments under elevated temperature and pressure offers additional advantages, such as accelerating reaction kinetics, enhancing mass transport, and improving product selectivity [140, 159]. However, these conditions bring about technical challenges, such as the need for robust sealing and reliable safety measures for high-pressure environments, as well as ensuring the stability of catalysts and electrolytes under extreme conditions [160].

These challenges can be addressed by optimizing the electrocatalytic process and systematically evaluating the impact of various operating parameters. This means fine-tuning factors such as temperature, pressure, electrolyte properties, and catalyst architecture should be taken into consideration for a universal CO_2RR system. By

analyzing the combined effects of these variables on product distribution, current efficiency, and energy consumption in this modified electrolysis reactor and system, this work aims to provide valuable insights into the development of efficient, stable, and scalable CO_2RR systems for future applications.

4.2 Characterization of Cu electrodes

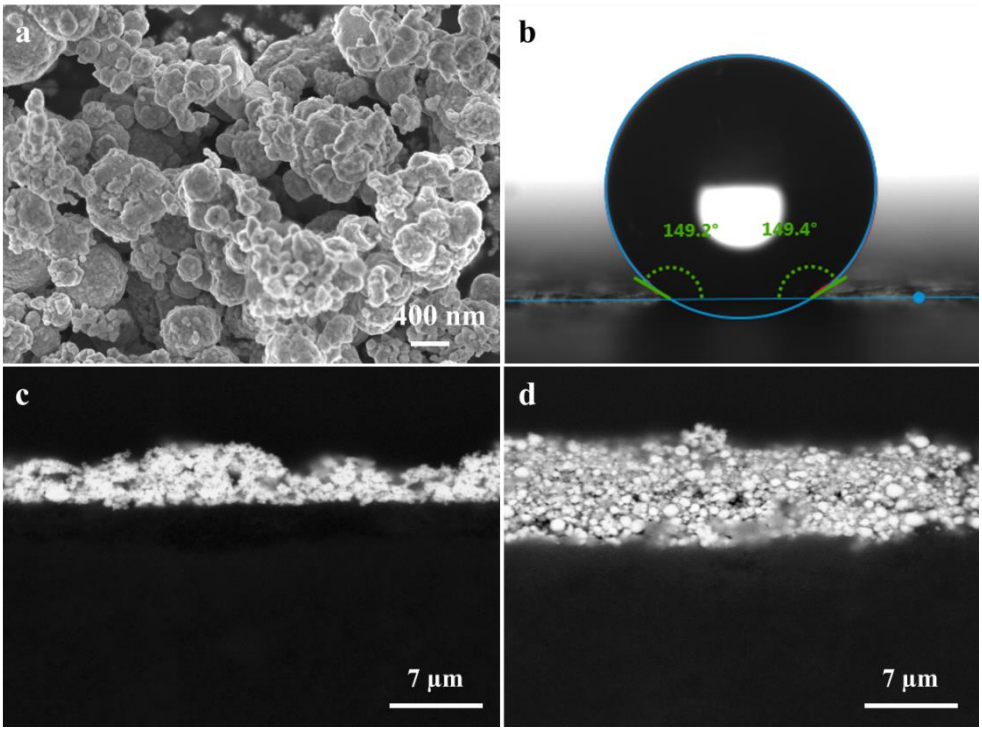

Figure 4.2: Characterization of cathodes. (a) SEM of commercial Cu powders. (b) Water contact angle of the prepared Cu@C electrode. SEM image from a cross-section of the prepared (c) Cu@C electrode and (d) CuAg@C electrode.

A conventional copper cathode is fabricated by manually spraying the catalyst ink, as detailed in Chapter 2.4.2, resulting in a cathode catalyst layer with a mass loading near 1.5 mg/cm^2. Furthermore, an equivalent mass of silver nanocatalyst is spray-deposited onto a copper-coated electrode to yield a CuAg@C cathode, or alternatively, copper is deposited onto a pre-existing silver-coated electrode to form an AgCu@C cathode. The overall catalyst loading for both tandem catalyst layer arrangements range from approximately 2.8 to 3.0 mg/cm^2. An SEM image of the commercial copper catalyst employed is shown in Figure 4.2a, which reveals distinct nanoparticles despite some

unavoidable agglomeration. The resulting Cu@C electrode displays superhydrophobic behavior with a contact angle exceeding 149°, as depicted in Figure 4.2b, which is anticipated to enhance gas transport at the three-phase interface during catalytic reactions [74]. The cross-sectional SEM image in Figure 4.2c illustrates a uniform copper catalyst layer approximately 5 µm thick on the carbon GDL. Moreover, Figure 4.2d presents a cross-sectional view of the CuAg electrode after the deposition of the dual catalyst layers, demonstrating a continuous, crack-free coating without discernible interfaces. The total thickness of the catalyst layers is around 8 µm, indicating a consistent deposition over the electrode surface. These morphological and structural characterizations confirm the effective fabrication and integration of the catalyst layers.

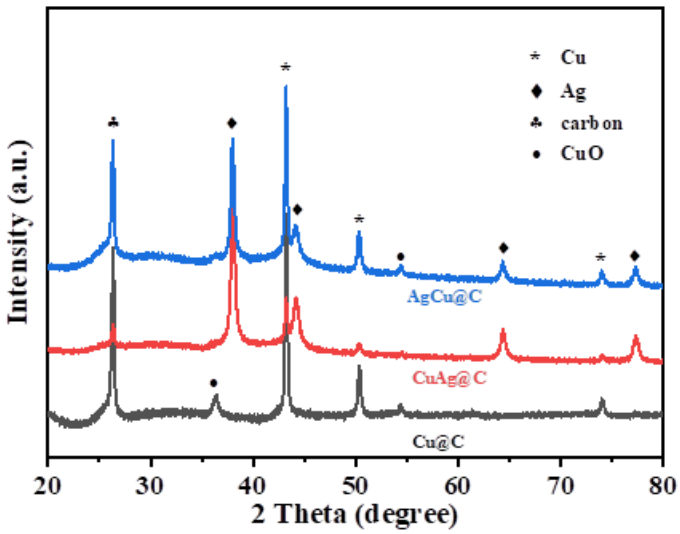

Figure 4.3: XRD patterns of Cu, CuAg, and AgCu electrodes.

XRD analysis was performed to determine the crystal structure and phase purity of the catalyst, with the resulting spectrum presented in Figure 4.3. The characteristic diffraction peaks at 43.1°, 50.4°, and 74.2° are assigned to the (111), (200), and (220) planes of copper, respectively, according to JCPDS No. 04-0836 [161]. Moreover, two minor peaks corresponding to CuO, identified by JCPDS No. 48-1548 [162], suggest partial oxidation of the copper. Diffraction peaks attributable to the (111), (200), (220), and (311) planes of silver, as indexed by JCPDS No. 65-2871 [163], appear in both varieties of tandem electrodes.

4.3 Effect of temperature on the alkaline system

In practical applications, electrolyzers operate under diverse external conditions, yet temperature is frequently neglected as a key factor when assessing CO_2RR systems [164]. Accordingly, this study systematically examines the product distribution and energy conversion efficiency of copper catalysts in a zero-gap electrolyzer using 1 M KOH anolyte, across a temperature range from ambient to 80 °C. At ambient temperature, the cell delivers a total current of 1.2 A (current density of 100 mA/cm^2) at a cell voltage of 2.62 V, whereas increasing the current to 2.4 A (current density of 200 mA/cm^2) requires a voltage of 3.04 V, as depicted in Figure 4.4a.

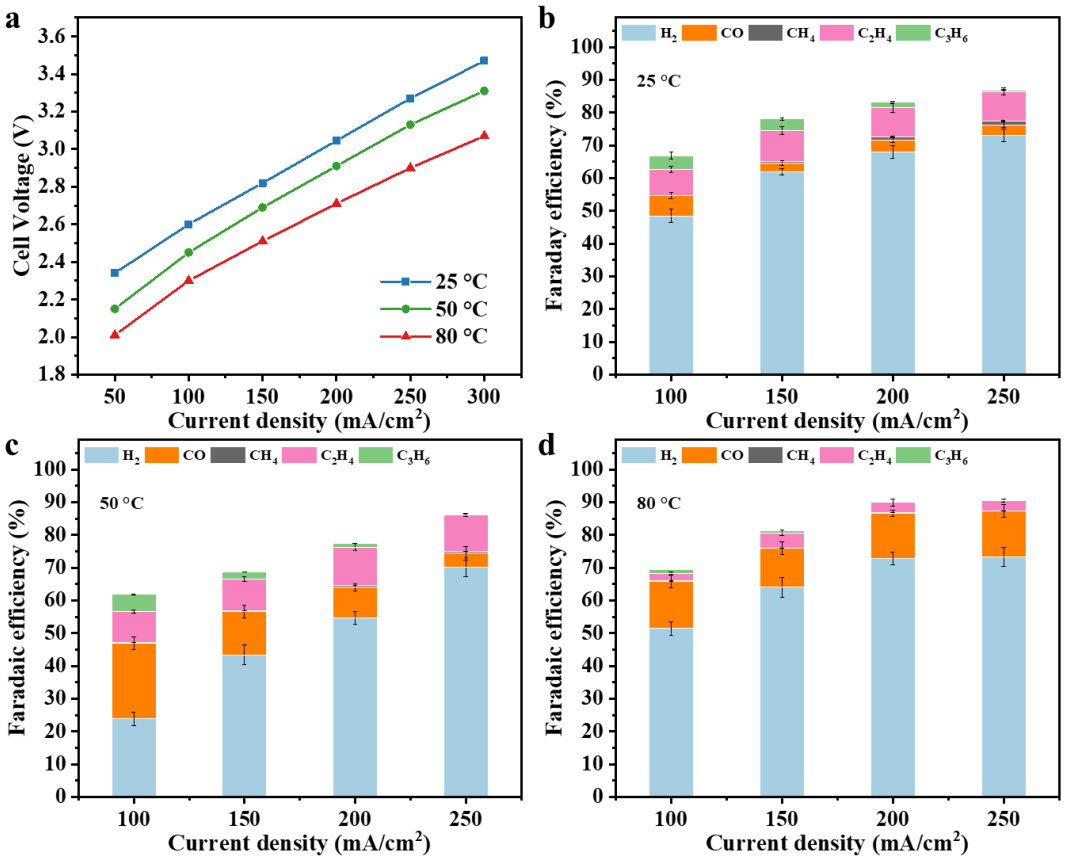

Figure 4.4: Electrocatalytic CO_2RR performance in 1 M KOH anolyte. (a) Polarization curves at several operating temperatures. Faradaic efficiencies of the products at reaction temperatures of (b) 25 °C, (c) 50 °C, and (d) 80 °C.

It should be noted that Cu-based catalysts have been reported to generate liquid products, such as formic acid (Appendix A2). Due to the lack of quantitative liquid-phase analysis in the current experimental setup, only the Faradaic efficiencies of gaseous products are presented. Under a current density of 100 mA/cm^2, the Faradaic efficiencies for CO, C_2H_4, and C_3 products are 6.25%, 7.82%, and 4.28%, respectively. Upon increasing the current density to 200 mA/cm^2, FE_{CO} decreases to 3.58%, FE for C_2H_4 exhibits a slight rise to 8.79%, while the FE for C_3 products markedly declines to 1.81% (Figure 4.4b). These results demonstrate that, at room temperature, the alkaline electrolyzer system maintains moderate selectivity toward ethylene at elevated current densities. Concurrently, the generation of C_3 compounds is limited, likely due to competitive HER and other C_2 product formation pathways.

Increasing the reaction temperature to 50 °C significantly decreases energy consumption, as a current density of 100 mA/cm^2 is reached at 2.45 V, and 200 mA/cm^2 is attained at 2.91 V. As shown in Figure 4.4c, the FE_{CO} at 100 mA/cm^2 markedly increases to 23.14%, while the Faradaic efficiencies for C_2H_4 and C_3 products are 9.50% and 5.29%, respectively. At 200 mA/cm^2, CO selectivity declines to 9.31%, whereas C_2H_4 production rises to 11.82%, and the fraction of C_3 products decreases to 1.10%. The elevated temperature presumably enhances the kinetics of CO desorption and overall reaction rates, resulting in increased CO generation at intermediate current densities. Moreover, the acceleration of carbon-carbon coupling kinetics contributes to the augmented formation of C_2 products, albeit accompanied by a reduction in C_3 selectivity at higher current densities. Upon further increasing the temperature to 80 °C, the system achieves additional voltage reduction, reaching 100 mA/cm^2 at 2.3 V and 200 mA/cm^2 at 2.71 V. Nevertheless, the distribution of products exhibits substantial variation at this temperature. According to Figure 4.4d, CO demonstrates an FE of 14.46% at 100 mA/cm^2, while FEs for C_2H_4 and C_3 products decline to 2.33% and 1.10%, respectively. At 200 mA/cm^2, CO maintains a high FE of 13.90%, but C_2H_4 formation is limited to 3.10%. These observations imply that elevated temperatures favor CO production but destabilize intermediates essential for synthesizing C_2 and C_3 products. In addition, enhanced HER activity at higher temperatures likely suppresses the generation of higher hydrocarbons by increasing proton availability.

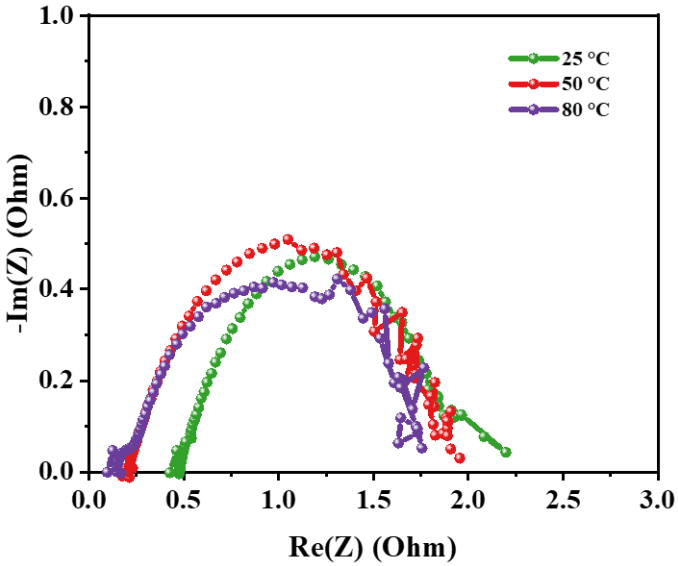

Figure 4.5: The Nyquist plots of the CO_2RR electrolyzer at several reaction temperatures.

The Nyquist plots presented in Figure 4.5 demonstrate clearly that raising temperature enhances ionic conductivity, reduces cell impedance, and consequently improves power conversion efficiency. Within the low-frequency region of the Nyquist plot, the impedance response deviates from an ideal semicircular shape and shows minor oscillations. This phenomenon results from the complex interactions among CO_2 mass transport, intermediate species accumulation, and local pH fluctuations inside the cathode catalyst layer, which are especially pronounced in MEA systems operating without catholyte [165, 166]. The synthesis of C_{2+} products further intensifies this effect due to the involvement of multiple proton-coupled electron transfer steps and various surface-bound intermediates.

The energy efficiency of CO_2RR is governed by reaction selectivity and overpotential, as calculated and presented in Figure 4.6. At a reaction temperature of 50 °C, the energy efficiency at a current density of 100 mA/cm^2 surpasses 20%, primarily due to the enhanced Faradaic efficiency of gaseous products and the lower electrolyzer voltage relative to room temperature. When the reaction temperature increases to 80 °C, the energy efficiency does not exhibit a further increase despite a continued decrease in electrolyzer voltage. This is mainly caused by the diminished Faradaic efficiency of the target products, resulting in an energy efficiency only 2%–5% greater than that observed

at ambient temperature. Although raising the reaction temperature reduces overpotential, this advantage can be counterbalanced by a decline in selectivity for the desired products, attributable to intensified side reactions.

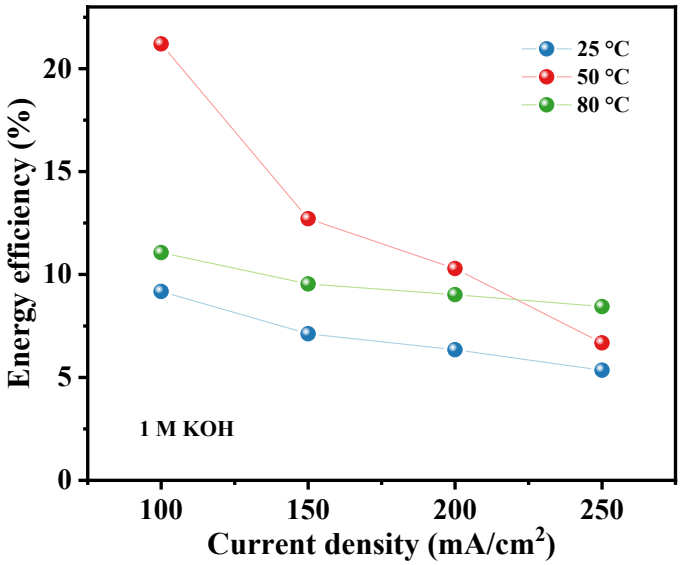

Figure 4.6: Calculated energy efficiency of detected C_1-C_3 gas products at each current density under operating temperatures of 25 °C, 50 °C, and 80 °C.

The stability of the CO_2RR process is assessed over a 3-hour period at a working current density of 100 mA/cm^2 and a reaction temperature of 50 °C (Figure 4.7a). The corresponding GC spectrum for gas composition analysis is shown in Figure 4.7b. The liquid products were not collected and quantitatively analyzed here, thus lacking the Faradaic efficiency of the liquid products. The overall Faradaic efficiency for gas-phase products remains relatively constant between 50% and 60%, although minor fluctuations appear in the selectivity of individual products. Such variations likely stem from transient changes in local pH and CO_2 coverage near the electrode surface [167]. Despite these fluctuations, the system maintains robust stability with consistently high overall Faradaic efficiency for gaseous products.

Temperature changes have a significant impact on the balance between energy efficiency and product selectivity in CO_2RR, as they directly influence the thermodynamic equilibrium potential and ionic conductivity. Moderate temperatures around 50 °C provide an optimal compromise by lowering energy requirements and

increasing the yields of CO and C_2H_4. However, at elevated temperatures, although energy efficiency improves further, the selectivity toward more complex products such as C_2H_4 and C_3 declines. These results emphasize the importance of carefully tuning operational conditions to attain specific product distributions. Additionally, continuous monitoring of overall efficiency and product composition during prolonged operation at fixed current density is essential to understand the relationship between reaction environment and catalyst behavior, thereby facilitating the design of stable and efficient CO_2RR systems.

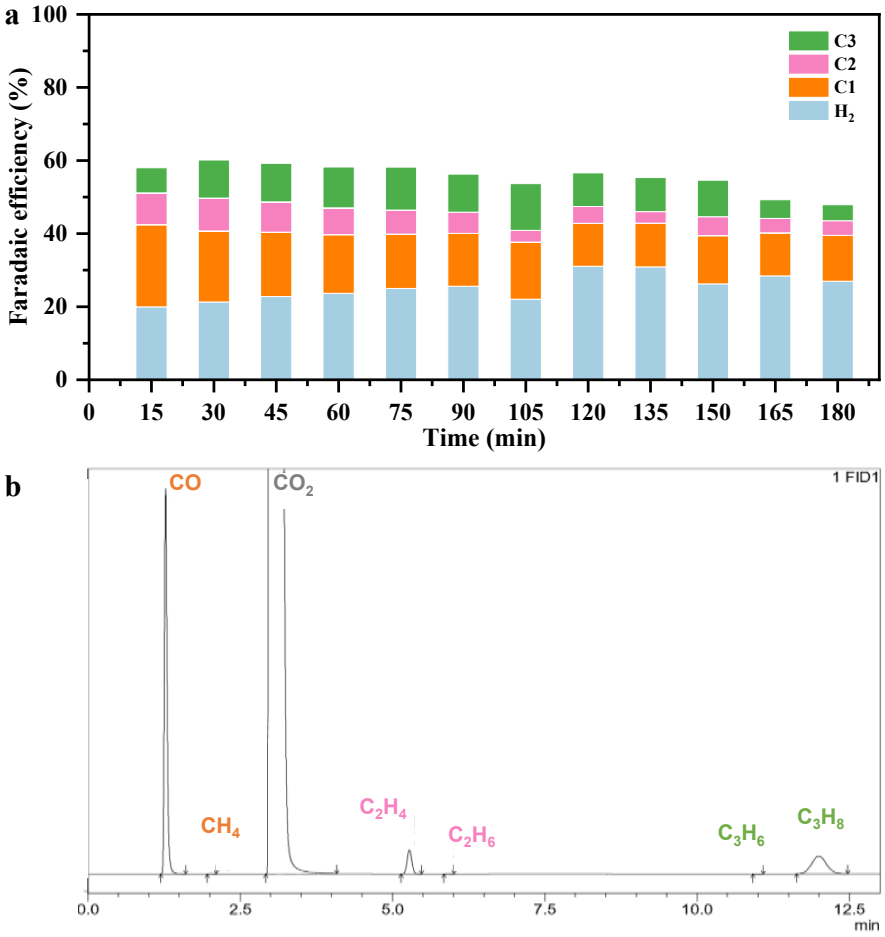

Figure 4.7: (a) Stability of the electrolytic reaction at a current level of 1.2 A at 50 °C in 1 M KOH anolyte. (b) GC spectrum for gas content and concentration analysis.

4.4 Effect of high pressure on the alkaline system

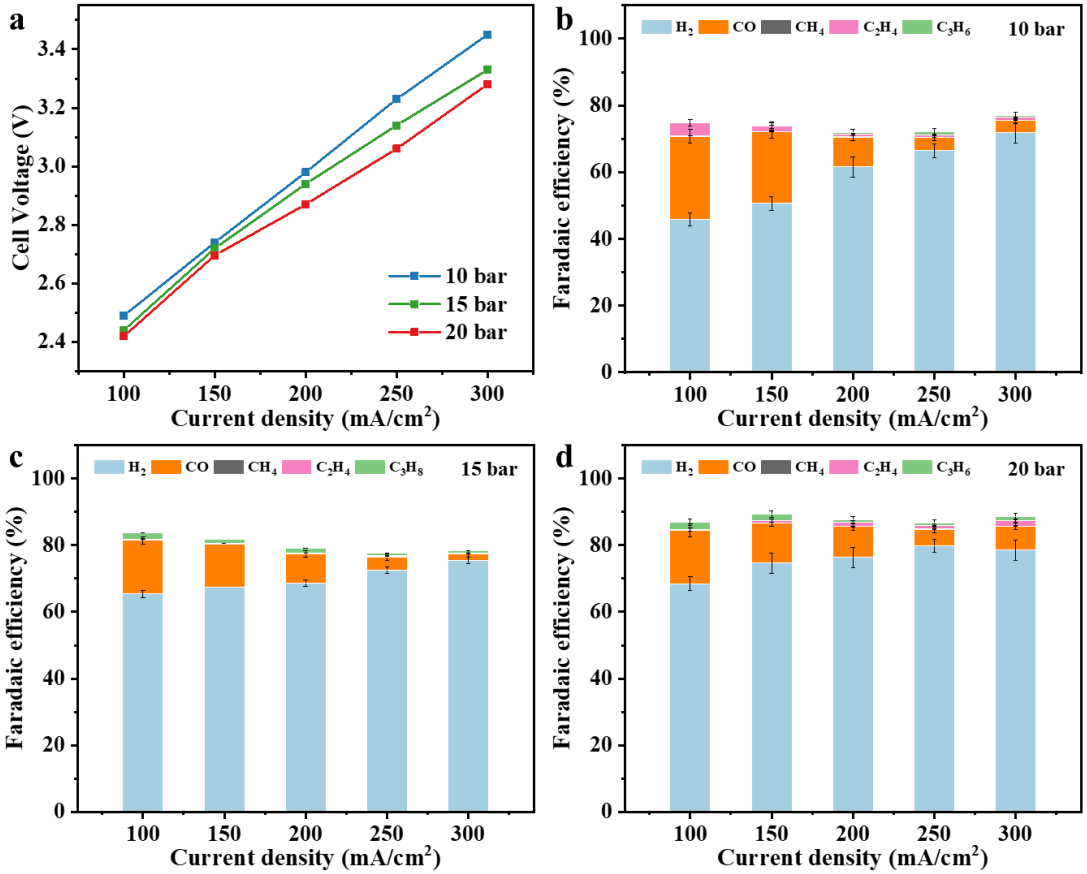

Figure 4.8: Electrocatalytic performance under high pressure conditions at 25°C in 1 M KOH anolyte. (a) Polarization curves. Faradaic efficiencies of the products at a reaction pressure of (b) 10 bar, (c) 15 bar, and (d) 20 bar.

Enhancing the CO_2 gas flow pressure is believed to improve the local concentration of CO_2 at the catalyst interface [139, 168, 169]. However, this also introduces stricter demands on catalyst durability and reactor configuration [87, 160, 170]. The effect of elevated pressures above 10 bar on CO_2RR performance in 1 M KOH electrolyte is systematically investigated using a modified electrolyzer setup. At a current density of 100 mA/cm^2, the cell voltage measures 2.49 V under 10 bar, decreases to 2.44 V at 15 bar, and further declines to 2.42 V at 20 bar. When the current density increases to 200 mA/cm^2, the corresponding cell voltages are 2.98 V, 2.94 V, and 2.87 V for 10, 15, and 20 bar, respectively. A similar pattern is observed at 300 mA/cm^2, where voltages of 3.45 V, 3.33 V, and 3.28 V are recorded as the pressure increases (Figure 4.8a). The moderate

reduction in activation energy barriers with pressure elevation, as illustrated in the Pourbaix diagram derived from the Nernst equation (Figure 4.9) [140], aligns with the minor voltage drops observed in the polarization curves. These results suggest that operating under high-pressure conditions is thermodynamically favorable for CO_2RR.

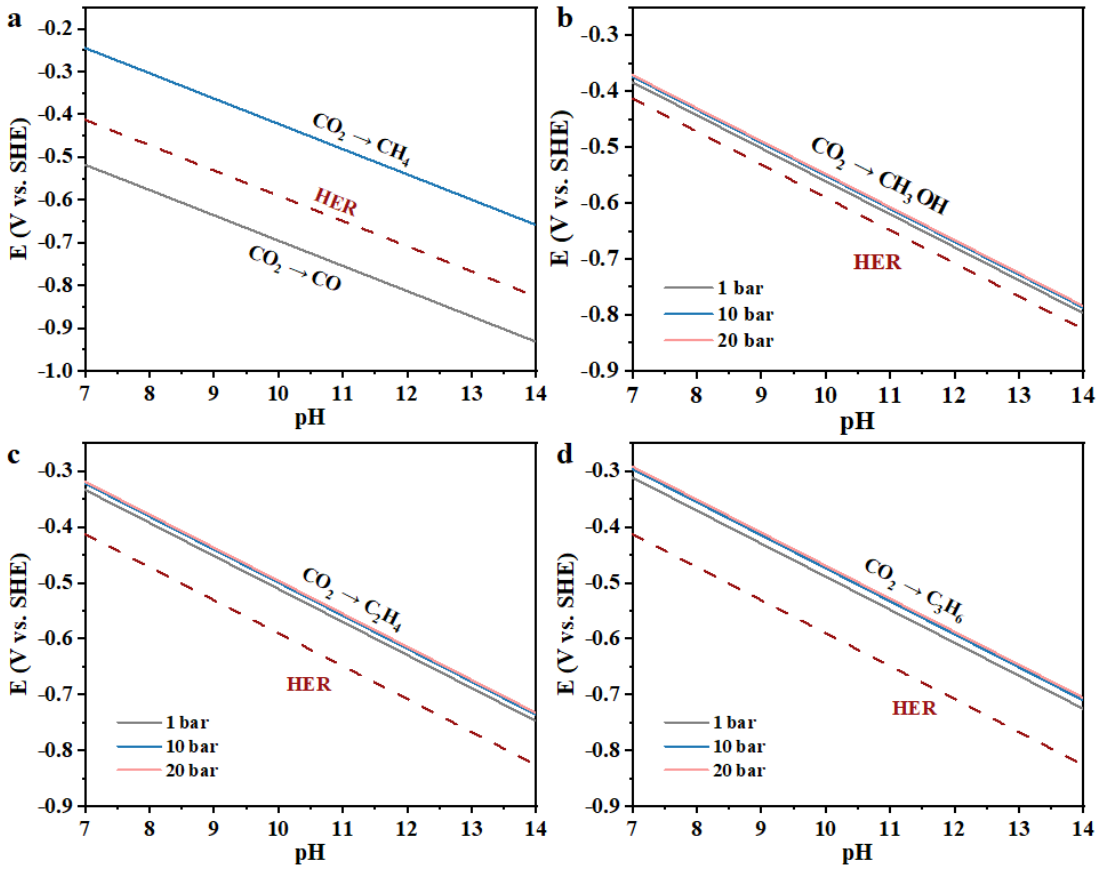

Figure 4.9: Effect of pressure on Pourbaix diagram for the electroreduction of CO_2 to C_1-C_3 products.

The Faradaic efficiencies of various products demonstrate pronounced variations in selectivity between hydrogen and carbon-based species under different pressure conditions. At 10 bar, FE_{CO} attains 24.92% at 100 mA/cm^2, but drops to 8.98% at 200 mA/cm^2 and further declines to 3.83% at 300 mA/cm^2. Ethylene exhibits an FE of 4.02% at 100 mA/cm^2, yet becomes nearly undetectable as the current density increases, with values falling to 0.86% at 200 mA/cm^2 and 0.78% at 300 mA/cm^2 (Figure 4.8b). Conversely, hydrogen evolution shows a distinct upward trend, reaching FEs of 45.87%, 61.56%, and 71.79% at 100, 200, and 300 mA/cm^2, respectively. At 15 bar, the product

distribution undergoes a notable shift (Figure 4.8c). The FE_{CO} at 100 mA/cm^2 reduces to 16.08%, while ethylene formation becomes negligible. Simultaneously, the FE of C_3 products increases slightly to 1.88%. As the current density rises, FE_{CO} continues to decline, registering 8.73% at 200 mA/cm^2 and 1.87% at 300 mA/cm^2. Ethylene remains barely detectable across all tested current densities, while C_3 products display marginal enhancements at both 100 and 300 mA/cm^2. Hydrogen production remains dominant, achieving an FE of 75.55% at 300 mA/cm^2, highlighting the increasing competitiveness of the HER against CO_2 reduction pathways. A comparable pattern emerges under 20 bar conditions (Figure 4.8d). At 100 mA/cm^2, FE_{CO} remains at 16.08%, while ethylene formation slightly increases to 0.26%, and C_3 product FE reaches 2.13%. At 200 mA/cm^2, FE_{CO} drops to 9.25%, accompanied by ethylene and C_3 FEs of 1.20% and 0.82%, respectively. At 300 mA/cm^2, FE_{CO} declines further to 7.18%, while ethylene and C_3 products show modest increases to 1.74% and 1.13%, respectively. Hydrogen generation peaks at this stage, with an FE of 78.53%, reaffirming the prevailing dominance of HER under high-pressure regimes.

The multi-proton coupled electron transfer processes intrinsic to CO_2RR involve intricate reaction kinetics. The generation of C_2 and C_3 species typically proceeds via multi-step mechanisms, requiring stabilization of key intermediates [56], which may not be adequately facilitated under pressurized conditions. Elevated pressure can increase CO_2 surface coverage on the catalyst, potentially blocking active sites or altering the reaction pathway, for instance, favoring CO desorption rather than its retention and transformation into C–C bonded products. Moreover, water transport from the cathode to the anode, driven by electric field and concentration gradients [171, 172], may further intensify HER, particularly at high current densities. These combined effects contribute to the unexpected suppression of C_2 and C_3 product formation under high-pressure environments. The data from high-pressure electrolysis indicate a consistent trend toward enhanced hydrogen generation, accompanied by a diminished selectivity for CO and multi-carbon products. This observation highlights the feasibility of leveraging pressurized systems for syngas production, a CO and H_2 mixture well-suited for downstream catalytic applications, such as Fischer–Tropsch synthesis, which typically demands a H_2:CO molar ratio of approximately 2:1 [173]. Consequently, the tunability

of product distribution under elevated pressures presents a promising strategy for coupling CO_2RR with thermocatalytic upgrading routes, enabling the efficient synthesis of energy-dense hydrocarbon fuels.

4.5 Effect of neutral anolyte

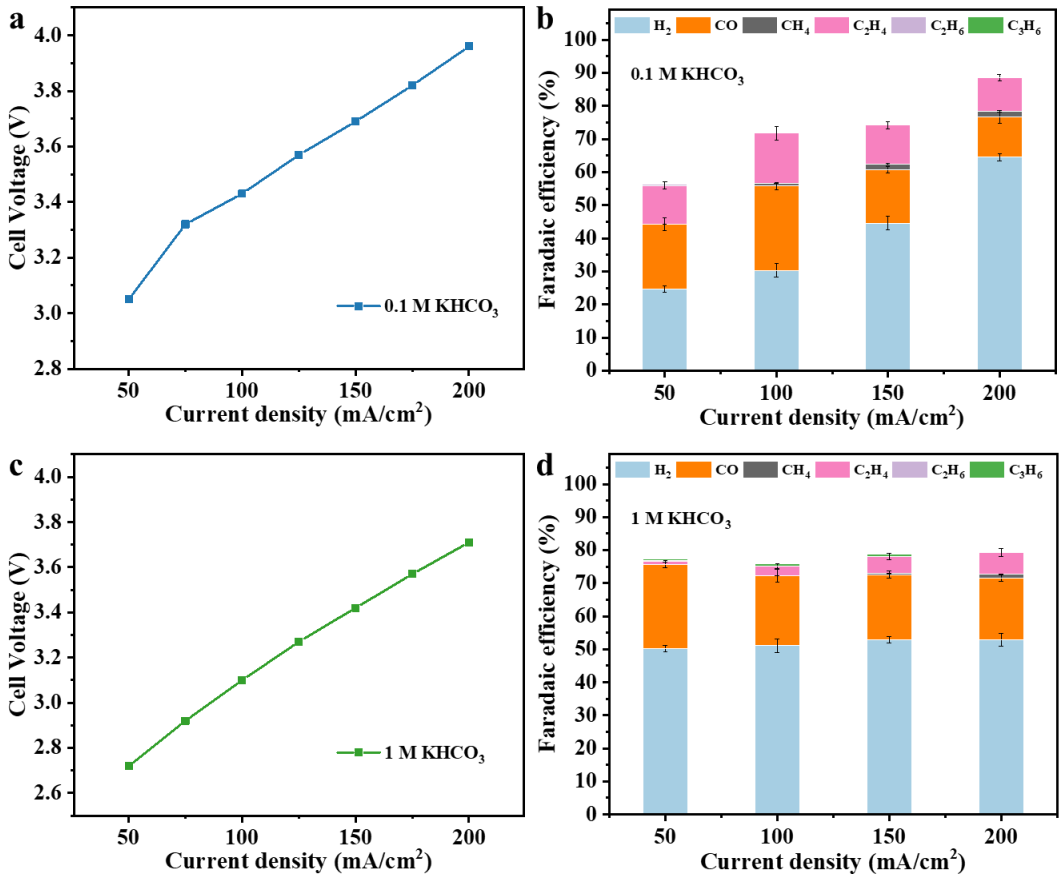

Figure 4.10: (a) Polarization curves and (b) Faradaic efficiencies of the products in 0.1 M $KHCO_3$ anolyte. (c) Polarization curves and (d) Faradaic efficiencies of the products in 1 M $KHCO_3$ anolyte.

Neutral $KHCO_3$ solutions, valued for their eco-friendliness, non-toxicity, and widespread availability, have become a commonly used electrolyte in CO_2RR systems due to their ability to buffer pH and donate protons [99, 174]. Investigating the effect of $KHCO_3$ concentration in the anolyte under zero-gap electrolyzer configurations offers crucial insights into the fundamental reaction mechanisms involved. As demonstrated in Figures 4.10a and 4.10b, when employing a 0.1 M $KHCO_3$ anolyte, the cell voltage

stabilizes around 3.43 V at a current density of 100 mA/cm^2 (equivalent to a total current of 1.2 A). Under these conditions, gaseous products dominate the product distribution, with ethylene and CO achieving Faradaic efficiencies of 15.1% and 25.4%, respectively. Upon increasing the current density to 200 mA/cm^2 (2.4 A), the cell voltage increases to 3.96 V, while the FEs for ethylene and CO decrease to 10.1% and 12.1%, respectively. The formation of ethylene is likely promoted through enhanced CO dimerization pathways. These results are consistent with the work of Peter Strasser et al., who found that a sharp rise in local pH during electrolysis with dilute bicarbonate solutions encourages C–C coupling, thereby favoring C_2 product formation [175]. Nonetheless, the higher cell voltage highlights the limited buffering and ionic conductivity capabilities of low-concentration electrolytes. The reduced selectivity toward carbon-based products under elevated potentials stems from increased competition between proton-coupled electron transfer steps, which tends to enhance HER activity at the expense of CO_2RR. As a result, the efficiency of C_{2+} hydrocarbon production diminishes in low-concentration $KHCO_3$ solutions under high current densities.

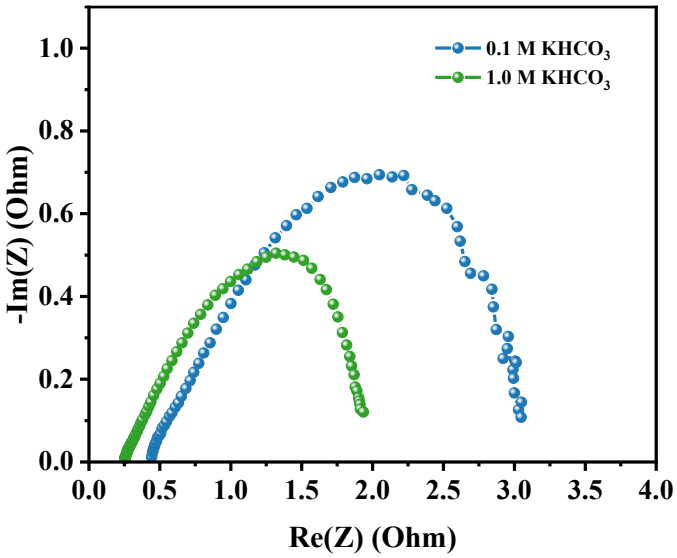

Figure 4.11: Nyquist plots of the neutral system with different concentration anolyte.

In contrast, raising the $KHCO_3$ concentration to 1.0 M leads to a marked reduction in cell voltage to 3.1 V at 100 mA/cm^2 and 3.71 V at 200 mA/cm^2 (Figure 4.10c). The improved buffering capacity and ionic conductivity reduce ohmic losses and help maintain a stable local pH, thus enabling a more energy-efficient operation, as

corroborated by the Nyquist plots in Figure 4.11. However, the FE_{CO} decreases to 21.2%, and hydrogen becomes the predominant product, reaching an FE of over 51% at 100 mA/cm^2, as illustrated in Figure 4.10d. At 200 mA/cm^2, HER dominates further, with hydrogen attaining an FE of 52.9%, and CO declining to 18.7%. These observations are consistent with findings by Kastlunger et al., who reported that higher bicarbonate concentrations tend to promote methane and oxygenated C_{2+} product formation, often at the cost of ethylene selectivity [176].

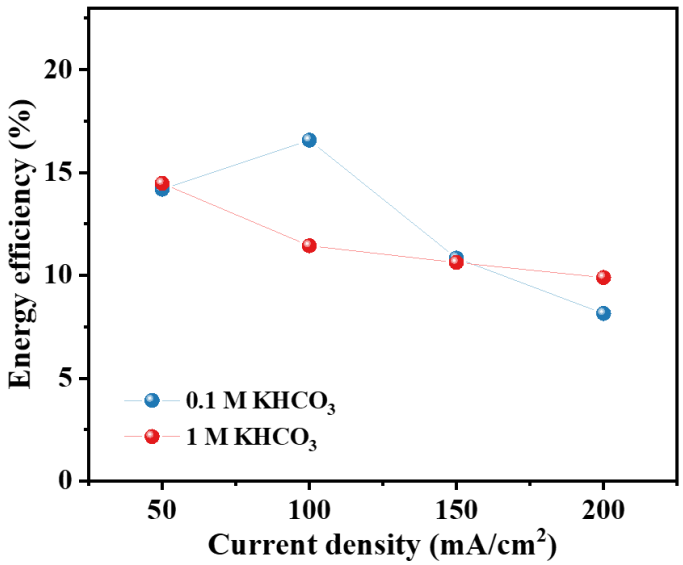

Figure 4.12: Calculated energy efficiency for C_1-C_3 gas products with 0.1 M and 0.1 M $KHCO_3$ anolyte.

Although the low-concentration neutral system operates at higher cell voltages, its improved selectivity toward C_1–C_3 products results in a higher energy efficiency (17%) at 100 mA/cm^2 compared to the system using a concentrated anodic electrolyte (Figure 4.12). The concentration of $KHCO_3$ plays a decisive role in modulating ethylene production, necessitating careful optimization to balance energy consumption, product selectivity, and long-term stability. While elevated electrolyte concentrations enhance conductivity and reduce voltage requirements, they tend to favor HER, thus constraining C_{2+} yields. Conversely, diluted solutions support higher ethylene selectivity, albeit at the expense of greater energy input. Hence, the correlation between electrolyte concentration and reaction kinetics proves crucial in steering product distribution in neutral CO_2RR systems.

4.6 Effect of tandem catalysts

Tandem catalyst layer electrodes combine silver, known for its high selectivity toward CO, with copper, which promotes the formation of C_{2+} products, thereby establishing a sequential reaction mechanism [177]. This dual-functional architecture spatially separates the CO_2 reduction reaction into two distinct steps: CO_2-to-CO and CO-to-C_2 conversions at different catalytic interfaces, which enhances surface *CO accumulation and facilitates C–C bond formation [73]. In this context, an AgCu tandem catalyst is fabricated by sequentially depositing a silver catalyst layer onto the GDL, followed by a copper layer; the reverse configuration is referred to as CuAg. Elemental distribution analysis via EDS mapping confirms a homogeneous dispersion of metals and reveals a predominance of the uppermost deposited element, as depicted in Figure 4.13.

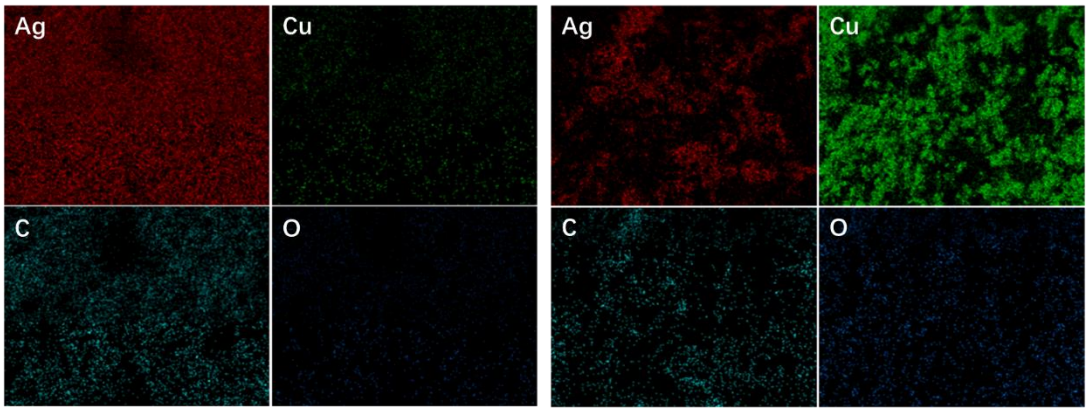

Figure 4.13: EDS mapping of CuAg@C (left) and AgCu@C (right) electrode.

Under alkaline conditions, the AgCu electrode maintains a low voltage requirement, reaching 2.7 V at a current density of 100 mA/cm^2 and 3.08 V at 200 mA/cm^2 (Figure 4.14a). At 100 mA/cm^2, FE_{CO} reaches 24.14%, while C_2H_4 and H_2 exhibit FEs of 2.07% and 55.08%, respectively. When the current density increases to 200 mA/cm^2, FE_{CO} decreases notably to 12.21%, accompanied by a slight rise in C_2H_4 FE to 2.26% and a more substantial increase in H_2 FE to 66.75% (Figure 4.14b). The CuAg electrode shows a marginally lower cell voltage of 2.6 V at 100 mA/cm^2 and a higher one of 3.14 V at 200 mA/cm^2. At 100 mA/cm^2, the FE_{CO} is lower at 20.63%, with no detectable formation of C_2H_4 (Figure 4.14c), while H_2 dominates the product profile with an FE of 71.15%. At

200 mA/cm^2, FE_{CO} drops to 13.07%, C_2H_4 emerges with an FE of 1.16%, and H_2 increases to 74.90%.

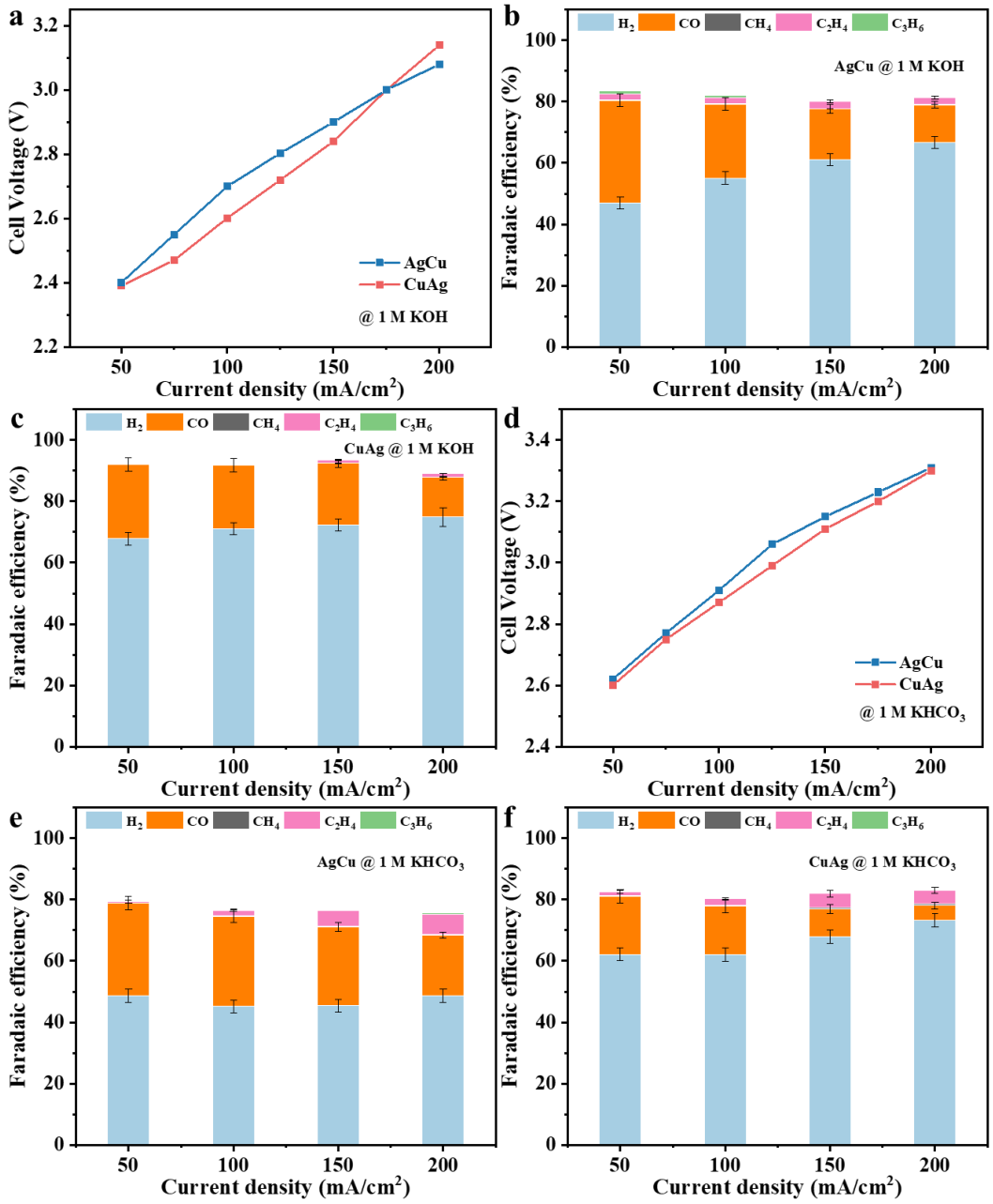

Figure 4.14: (a) Polarization curves of two types of Ag/Cu tandem catalysts in 1 M KOH anolyte. Faradaic efficiencies of the products from (b) AgCu and (c) CuAg catalysts in an alkaline system. (d) Polarization curves of the tandem electrodes in 1 M $KHCO_3$ anolyte. Faradaic efficiencies of the products from (e) AgCu and (f) CuAg electrodes in a neutral system.

In neutral electrolyte, the AgCu electrode operates at 2.91 V for 100 mA/cm^2 and 3.31 V for 200 mA/cm^2 (Figure 4.14d). At 100 mA/cm^2, it yields CO with an FE of 29.44%, alongside 1.81% for C_2H_4 and 45.15% for H_2. Increasing the current density to 200 mA/cm^2 results in a decrease in FE_{CO} to 19.71%, while C_2H_4 FE increases substantially to 6.50% (Figure 4.14e). For the CuAg configuration, cell voltages are 2.87 V and 3.3 V at 100 and 200 mA/cm^2, respectively. At 100 mA/cm^2, FE_{CO} is 15.80%, while C_2H_4 and H_2 achieve FEs of 2.20% and 62.14%, respectively. At 200 mA/cm^2, FE_{CO} drops significantly to 4.92%, while C_2H_4 and H_2 FEs rise to 4.33% and 73.20%, respectively, as presented in Figure 4.14f.

Although the tandem electrode arrangement enhances CO generation and improves overall Faradaic efficiency, the formation of carbon products (C_2–C_3) remains constrained relative to pure copper electrodes. Moreover, the comparative increase in C_2H_4 production in neutral versus alkaline media indicates that electrolyte composition has a substantial influence on the catalytic reaction pathways. These findings underscore the necessity of rational catalyst design to tailor product selectivity and highlight the synergistic role of catalyst structure and electrolyte environment in steering the CO_2 reduction reaction toward desired outcomes.

4.7 Conclusion

This investigation conducts a comprehensive analysis of the impacts exerted by critical operational parameters, namely electrolyte concentration, reaction temperature, system pressure, and catalyst architecture, on CO_2RR performance within a zero-gap electrolyzer configuration. The data indicate that electrolyte concentration exerts a pronounced influence on both current efficiency and product selectivity. Specifically, lower concentrations favor the generation of C_2 species, whereas higher concentrations contribute to a reduction in cell voltage and facilitate proton transport, albeit at the expense of heightened HER activity. Reaction temperature is observed to modulate kinetic behavior; moderate thermal conditions strike a balance between energy input and selectivity, while elevated temperatures, although lowering voltage requirements, inhibit the formation of higher hydrocarbons. Increased operational pressure leads to enhanced

local CO_2 availability, reduced cell voltage, and improved mass transport and reaction kinetics. However, this also escalates HER competition, thereby compromising the selectivity toward multi-carbon products. Additionally, the interplay between components in tandem catalyst systems enhances CO generation, which is likely attributable to disparities in intermediate adsorption energetics, underscoring the importance of meticulous catalyst engineering. Collectively, these findings contribute valuable mechanistic understanding and offer actionable guidance for optimizing the efficiency and selectivity of CO_2RR systems. The core results presented in Chapter 4 have been disseminated in the form of a peer-reviewed article [178], titled “Synergistic electroreduction of CO_2 to C_1–C_3 gas products in a pressure-tolerant MEA system,” published in the International Journal of Hydrogen Energy (2025).

5 Operational Adjustments

5.1 Insights of CO_2-to-CO with cation exchange membrane

In a CO_2RR electrolyzer, the cation exchange membranes selectively conduct cations (such as H^+) and prevent anions (such as OH^-, HCO_3^-, and CO_3^{2-}) from passing through, thereby maintaining charge balance on both sides of the electrolyzer [53]. Carbon dioxide molecules are adsorbed onto the surface of metal catalysts, where they undergo coordinated proton-electron transfer (CPET) to be reduced to a carboxyl intermediate (*COOH). After acquiring protons and electrons and separating water molecules, *CO desorbs from the catalyst surface, yielding CO as the product [54, 59, 179]. Besides, the operational parameters could pose an impact on the energy efficiency of the CO_2RR electrolyzer by directly influencing the balance between the cell voltage and product Faradaic efficiency.

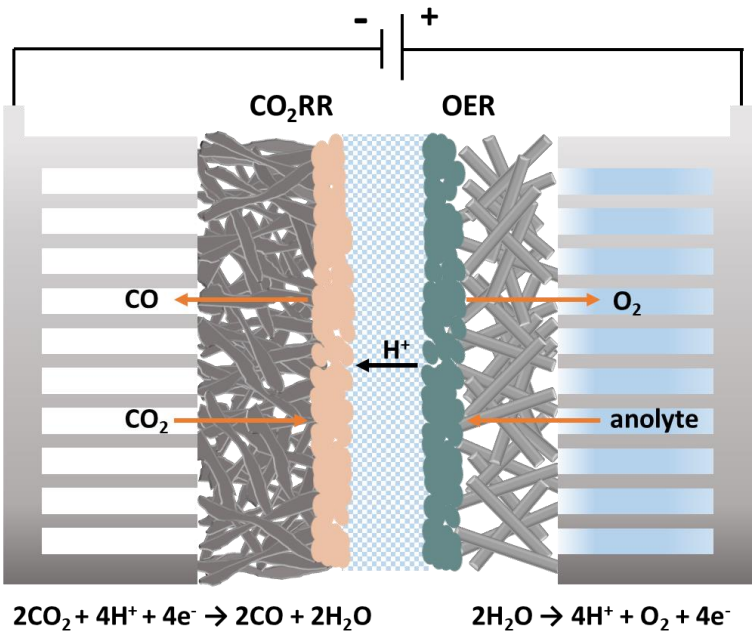

Figure 5.1: Schematic representation of a zero-gap CEM-MEA electrolyzer.

This chapter aims to investigate the influence of different parameters on the performance of a CEM-based MEA electrolyzer for the electrocatalytic conversion of

carbon dioxide to CO on the silver electrode. Figure 5.1 illustrates the schematic diagram of the studied CEM-MEA system. The system comprises two half-cells, namely an anode chamber and a cathode chamber, separated by a Nafion cation exchange membrane. Each chamber consists of fluid flow plates and gas diffusion electrodes, with each GDE composed of a gas diffusion layer and a catalyst layer. Both fluid flow plates are implemented in a spiral channel configuration to ensure a broad distribution of reactant species over the electrode region. At the anode, the anolyte undergoes electrolysis to produce gaseous oxygen and protons, a reaction known as the oxygen evolution reaction. Oxygen is discharged from the anode chamber along with the anolyte, while the protons are conducted to the cathode through the cation exchange membrane. At the cathode, humidified gaseous carbon dioxide is reduced to carbon monoxide in combination with protons and electrons on a silver catalyst layer.

5.2 Effect of cathode catalyst loading

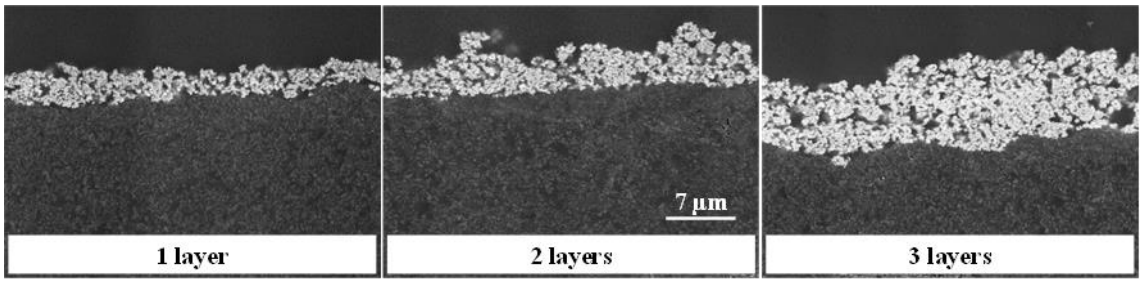

Figure 5.2: Cross-sectional SEM images of catalyst layers with different loading mass.

The preparation of the Ag cathode and IrO_2 anode is shown in Chapter 3. Here, the 12 cm^2 electrode with a total loading of 30 mg, 60 mg, and 90 mg of Ag nanoparticles by repeated spraying is defined as 1-, 2- and 3-layer electrodes respectively. Figure 5.2 shows the cross-sectional SEM images of 1-layer, 2-layer, and 3-layer Ag catalyst cathodes, respectively. Due to the rapid evaporation of the solvent, the dispersed ink mist is instantly fixed on the catalyst layer, thus forming a clear and thick catalyst layer. It can be inferred that the catalyst layer exhibits uniform features within the photographed area. The cathode catalyst layer (CCL) thickness of 1-layer Ag cathode sample is 3.2 µm, while that of 2- and 3-layer cathode sample is 6.3 µm and 9.5 µm, respectively.

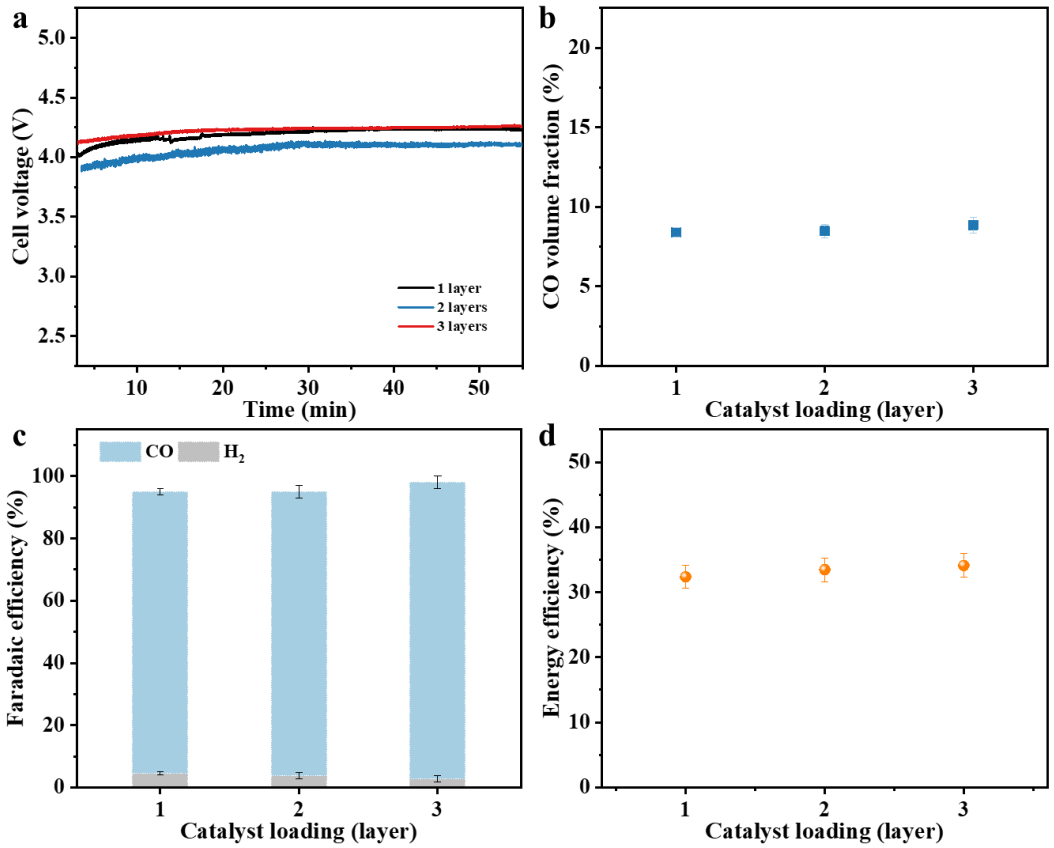

Figure 5.3: (a) Voltage response diagram of cathodes with different catalyst layer thicknesses at a constant current of 1.2 A, and (b) volume fraction of the generated CO product detected by GC. (c) Faradaic efficiency of carbon monoxide and (d) energy efficiency for CO production with different catalyst thicknesses in cathode electrode.

In this section the inlet volume flow rate of CO_2 was set to 90 standard cubic centimeters per minute (sccm), the reaction temperature to 25 °C, the reaction pressure to 0 barg, and 1 M $KHCO_3$ aqueous solution was selected as the anolyte. Figure 5.3a shows that the cell voltage remained close for all tested cathode catalyst loadings during the same period at a working current of 1.2 A. Among the three test samples, the 1-layer cathode and 3-layer catalyst performed equally well and required a cell voltage of 4–4.2 V to drive. The 2-layer catalyst sample performed best, with a cell voltage of 3.9–4.1 V. By automatically injecting the experimental product into the GC for three detections, the volume fraction of CO in real time is presented in Figure 5.3b. The volume fraction of

CO produced by the three different catalyst layers remains at a similar level, stabilizing at about 8–9%.

With increasing catalyst layer thickness, a slight improvement in the FE_{CO} is observed: from 90.5% for the single-layer electrode to 91.3% and 95.4% for the double- and triple-layer electrodes, respectively. Simultaneously, the hydrogen evolution contribution decreases from 4.4% to 2.7% (Figure 5.3c). Despite these variations, the energy efficiencies across all configurations remain within a narrow window of 32.3% to 33.8% (Figure 5.3d). Although enhanced CO selectivity is achieved with thicker catalyst layers, the absolute CO output, as reflected in partial current density or volumetric production rate, does not increase markedly. This outcome implies that, under constant-current operation, increasing catalyst layer thickness does not substantially enhance CO production, suggesting that the reaction kinetics are predominantly constrained by the imposed current rather than catalyst availability when employing a highly active Ag-based catalyst. While a marginal increase in FE_{CO} is noted with greater thickness, the corresponding gain in CO yield is limited, and excess catalyst material may remain unutilized. Thus, achieving a rational trade-off among catalyst usage, utilization efficiency, and transport phenomena is critical for optimizing CO_2 reduction systems. Considering practical aspects such as material cost and energy efficiency, the single-layer Ag electrode, offering sufficient catalytic activity and stable operation under these conditions, is chosen for subsequent investigations exploring other key parameters influencing CO_2RR performance.

5.3 Effect of CO_2 flow rate

This subsection systematically investigates the effect of CO_2 inlet flow rate on the performance of CO_2 electroreduction. All experiments were conducted at a reaction temperature of 25 °C and atmospheric pressure (0 barg), using 1 M $KHCO_3$ aqueous solution as the anolyte. As shown in Figure 5.4a, chronopotentiometric curves recorded at CO_2 flow rates ranging from 50 to 90 sccm show that the cell voltage increases with increasing flow rate. During the initial 15 minutes of electrolysis, an average voltage of 4.0 V is observed at 50–60 sccm, while the average voltage increases to 4.2 V at 70–

90 sccm. The slightly elevated voltage at higher flow rates may also indicate increased ohmic resistance or incomplete wetting of the GDE, potentially caused by faster gas removal from the reaction interface. As shown in Figure 5.4b, the volume fraction of CO in the gas product decreases as the CO_2 flow rate increases. This trend can arise from two distinct mechanisms: the dilution effect and kinetic limitations, which must be clearly distinguished to correctly interpret the data. The dilution effect refers to a physical process in which the concentration of a product gas (in this case, CO) decreases simply because it is mixed with a larger volume of unreacted CO_2. Under constant current operation, the amount of CO generated remains approximately the same, but the higher total gas flow reduces the measured CO concentration in the outlet stream. This is analogous to adding more water to a fixed amount of solute in a solution, the solute quantity stays the same, but the concentration decreases. By contrast, kinetic limitations occur when the reaction rate itself is affected. In the context of CO_2 electroreduction, such limitations may include insufficient CO_2 transport to the catalyst surface, incomplete wetting of the catalyst layer, or reduced availability of active sites due to mass transport resistance. These factors would lead to an actual reduction in CO production, not just dilution, resulting in both lower volume fraction and lower Faradaic efficiency.

To distinguish between these two effects, Figure 5.4c provides crucial supporting evidence. The Faradaic efficiency of CO remains above 90% across all tested flow rates, which suggests that the electrochemical conversion of CO_2 to CO remains efficient and consistent. This high and stable Faradaic efficiency indicates that the observed decrease in CO volume fraction is predominantly caused by the dilution effect, not by a loss of catalytic activity or transport failure. Furthermore, if kinetic limitations were dominant at higher flow rates, one would expect a drop in Faradaic efficiency due to insufficient CO_2 reaching the active sites or increased competition from side reactions such as hydrogen evolution. However, no such decrease is observed. On the contrary, the Faradaic efficiency slightly increases from 90.3% to 92.1% as the flow rate increases from 50 to 90 sccm, further reinforcing that catalytic performance remains intact. In summary, the combination of decreasing CO volume fraction (Figure 5.4b) and stable or slightly increasing Faradaic efficiency (Figure 5.4c) supports the conclusion that the CO concentration trend results primarily from a dilution effect, not from kinetic degradation

of the reaction. Additionally, the energy efficiency shown in Figure 5.4d remains stable within the range of 32.1% to 34.5%, reinforcing the conclusion that the system's overall performance is not significantly compromised at higher flow rates. The modest increase in cell voltage is likely related to interface effects (e.g., local drying or higher gas flow shear) but does not reflect a fundamental loss in catalytic or electrochemical function.

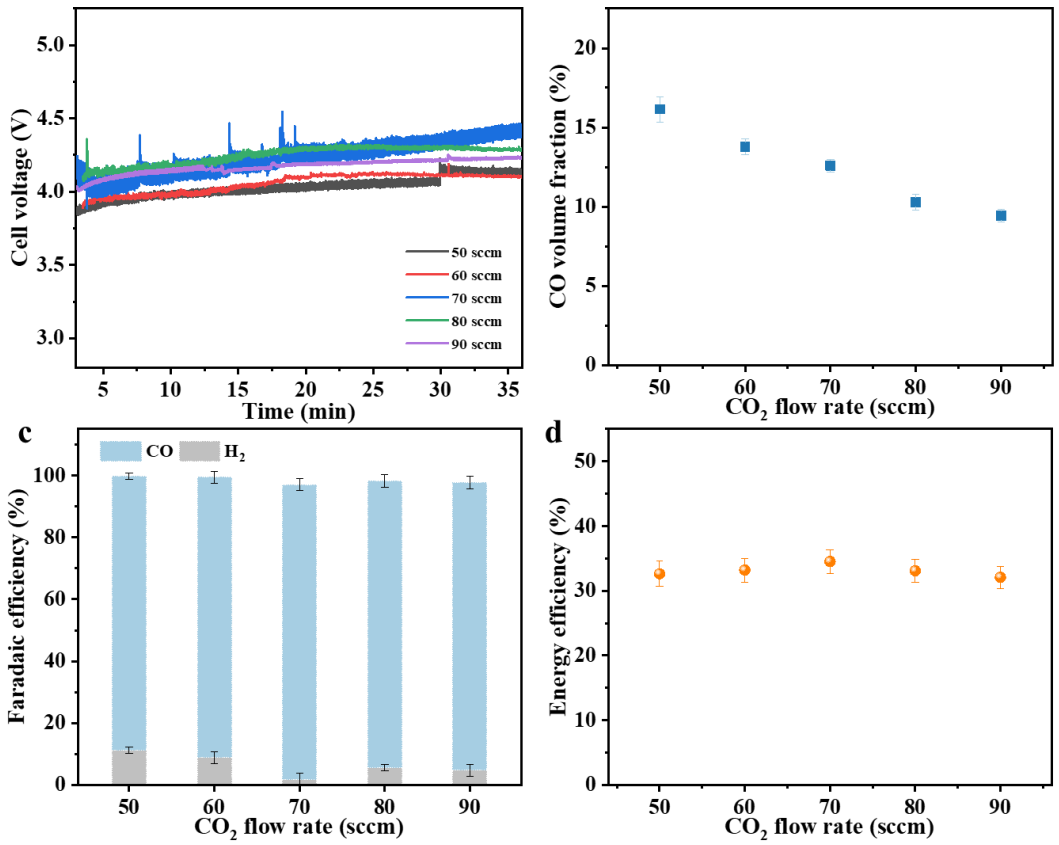

Figure 5.4: (a) Voltage response diagram and (b) volume fraction of the generated CO product detected by GC with different CO_2 inlet flow rates at a constant current of 1200 mA. (c) Faradaic efficiency of carbon monoxide and (d) energy efficiency for CO production with different CO_2 flow rates.

The results indicate that an optimal CO_2 flow rate is necessary to maintain a balance between CO concentration, Faradaic efficiency, and energy efficiency. At this flow rate, CO_2 supply matches the reaction rate at the catalyst surface and gas-liquid interfacial mass transport efficiency is strengthened, while side reactions are suppressed. This condition enables maximum CO production without excessive dilution or voltage penalties. The findings also emphasize the importance of controlling the CO_2 feed rate to

optimize, but careful consideration must be given to downstream product analysis and energy costs.

5.4 Effect of anolyte concentration

In a zero-gap electrolyzer, although the cathode is not in direct contact with a flowing liquid electrolyte, the anolyte can still migrate across the membrane to the cathode side due to electrostatic attraction and concentration gradients [172]. This ionic migration enables the anolyte to serve as the primary source of protons. The overall resistance of the cell is influenced by the electrolyte concentration [180], which, in turn, affects the voltage required to sustain a given current density. To investigate this relationship, potassium bicarbonate solutions with concentrations ranging from 0.1 M to 2 M were employed as the anolyte.

As illustrated in Figure 5.5a, a monotonic decline in cell voltage is observed with increasing $KHCO_3$ concentration, decreasing from values above 4.45 V at 0.1 M to around 3.7 V at 2.0 M. This reduction is primarily attributed to the improved ionic conductivity and diminished ohmic resistance associated with elevated electrolyte concentrations [86, 180]. The composition of the anolyte also exerts a pronounced influence on product distribution. According to Figure 5.5b, FE_{CO} significantly rises from 34.4% at 0.1 M to 93.0% at 1.0 M $KHCO_3$, whereas the Faradaic efficiency for H_2 falls sharply from 64.1% to below 5%. This trend can be ascribed to modifications in the local cathodic microenvironment, where improved proton transfer across CEM counteracts local alkalinity caused by the water reduction reaction ($H_2O + e^- \rightarrow ½H_2 + OH^-$), thereby suppressing the competing HER. At concentrations beyond 1.0 M, both the volumetric CO percentage and FE_{CO} reach a plateau at approximately 9% and ~90%, respectively, as shown in Figures 5.5b and 5.5c. This stabilization likely stems from the membrane's proton transport capacity reaching saturation [165], indicating that proton availability is no longer the rate-limiting factor in the CO_2 electroreduction process. Additionally, the local pH and water content near the cathode tend to stabilize, offering minimal further improvement to the reaction environment. The energy efficiency for CO formation rises from 11.3% at 0.1 M to 33.2% at 1.0 M, as presented in Figure 5.5d. This enhancement

is driven by a combination of lower cell voltage and increased product selectivity, jointly reducing energy losses associated with HER and high overpotentials.

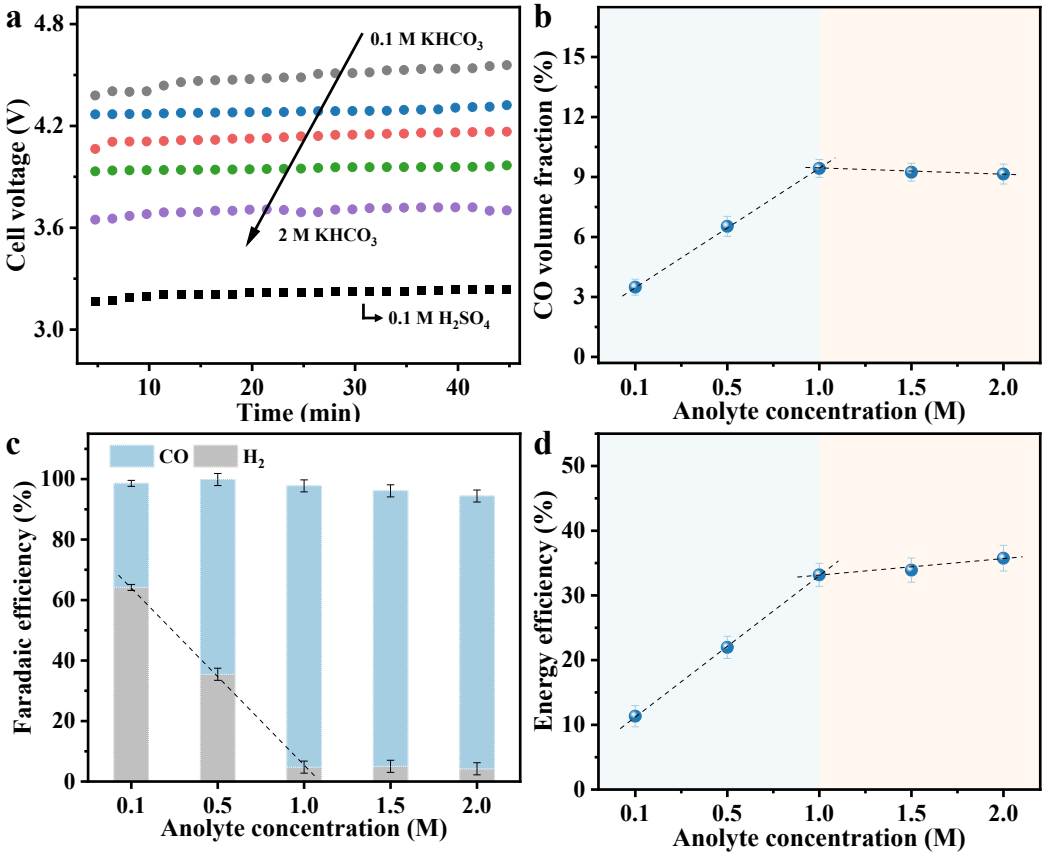

Figure 5.5: (a) Voltage response diagram and (b) volume fraction of the generated CO product detected by GC with different concentrations of anolyte at a constant current of 1200 mA. (c) Faradaic efficiency of carbon monoxide and (d) energy efficiency for CO production with different concentrations of anolyte.

In conclusion, increasing the $KHCO_3$ level leads to reduced cell voltage, enhanced selectivity for CO, and improved energy conversion efficiency. An optimal electrolyte concentration of around 1.0 M represents a balanced condition, providing adequate ionic conductivity and proton mobility, which together enable high CO selectivity, low operational voltage, and steady electrochemical performance.

5.5 Effect of temperature

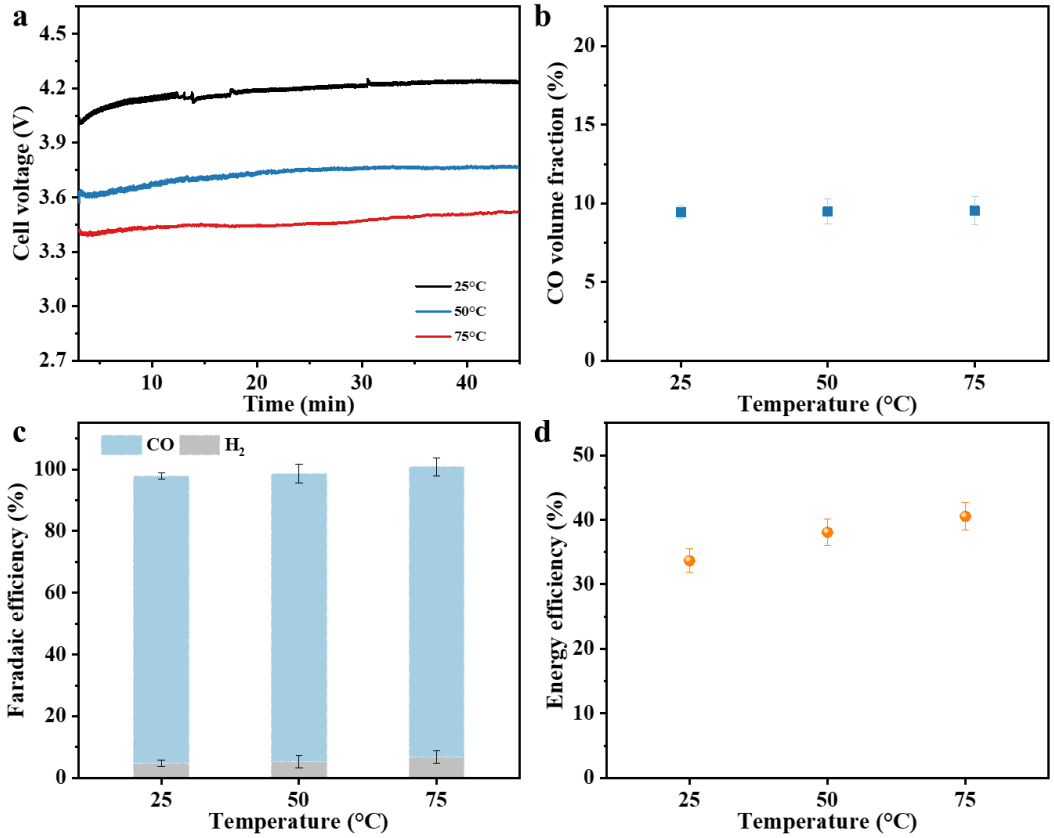

Figure 5.6: (a) Voltage response diagram and (b) volume fraction of the generated CO product detected by GC under different reaction temperatures at a constant current of 1200 mA. (c) Faradaic efficiency of carbon monoxide and (d) energy efficiency for CO production under different reaction temperatures.

The effect of reaction temperature on CO_2RR is systematically investigated, revealing distinct trends in cell voltage, energy efficiency, and Faradaic efficiency. As shown in Figure 5.6a, the full-cell voltage decreases significantly with increasing temperature. At 25 °C, the average operating voltage is 4.2 V; this value drops to 3.7 V at 50 °C and further to 3.5 V at 75 °C. These respective reductions of 0.5 V and 0.7 V indicate that elevated temperatures promote thermal activation of reaction kinetics and reduce the overpotential required for the electrochemical process. This observation aligns with thermodynamic principles, as higher temperatures lower the Gibbs free energy of the reaction, enhance the spontaneity of the process, and facilitate charge-transfer

dynamics at the electrode–electrolyte interface. Despite the reduction in cell voltage, the volumetric concentration of CO gas remains stable across the studied temperature range, as shown in Figure 5.6b. The CO concentration consistently lies between 9.4% and 9.5%, suggesting that the primary reaction pathway and product selectivity are not significantly affected by thermal variation. This stability demonstrates the robustness of the catalytic system and its ability to maintain CO selectivity while suppressing the competing HER under varying thermal conditions.

Figures 5.7c and 5.7d further illustrate the influence of temperature on Faradaic and energy efficiencies. At 25 °C, the Faradaic efficiency for CO is 92%. This value increases slightly to 94% at 50 °C and then remains constant at 94% when the temperature reaches 75 °C. The plateau in FE_{CO} indicates that further thermal elevation beyond 50 °C does not significantly alter the kinetics of CO formation under the present system configuration. In contrast, energy efficiency exhibits a continuous upward trend, from 33.0% at 25 °C to 40.5% at 75 °C, reflecting improved energy utilization as a result of lower voltage requirements and stable product selectivity.

Beyond its kinetic influence, temperature also affects key physicochemical properties of the system. Increasing temperature may change the viscosity of the electrolyte, enhance ionic conductivity, and lowers charge-transfer resistance. These changes improve mass transport and ion mobility and facilitate the desorption of products from the catalyst surface, thereby supporting efficient and stable system operation. However, excessive temperatures may promote unwanted side reactions, accelerate material degradation, and compromise long-term durability. It is therefore critical to define an optimal operating window, such as around 50 °C observed here, that balances performance enhancement with system stability.

5.6 Effect of pressure

Generally, increasing pressure enhances the solubility of CO_2 in the electrolyte, thereby improving reactant availability and mass transport in many electrochemical systems. This effect typically leads to higher reaction rates and improved selectivity in conventional flow-cell electrolyzers, where dissolved CO_2 must be diffused through the

electrolyte to reach the catalyst surface. In contrast, the zero-gap design is characterized by extremely short diffusion pathways and intimate contact among the catalyst layer, membrane, and gas diffusion electrode. In this configuration, gaseous CO_2 is directly supplied to the catalyst surface through the gas diffusion layer, circumventing reliance on CO_2 solubility in the bulk electrolyte. Consequently, CO_2 mass transport is not limited by dissolved concentration, and the enhanced solubility afforded by elevated pressure does not necessarily translate into significant performance improvements.

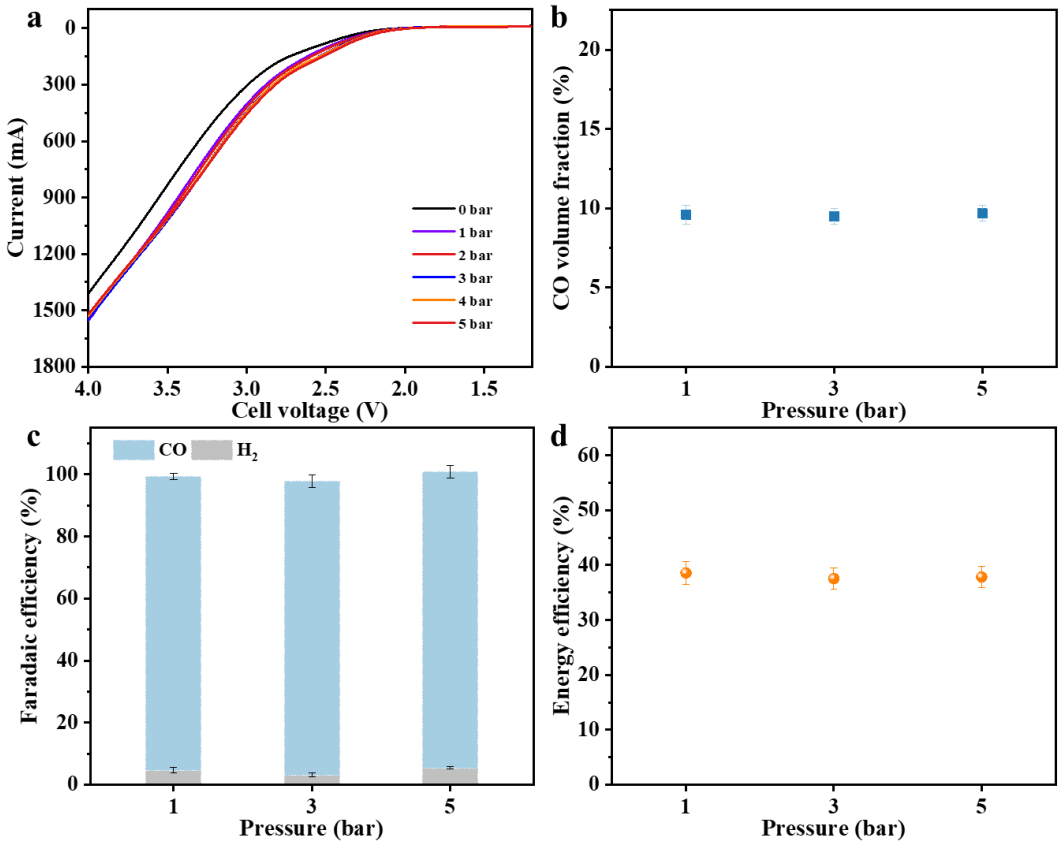

Figure 5.7: (a) LSV curves under different reaction pressure. (b) The volume fraction of the generated CO product detected by GC under different reaction pressures at a constant current of 1200 mA. (c) Faradaic efficiency of carbon monoxide and (d) energy efficiency for CO production under different reaction pressures.

The influence of system pressure on CO_2RR in a zero-gap electrolyzer is systematically evaluated through experimental data. As illustrated in Figure 5.7a, the

overall reaction rate remains largely unchanged within the pressure range of 1 to 5 bar. Correspondingly, Figure 5.7b shows that the volumetric concentration of CO gas remains stable, varying only slightly between 9.5% and 9.6% over this pressure interval. These results indicate that moderate increases in pressure do not substantially affect CO production selectivity or yield in the system.

Further analysis, as presented in Figure 5.7c, reveals only minor changes in Faradaic efficiencies for CO and hydrogen with increasing pressure from 1 to 5 bar. The FE_{CO} exhibits a modest rise from approximately 93% to 95%, while FE of H_2 decreases slightly from around 6% to 3%. This marginal variation suggests that, within this pressure range, the influence on competing reaction pathways, such as hydrogen evolution, is limited. Similarly, Figure 5.7d demonstrates that overall energy efficiency experiences only a slight improvement, increasing from 37.5% to 38.6% as pressure rises. The relatively small impact on energy efficiency reflects the minimal effect of moderate pressure changes on the electrochemical cell voltage and reaction kinetics.

Therefore, within the 1 to 5 bar range, pressure exerts limited influence on Faradaic efficiency, energy efficiency, and product selectivity in zero-gap electrolyzers. This underscores the importance of optimizing other parameters, such as temperature, electrolyte concentration, membrane properties, and catalyst design, to improve overall system performance. Additionally, operating at near atmospheric or moderately elevated pressures can reduce system complexity, capital costs, and safety concerns associated with high-pressure operation.

5.7 Phenomenon of carbonate precipitation

In zero-gap CO_2 electrolyzers using a cation exchange membrane, H^+ are transported from the anode to the cathode, which theoretically should maintain an acidic environment at the cathode. However, in practice, carbonate precipitation is frequently observed on the cathode side, especially within the GDE structure, as illustrated in Figure 5.8. Similar deposition phenomena have been frequently observed in MEA systems [44, 144, 181].

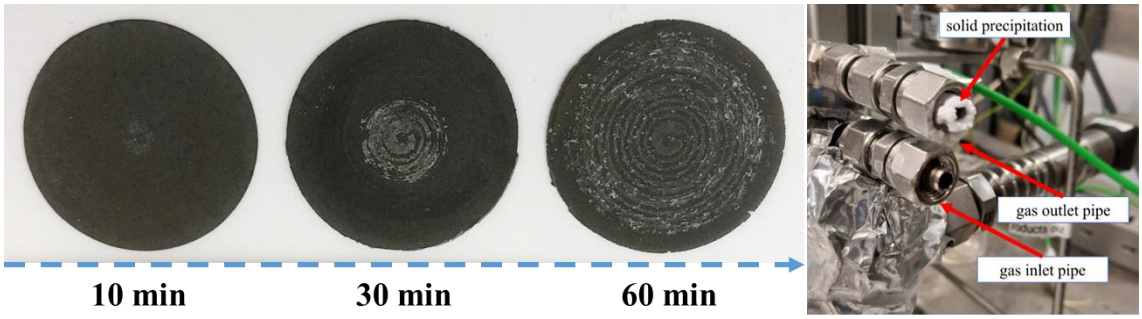

Figure 5.8: Optical photos of the deposits in the pipe and on the back of the cathode after the experiment.

This phenomenon arises due to local alkalization effects caused by electrochemical reactions and limitations in mass transport. Although the cathode does not receive bulk liquid electrolyte, the CEM remains hydrated by the anolyte, which is sufficient to support water reduction ($H_2O + e^- \rightarrow \frac{1}{2}H_2 + OH^-$) that produces hydroxide ions. These OH^- ions accumulate in the confined interfacial region, sharply increasing the local pH. Meanwhile, gaseous CO_2 supplied to the cathode dissolves in this hydration layer and reacts with OH^- to form bicarbonate (HCO_3^-) and subsequently carbonate (CO_3^{2-}), via the reactions $CO_2 + OH^- \rightarrow HCO_3^-$ and $HCO_3^- + OH^- \rightarrow CO_3^{2-} + H_2O$. The rate of proton delivery through the CEM is often insufficient to neutralize the generated OH^-, particularly at high current densities. Furthermore, cations such as K^+, which originate from the ionomer binder or diffuse back from the anode, can interact with CO_3^{2-} to form solid carbonate salts like K_2CO_3. These deposits accumulated next to the GDE block channels and affect gas delivery, which limits the stable operation of the system to less than an hour.

These findings suggest that the local cathode chemical environment is not only controlled by membrane properties or bulk pH, but also by the interfacial water dynamics, ion accumulation, and electrochemical kinetic interactions. Some possible measures include designing membranes with higher ion selectivity to suppress cation crossover, adjusting electrolyte formulation to suppress carbonate formation, optimizing water and gas management, or implementing regular maintenance programs such as flushing or flow circulation [182].

5.8 Conclusion

This chapter is devoted to the study of the performance of the electroreduction of carbon dioxide to carbon monoxide in a zero-gap electrolyzer based on cation exchange membranes. The performance of CO_2RR is influenced by several key factors, including catalyst loading, flow rate, temperature, pressure, and electrolyte concentration. Increasing catalyst loading does not necessarily lead to a proportional increase in reaction rate. Although thicker catalyst layers increase the overall catalytic loading, the relationship between catalyst loading and reaction rate is not linear, suggesting that other factors, such as mass transport limitations or catalyst efficiency, play a more important role. On the other hand, the selection of an appropriate flow rate and pressure is critical for optimizing single-pass conversion rate. Higher flow rates and pressures improve mass transport, reducing concentration polarization and enhancing the selectivity towards desired products, particularly carbon monoxide. Temperature and electrolyte concentration have a profound impact on both reaction rate and energy efficiency. Elevated temperatures can accelerate the reaction kinetics and also reduce the power consumption, thus affecting the overall energy efficiency. Similarly, higher electrolyte concentrations can increase the conductivity, improving the reaction rate but may also alter the product distribution. Overall, the optimal balance of these parameters is crucial for maximizing the efficiency of CO_2 electroreduction, with each factor contributing to either improving mass transport, enhancing catalytic activity, or optimizing energy consumption. The main content of Chapter 5 has been published as a peer-reviewed article entitled “Experimental study of operating parameters in zero-gap CO_2 electrolysis” in Frontiers in Catalysis [183].

6 CO_2RR in Unconventional Conditions

6.1 Insights of CO_2RR at high temperature

High-temperature electrocatalytic CO_2RR presents considerable potential, particularly when coupled with DAC technology [184], offering a promising route for sustainable carbon recycling. Thermodynamically, elevated temperatures reduce the Gibbs free energy of the reaction, thereby lowering the overpotential and enhancing both reaction kinetics and energy conversion efficiency [185]. Integrating the benefits of high-temperature operation with the molecular selectivity of membrane-based separation can significantly boost reaction rates and product yields.

Beyond these electrocatalytic advantages, high temperatures also enable the possibility of thermal catalytic processes occurring either simultaneously or sequentially with electrochemical steps. This opens pathways for tandem or hybrid reaction schemes, such as those resembling Fischer–Tropsch synthesis, where thermally driven C–C coupling can complement electrochemical CO formation. In this context, the catalyst layer design becomes critical. The use of bifunctional or hierarchical catalysts, capable of promoting both electrocatalytic CO_2RR and thermocatalytic transformations, offers a unique opportunity to leverage high-temperature conditions for enhanced hydrocarbon production. Such integrated systems hold the potential to overcome the selectivity and efficiency bottlenecks of conventional CO_2RR processes.

Nevertheless, to realize high-temperature electrocatalytic CO_2RR requires addressing several material and process challenges. One of the main issues is the thermal and chemical stability of ion exchange membranes, as many commercial materials degrade above 90 °C [120]. To overcome this, advanced membranes such as BASF Celtec proton exchange membranes, which are stable above 100 °C [186-188], have emerged as viable solutions. In the present work, these high-temperature membranes are successfully integrated into a zero-gap electrolyzer to investigate the energy efficiency and product selectivity of CO_2RR under elevated temperatures.

6.2 Experimental methodology

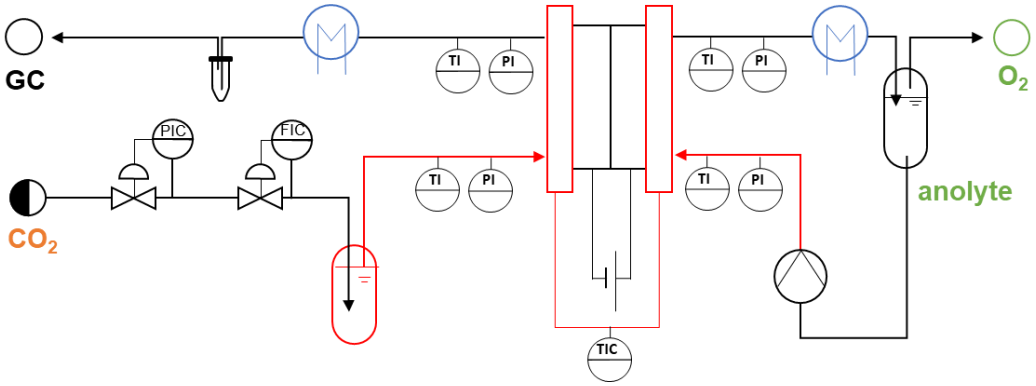

Figure 6.1: P&ID for high-temperature CO_2RR system.

Considering that the thickness of the Celtec membrane is 360-400 μm according to the manufacturer information, another anode flow field was used in the experiments in this section. The anode flow field includes a 250-micron thick gap at the top to properly compress the MEA section to ensure intimate contact between the catalyst layer, GDL, and membrane within the reactor. The Celtec proton exchange membrane remains untreated and is merely cut into small circular pieces with a diameter of 4.8 cm. In the remodeled zero-gap MEA electrolyzer described above, the cell voltage is the potential difference between the cathode and the anode with no iR compensation. 1 M $KHCO_3$ anolyte was circulated by an HPLC pump with a flow rate of 30 mL min^{-1}. CO_2 was bubbled through a cylinder filled with water at 80 °C before entering the reactor, and the electrolytic cell was heated to different temperatures (120 °C -180 °C) by inserting heat cartridges. In this section, cooling water with a temperature of 5 °C pumped by a water cooler device is circulated through the two tube-in-tube heat exchangers downstream of the electrolyzer outlet. The P&ID for this high-temperature CO_2RR system is shown in Figure 6.1.

6.3 CO_2RR performance with high temperature membrane

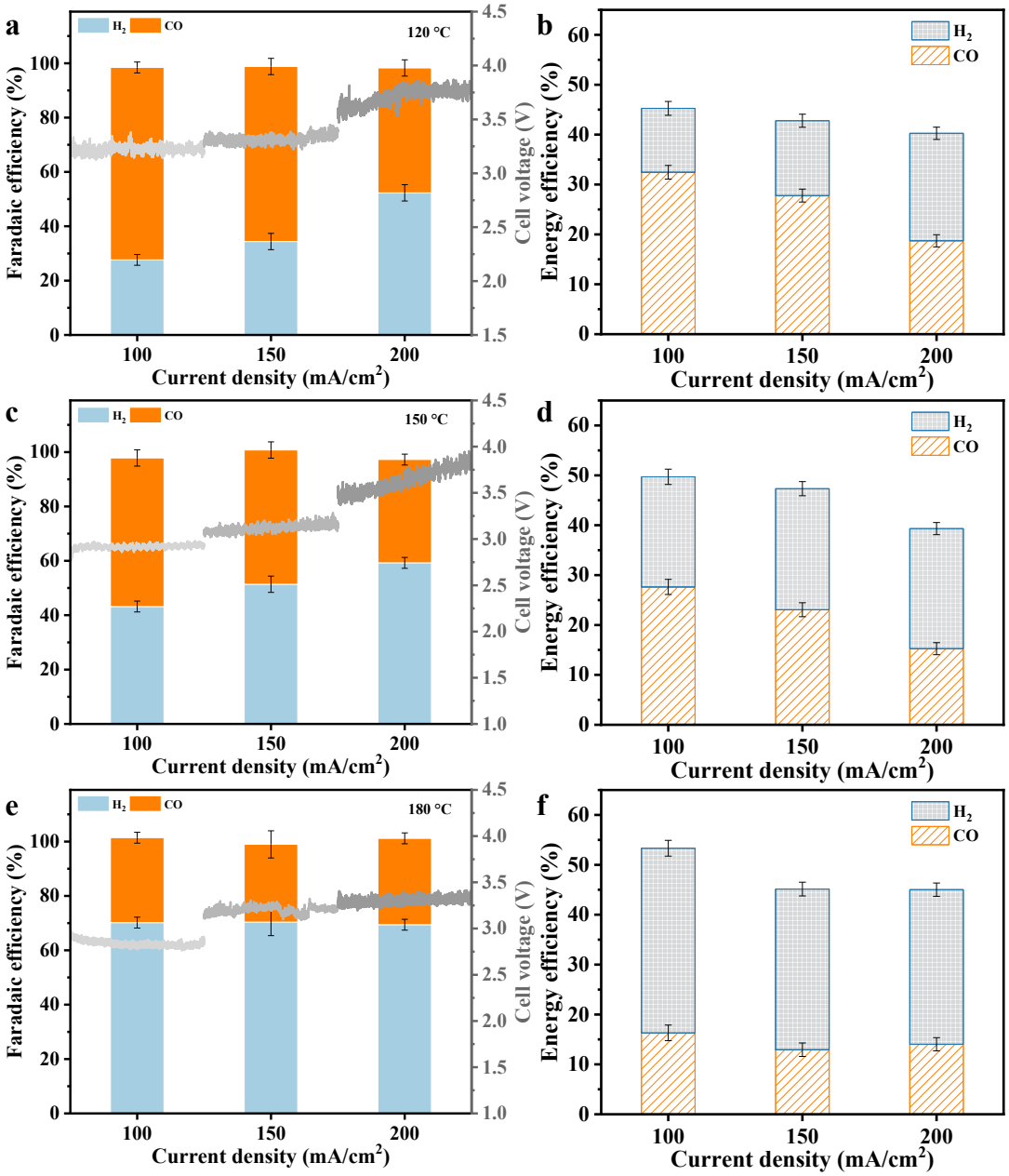

Figure 6.2: Performance of CO_2RR based on silver catalyst with HTPEM. (a, b) Voltage, FE, and energy efficiency at 120 °C; (c, d) at 150 °C; (e, f) at 180 °C.

The silver catalyst, which demonstrates high FE_{CO} in the low-temperature CO_2RR experiments described in Chapter 5, is again employed as the cathode to evaluate its catalytic performance at elevated temperatures ranging from 120 °C to 180 °C. As shown

in Figure 6.2a, the cell voltage required to sustain current densities of 100, 150, and 200 mA/cm^2 at 120 °C is 3.2 V, 3.4 V, and around 3.65 V, respectively. The corresponding FE_{CO} is 70.1%, 64.4%, and 45.9%. Figure 6.2b shows that the overall energy efficiencies reach 45.5%, 40.1%, and 31.7%, while the carbon-based energy efficiencies, considering only CO as the target product, account for 32.4%, 27.8%, and 18.7%, respectively. At 150 °C (Figure 6.2c), the voltage required to maintain current densities of 100, 150, and 200 mA/cm^2 decreases to 2.9 V, 3.14 V, and 3.65 V, respectively. Corresponding FE_{CO} decline to 54.6%, 49.4%, and 38.0%, with total energy efficiencies (including both hydrogen and CO products) reported as 39.6%, 35.1%, and 27.2% (Figure 6.2d). Further increasing the temperature to 180 °C reduces the required voltages to 2.81 V, 3.24 V, and an average of 3.32 V for the respective current densities (Figure 6.2e), while FE_{CO} falls to 31.2%, 28.6%, and 31.7%. Interestingly, total energy efficiencies improve to 53.3%, 45.1%, and 45.0% (Figure 6.2f), reflecting contributions from hydrogen evolution alongside CO production.

These results reveal a clear trend where increasing temperature leads to reduced cell voltage at constant current densities, indicating improved electrochemical kinetics and lowered overpotentials. However, the Faradaic efficiency for CO production declines with temperature elevation, reflecting a shift in product selectivity likely due to enhanced hydrogen evolution reaction competing at higher temperatures. Despite this, the overall energy efficiency remains relatively high at elevated temperatures due to the combined energy contributions of CO and hydrogen products. This interplay highlights the complex trade-off between thermodynamic advantages and selectivity limitations at elevated temperatures.

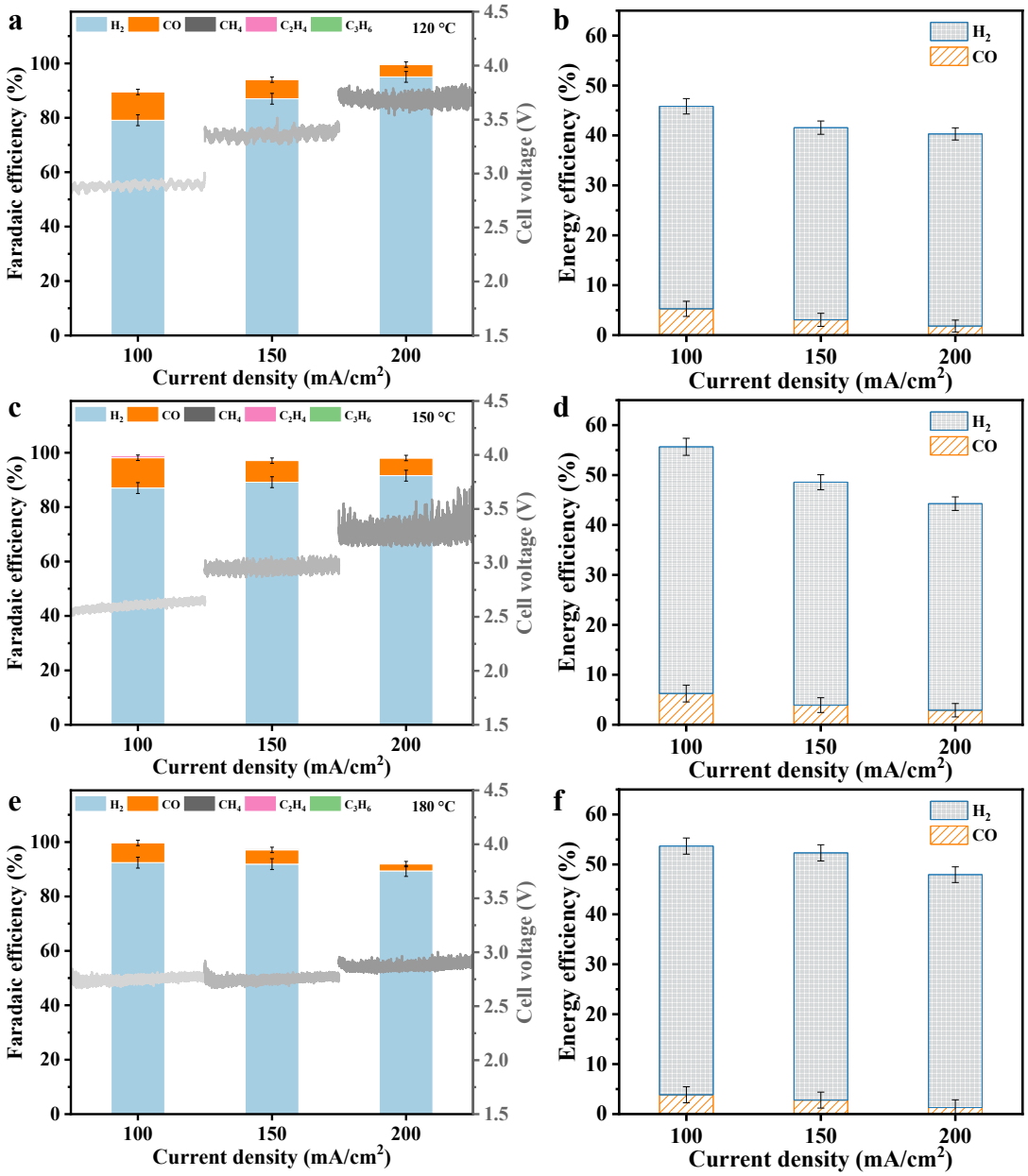

Figure 6.3: Performance of CO_2RR based on copper catalyst with HTPEM. (a, b) Voltage, FE, and energy efficiency at 120 °C; (c, d) at 150 °C; (e, f) at 180 °C.

The copper catalyst was also employed as the cathode for CO_2 electroreduction at elevated temperatures ranging from 120 °C to 180 °C. As shown in Figure 6.3a, the cell voltages required to sustain current densities of 100, 150, and 200 mA/cm^2 at 120 °C are 2.87 V, 3.37 V, and 3.67 V, respectively. The corresponding FE_{CO} are 10.4%, 7.0%, and 4.5%, while the total energy efficiencies (including both CO and H_2) reach 45.8%, 41.5%,

and 40.2%, respectively (Figure 6.3b). At 150 °C (Figure 6.3c), the required voltage decreases to 2.6 V, 2.95 V, and 3.3 V, and CO selectivity improves slightly, with FE_{CO} values of 11.1%, 7.9%, and 6.5%. The corresponding total energy efficiencies increase to 55.6%, 48.5%, and 44.2% (Figure 6.3d). Further temperature elevation to 180 °C (Figure 6.3e) yields voltages of 2.73 V, 2.78 V, and 2.87 V, respectively, but CO selectivity decreases notably, with FE_{CO} values dropping to 7.2%, 5.2%, and 2.5%. Nevertheless, total energy efficiencies remain relatively high at 53.6%, 52.3%, and 47.9% (Figure 6.3f), due to the dominant contribution of hydrogen evolution. Across all tested temperatures, mainly CO and H_2 are detected, in contrast to low-temperature CO_2RR on copper where C_2 products are also observed, enabled by C–C coupling pathways. The absence of C_2 products here indicates a shift in selectivity, that is, high-temperature electrocatalytic CO_2RR actually optimizes HER.

In the presence of suitable catalysts, long-chain hydrocarbons can form via C–C coupling when CO and H_2 are supplied in appropriate ratios under high-temperature and high-pressure conditions. However, in the current system, high temperatures primarily enhance hydrogen production through electrocatalysis, while thermal catalysis remains inefficient. This could be due to both the intrinsic properties of the catalyst and the lack of sufficiently harsh thermocatalytic conditions (i.e., inadequate temperature or pressure). As a result, the desired thermochemical synergy is not fully realized, and the system remains dominated by HER and C_1 products. This outcome highlights both the potential and the challenge of integrating high-temperature electro- and thermocatalytic processes: while temperature facilitates improved kinetics, achieving complex product formation will require both optimized catalyst design and more rigorous thermochemical control.

6.4 Conclusion

A high-temperature setup was developed, capable of operation up to 180 °C, enabling the membrane electrode assembly electrolyzer to perform CO_2 reduction reactions under elevated temperature conditions. Although the system is equipped for high-pressure operation, high-pressure conditions were not employed in the present study. High temperatures can promote electrolyte evaporation; therefore, a large electrolyte

volume was supplied to maintain stable operation. This limitation could be addressed in future studies by combining high-temperature and high-pressure conditions to suppress electrolyte loss, allowing greater focus on cathodic CO_2RR performance. Despite this limitation, the setup demonstrates significant advancement in high-temperature CO_2RR.

CO_2 electroreduction in high-temperature proton exchange membrane systems presents both compelling opportunities and critical challenges. Elevated temperatures facilitate faster charge transfer and reduce cell voltages, but also intensify the competing HER, which compromises selectivity toward carbon-based products such as CO and multicarbon species. This effect is particularly pronounced in acidic, proton-conductive environments, where HER becomes increasingly dominant. Long-term operation is further hindered by catalyst deactivation, membrane fouling, and gas crossover, all of which affect durability and scalability. To address these limitations, future efforts should prioritize the development of thermally stable and selective catalysts that resist sintering and maintain activity under harsh conditions, alongside robust membrane materials capable of sustaining high-temperature, high-current electrolysis without significant degradation. One promising strategy involves the design of tandem catalyst systems: the first component optimized for efficient electrochemical production of CO and H_2 (syngas), and the second tailored for thermocatalytic conversion of syngas into higher hydrocarbons at milder temperatures. When combined with pressurized operation and co-fed reactants, such hybrid approaches may unlock more selective, energy-efficient, and continuous pathways for CO_2 valorization.

7 Conclusions and outlook

7.1 Summary of some remarkable results

In the process of transitioning from fundamental research to production scaling, it is imperative to explore and evaluate the comprehensive performance of CO_2 electroreduction reactions. With a keen interest and guidance in this area, the objective of this doctoral thesis is to enhance the efficiency of CO_2 electrochemical reduction reactions for C_1-C_3 gas products, while overcoming challenges associated with the stable operation of electrolyzers, thereby contributing to carbon neutrality and the transition to clean energy. To achieve this goal, a series of optimization strategies are employed, including adjustments to the electrochemical reactor structure, optimization of catalyst performance, and exploration of the influence of temperature and pressure on energy efficiency (Figure 7.1).

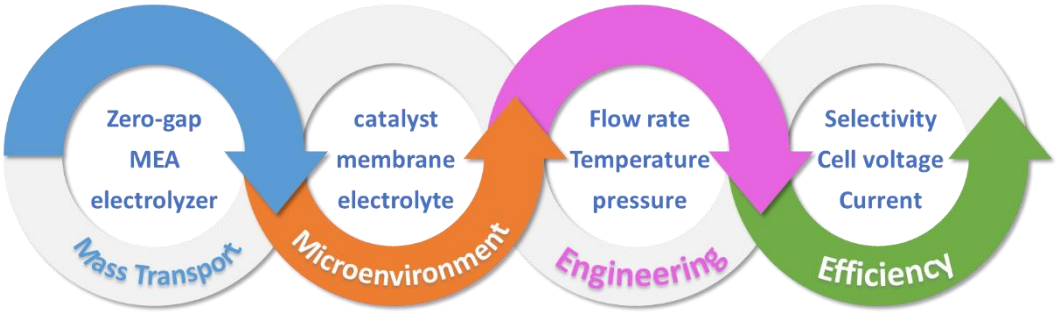

Figure 7.1: Content and relevance of experimental research in this dissertation.

Both AEM and CEM systems in the zero-gap electrolyzers are investigated to evaluate their advantages. The AEM system demonstrated superior energy efficiency and lower voltage requirements, particularly under alkaline conditions with 1 M KOH. This setup achieved 48% energy efficiency at 100 mA/cm^2 and 40% at 200 mA/cm^2 while maintaining FE_{CO} above 90% under moderate temperatures (50 °C). In contrast, the CEM system, though requiring higher energy input, provided insights into the role of electrolyte concentration and flow dynamics, with energy efficiencies improving to 32% using 2 M $KHCO_3$.

Catalyst selection and modification were critical in optimizing CO_2 reduction pathways. Ag catalysts were predominantly used for CO production due to their high selectivity and stability, achieving FE_{CO} consistently above 90% across varied flow rates and catalyst loadings. In AEM-MEA systems, copper-based catalysts enabled the production of higher-value C_{2+} products. Alkaline environments (1 M KOH) enhanced conductivity and reduced voltage requirements (3.23 V at 200 mA/cm^2) but limited C_{2+} Faradaic efficiency to 26%-38%. Moderately alkaline electrolytes (0.1 M $KHCO_3$) shifted product distribution towards CO and ethylene, with potassium ions promoting the formation of C_3 products. Tandem catalysts such as Cu/Ag improved CO selectivity but reduced C_2-C_3 product yields due to the rapid desorption of CO intermediates, underscoring the trade-offs between selectivity and overall productivity.

Operating conditions were systematically varied to enhance reaction performance, including temperature, pressure, and electrolyte concentration. Elevated temperatures improved reaction kinetics and thermodynamics, as demonstrated in AEM-MEA systems where energy efficiency increased by over 10% under pressurized and high-temperature conditions compared to ambient operations. Similarly, in CEM-MEA systems, increasing temperature from ambient to 75 °C raised energy efficiency from 28% to 37%. Pressure studies revealed that pressurization (1-5 bar) could push total Faradaic efficiency close to 100%, with FE_{CO} reaching 95% and energy efficiencies stabilizing around 35%. However, carbonate precipitation remained a limiting factor, particularly in alkaline systems, requiring strategies such as humidified CO_2 vapor to mitigate its impact and extend operational stability to over 100 hours in neutral electrolytes.

Performance metrics were evaluated to determine the efficiency, selectivity, and stability of the systems under study. The high selectivity of Ag for CO was validated across varying parameters, with energy efficiency peaking at 48% in AEM systems under alkaline conditions. For copper-based catalysts, the balance between C_{2+} product formation and competing hydrogen evolution reactions was assessed, revealing the need for optimized catalyst design and electrolyte composition. High-temperature proton exchange membranes were introduced in Chapter 6, highlighting their potential for high-temperature operations. However, challenges such as reduced CO selectivity, membrane

fouling, and degradation limited their effectiveness, emphasizing the need for further material innovation.

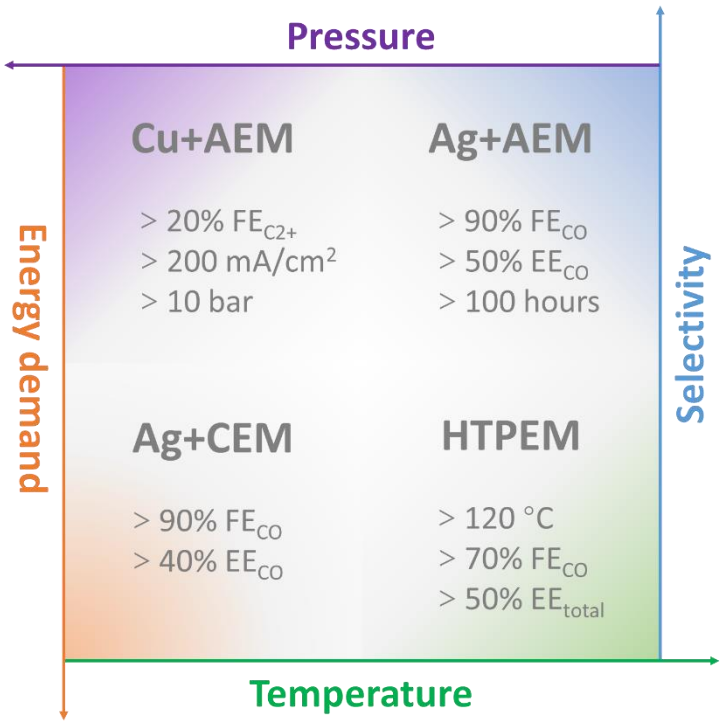

Figure 7.2: Most remarkable results obtained from the experiments in this dissertation.

The most remarkable results from the above chapters are shown in Figure 7.2 and some important parameters for zero-gap electrolyzer operation are listed in Table 7.1. Well-designed microenvironments and reasonable operating conditions can increase reaction rates and reduce energy consumption. In conclusion, the comprehensive integration of these methodologies in this dissertation underscores the interplay between reactor design, catalyst performance, and operating conditions in advancing CO_2 electroreduction technologies. The data-driven approach not only provides a framework for optimizing existing systems but also shows the potential to address current limitations and enhance the scalability of these systems.

Table 7.1: Some important parameters for zero-gap electrolyzer operation.

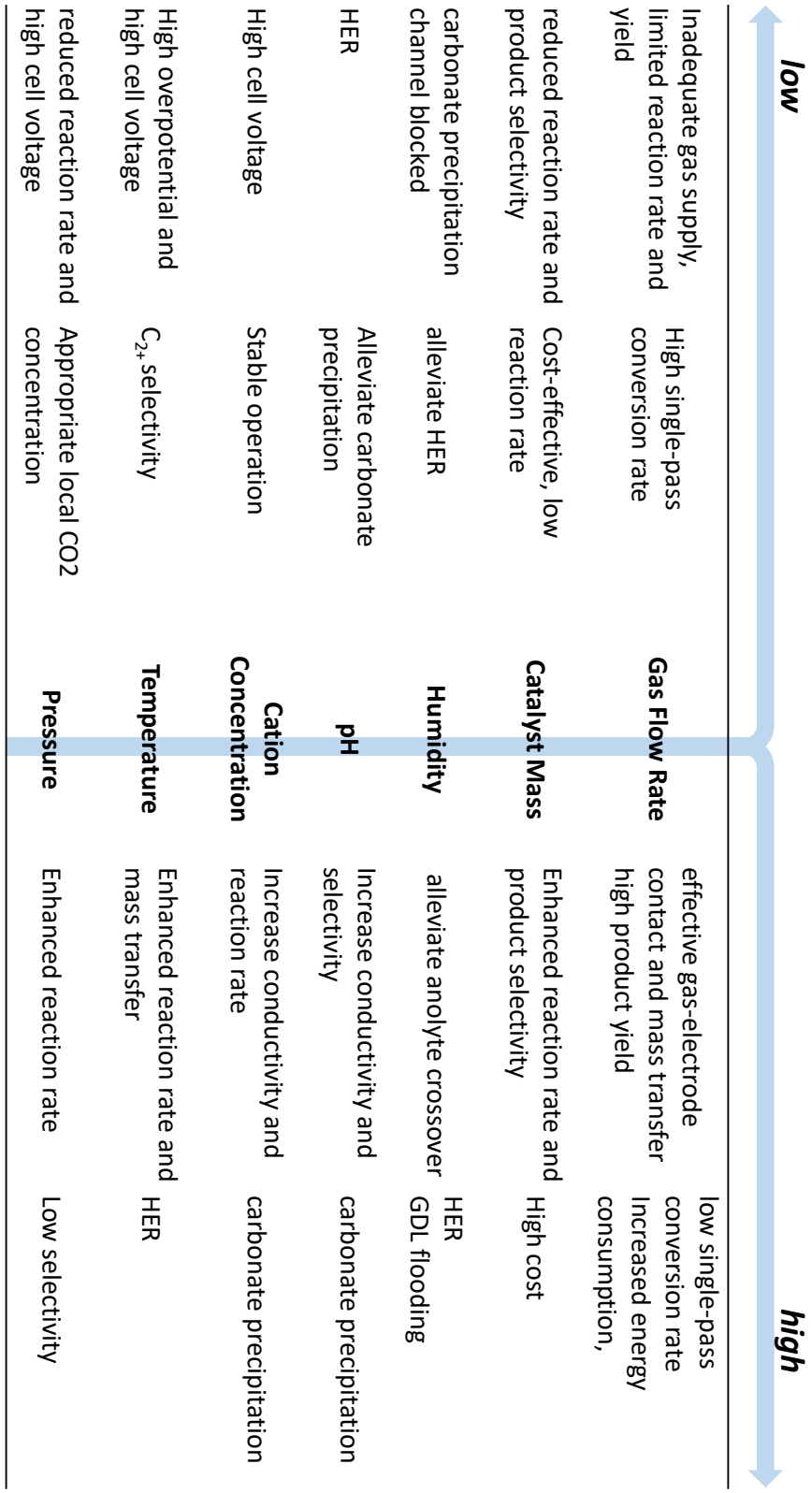

7.2 Outlook

To achieve significant improvements in CO_2RR field will require coordinated advances across catalyst design, electrolyte engineering, reaction condition optimization, and system integration. The possible future development prospects are as follows.

Ensuring long-term stability and operational efficiency is essential for practical deployment. MEA-based electrolyzers are prone to issues such as carbonate deposition, electrode flooding, and gas crossover. These challenges may be addressed through careful electrolyte formulation, improved electrolyzer architecture, and the development of ion exchange membranes with enhanced mechanical robustness, reduced gas permeability, and high ionic conductivity.

Catalyst innovation remains central to progress. Designing novel catalysts, such as bimetallic alloys, core–shell structures, and nanostructured composites, offers pathways to increase activity and selectivity toward desired products. Precise control over morphology, composition, and surface atomic arrangements can maximize active site density, enhance reactant binding, and lower energy barriers for key transformations.

A deeper mechanistic understanding of CO_2 reduction is also critical. Elucidating reaction pathways, surface kinetics, and intermediate species through a combination of computational modeling, advanced spectroscopy, and machine learning–driven data analysis will inform rational catalyst design and operational strategies.

Moreover, integrating electrochemical CO_2 reduction with thermocatalytic upgrading offers a promising route to enhance both selectivity and efficiency. Tandem systems that combine an electrochemical step, optimized for syngas production, with a downstream thermocatalytic reactor for C–C coupling and hydrocarbon formation could circumvent the limitations of each process alone. This hybrid strategy is particularly relevant for converting low-value intermediates into energy-dense liquid fuels or chemical feedstocks under controlled temperature and pressure. Finally, embedding these approaches within broader carbon management frameworks, such as carbon capture, storage, and utilization, will be essential to closing the carbon loop and enabling

sustainable industrial implementation. Continued interdisciplinary collaboration will be key to transforming CO_2 from a waste product into a valuable carbon resource.

Appendix

A1 H-cell electrolyzer

The three-electrode electrochemical measurements were conducted at room temperature in a gas-tight H-type cell separated by a Sustainion® anion exchange membrane. Both compartments were filled with 50 mL of either 0.1 M $KHCO_3$ or 1 M KOH as the electrolyte. Iridium dioxide on titanium (IrO_2@Ti) and silver on carbon paper (Ag@Carbon) with a surface area of 1 cm^2, were employed as the working and counter electrodes, respectively, with an Ag/AgCl electrode (saturated with KCl) serving as the reference electrode in the cathode chamber. The potential measurements were converted to the reversible hydrogen electrode (RHE) scale using the relationship E(vs RHE) = E (vs Ag/AgCl) + 0.197 + 0.0591 × pH [189, 190]. The pH value of the electrolyte was determined by an LLG-pH Meter.

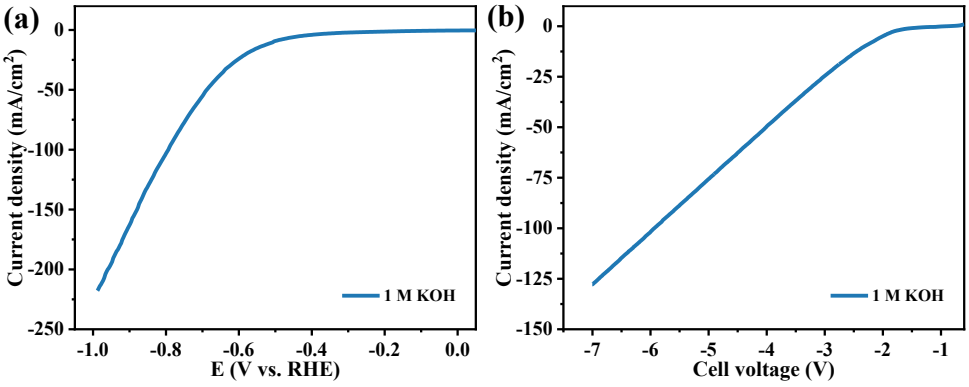

Figure A1.1: LSV curves at a scan rate of 10 mV/s in an H-cell with 1 M KOH as electrolytes.

To evaluate the performance of the prepared catalyst in alkaline electrolytes, linear sweep voltammetry (LSV) curves were measured in an H-cell with 1 M KOH as both catholyte and anolyte. Figure A1.1 depicts that the electrocatalysis started at -0.5 V vs. RHE and reached 200 mA/cm^2 at -0.88V vs. RHE. However, two-electrode tests have proven that a large cell voltage (≥ 6 V) is desired in an H-cell to maintain a sufficient

reaction rate (≥ 100 mA/cm^2), which is blamed on the hindered mass transport in a liquid electrolyte system.

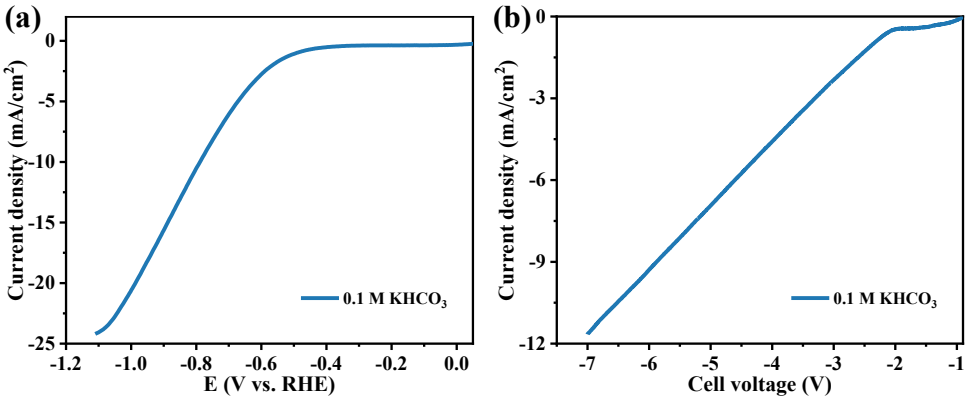

Figure A1.2: LSV curves at a scan rate of 10 mV/s in an H-cell with 0.1 M $KHCO_3$ as electrolytes.

The LSV curves were measured in an H-cell with pure CO_2 saturated 0.1 M $KHCO_3$ as both catholyte and anolyte. The electrocatalytic activity was initiated at -0.5 V vs. RHE, but Figure A1.2 illuminates that it could only play a current density of 20 mA/cm^2·at -1.0·V vs. RHE and the two-electrode test within the H-cell also expresses the appetite for an exaggerated cell voltage.

A2 Flow electrolyzers

Analysis of liquid products in flow cell systems is critical for understanding reaction pathways and improving catalyst design. Liquid products are often more difficult to detect and quantify than the gaseous products due to their low concentrations and the potential for crossover or mixing within the electrolytes. Flow cells feature a controlled reaction environment and separate liquid and gas outlets, which simplifies sample collection and enables more precise measurements. Advanced analytical techniques, such as nuclear magnetic resonance (NMR) spectroscopy, are often used to accurately quantify liquid products. NMR is particularly advantageous due to its non-destructive nature, high sensitivity, and ability to distinguish similar molecular structures.

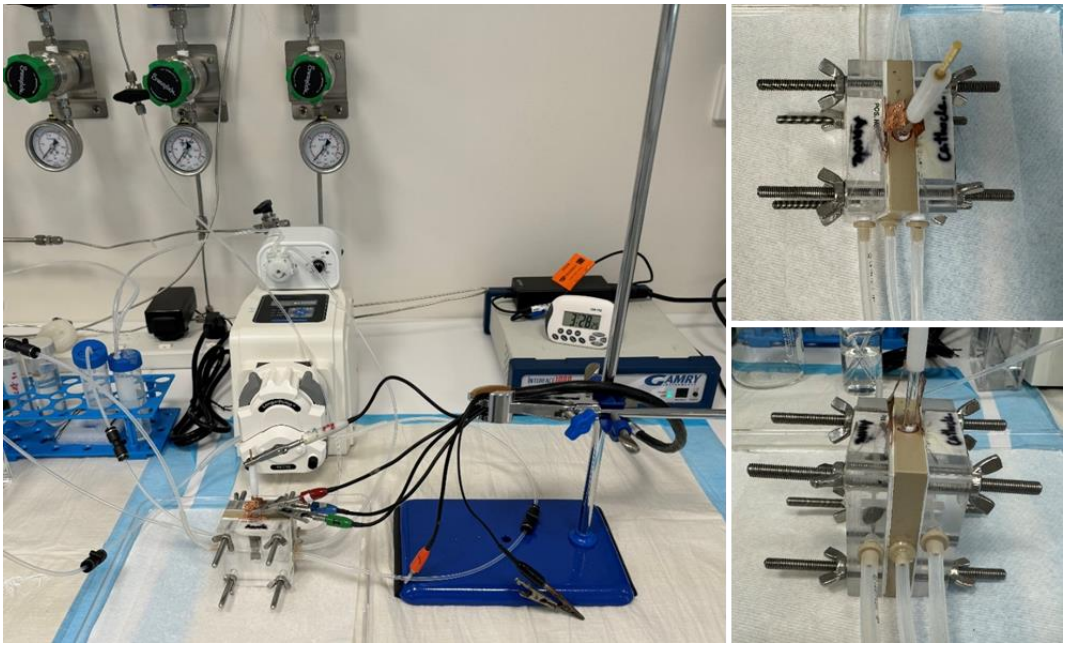

Figure A2.1: Photos of the CO_2RR system based on a flow electrolyzer.

The CO_2RR performance test was conducted in a flow cell using a three-electrode system and monitored by a Garmy electrochemical workstation. 6 mg of copper catalyst powder was added to 2 mL of methanol and ultrasonicated to ensure even dispersion. Into the dispersed mixture, 6 µL of a Nafion solution (~5 wt%) was added and ultrasonicated again to form a catalyst ink. The prepared catalyst ink was then sprayed onto a 2 × 2 cm^2 gas diffusion layer to achieve a catalyst loading of approximately 1 mg/cm^2, forming a gas diffusion electrode. The electrode was left to air dry at room temperature overnight to ensure complete drying. The nickel foam was cleaned using ultrasonic cleaning and then dried overnight in an oven at 60 °C. An Ag/AgCl electrode (saturated KCl solution) served as the reference electrode, nickel foam was used as the counter electrode, and a Cu catalyst on carbon paper was used as the working electrode (with an active area of 1 cm^2). Fresh 1 M $KHCO_3$, prepared in a volumetric flask, was used as both the catholyte and anolyte, with a proton exchange membrane (Nafion 115) functioning as the ion exchange membrane. Alternatively, fresh 1 M KOH, also prepared in a volumetric flask, was used as both the catholyte and anolyte with an anion exchange membrane (Fumasep FAB-PK-130). The electrolyte was circulated through the flow cell at a constant rate of 5 mL min^{-1} using a peristaltic pump. High-purity CO_2 gas (99.999%) was controlled by a

mass flow controller at a flow rate of approximately 40 sccm. All electrocatalytic reactions were conducted under ambient pressure and temperature conditions.

Liquid product quantification: 10 mL of electrolyte is circulated on the cathode side, with a continuous reaction for 20 minutes at each given test current. Then, 400 µL of the cathode electrolyte is taken, and 100 µL of DMSO-d6 is added as the locking solvent, along with 100 µL of DSS as an internal standard. Liquid products are measured using 400 MHz 1H-NMR. The concentration of the liquid products is quantified by comparing the area ratio of the liquid product peaks to the DSS peak against a standard curve. The FE_i for a specific product i is calculated using the following equation.

$$FE_i = \frac{m_i \times V \times n_i \times F}{Q_{total}} \times 100\%$$

where m is the measured concentration of the specific product (mol/L); V is the volume of cathode electrolyte (L); n_i is the number of electrons transferred to form specific product; F is the Faradaic constant (96,485 C mol^{-1}); Q is the total charge (C).

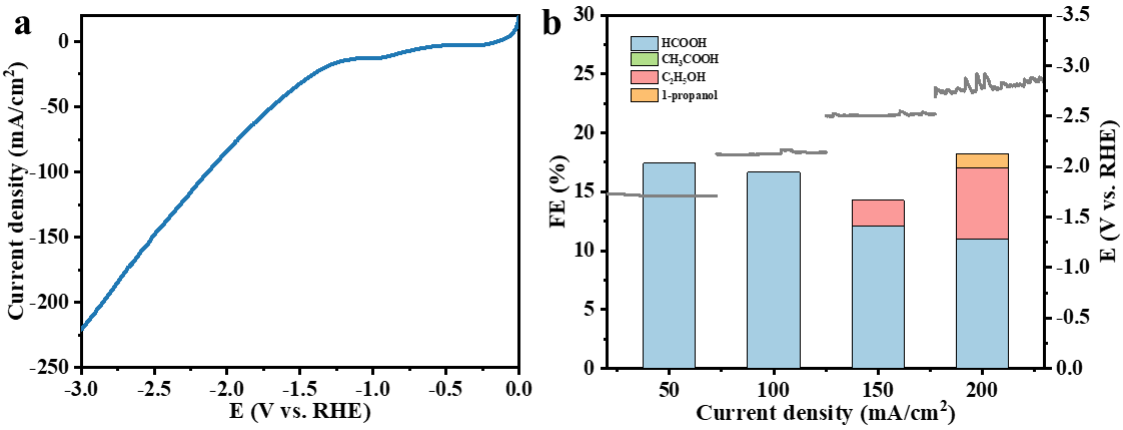

Figure A2.2: Electrochemical performance of a CEM membrane flow electrolyzer with 1 M $KHCO_3$ as electrolyte. (a) LSV curves with a scan rate of 10 mV/s were recorded in a three-electrode electrolytic cell. (b) Faradaic efficiency of the liquid products at each given current test.

As the applied voltage increases, the current density also increases, showing a clear liner correlation between voltage and current above ca. 3 V (Figure A2.2). After applying -1.5 V, the current density increases significantly. Specifically, after reaching -2.8 V, it finally reaches a high value of 200 mA/cm^2. At current densities below 100 mA/cm^2, only formic acid with an Faradaic efficiency of 18% was detected. At higher current densities and voltages, the generation of higher hydrocarbon becomes obvious. Notably, at large currents and voltages, C_2 products such as ethanol were detected, indicating a change in product selectivity. The Faradaic efficiency of these C_2 products increased with the increase in applied voltage and current density, highlighting the importance of optimizing electrochemical conditions for improving the production of multi-carbon compounds. This behavior emphasizes the complexity of CO_2 reduction and suggests that higher voltages promote the formation of more complex products rather than the main formate generation observed at lower currents. However, when monitoring the cell voltage, it was found that to achieve a current density of 150 mA/cm^2, the system requires an extremely high total voltage of up to 8 V (Figure A2.3).

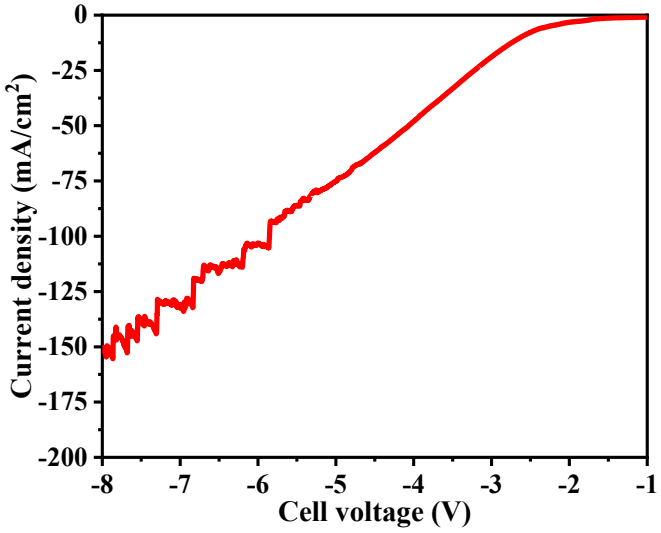

Figure A2.3: LSV curves with a scan rate of 10 mV/s were recorded in terms of electrolyzer cell voltage.

In the flow cell system utilizing an AEM with an alkaline electrolyte, significant improvements in current density were observed compared to systems with CEM under

similar applied potential. Specifically, at an applied potential of -2.2 V, the system achieved a current density of 200 mA/cm^2, as Figure A2.4 shows.

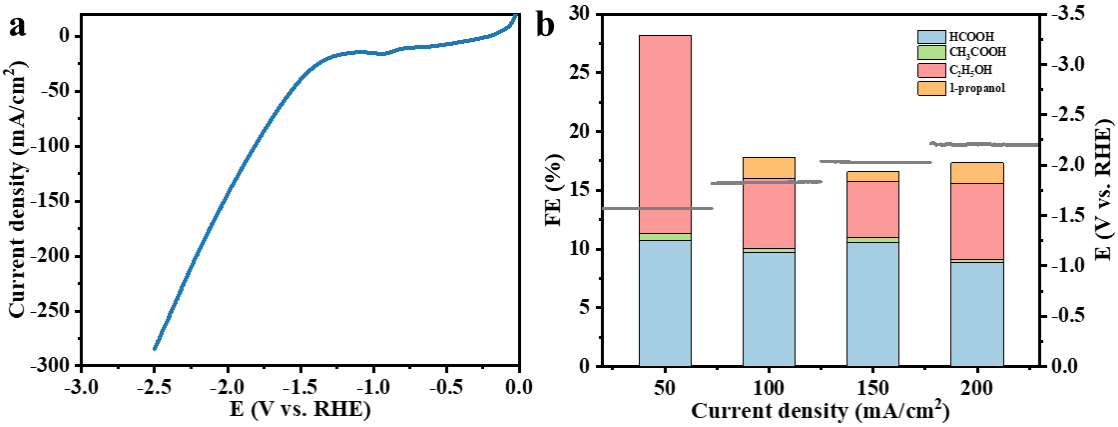

Figure A2.4: Electrochemical performance of an AEM membrane flow electrolyzer with 1 M KOH as electrolyte. (a) LSV curves with a scan rate of 10 mV/s were recorded in a three-electrode electrolytic cell. (b) Faradaic efficiency of the liquid products at each given current test.

At current densities ranging from 50 to 200 mA/cm^2, ethanol production was detected, indicating the formation of C_2 products under these operating conditions. At a current density of 50 mA/cm^2, the Faradaic efficiency for ethanol was found to be 15%. As the current density increased, small amounts of 1-propanol were also detected, suggesting the formation of higher-order carbon products at elevated current densities. This shift to more complex products such as 1-propanol highlights the potential of this system to generate valuable multi-carbon chemicals under the right conditions.

Despite the promising results in terms of product selectivity and current density, the high voltage requirement of 6.5 V to achieve 200 mA/cm^2 significantly limits the economic viability of this system (Figure A2.5). This high voltage demand leads to considerable energy input, making it less practical for large-scale applications. Thus, while the use of an alkaline electrolyte with an AEM enhances the performance of the CO_2 reduction process, further optimization is needed to reduce energy consumption and make the system more energy-efficient and economically feasible for practical deployment.

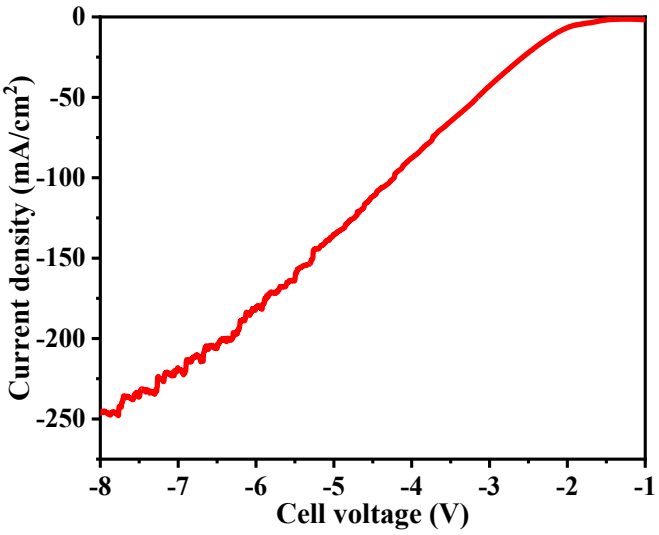

Figure A2.5: LSV curves at a scan rate of 10 mV/s in an H-cell with 0.1 M $KHCO_3$ as electrolytes.

List of Figures

List of Tables

References

[1] M.I. Hoffert, K. Caldeira, A.K. Jain, E.F. Haites, L.D.D. Harvey, S.D. Potter, M.E. Schlesinger, S.H. Schneider, R.G. Watts, T.M.L. Wigley, D.J. Wuebbles, Energy implications of future stabilization of atmospheric CO_2 content, Nature 395 (1998) 881-884.
[2] M. Crippa, E. Solazzo, D. Guizzardi, F. Monforti-Ferrario, F.N. Tubiello, A. Leip, Food systems are responsible for a third of global anthropogenic GHG emissions, Nature Food 2 (2021) 198-209.
[3] C. Rodriguez Franco, D.S. Page-Dumroese, D. Pierson, T. Nicosia, Biochar Utilization as a Forestry Climate-Smart Tool, Sustainability, 2024, 1714.
[4] United States Energy Information Administration, International Energy Outlook, 2018 https://www.eia.gov/outlooks/ieo/.
[5] G. Polya, WMO Warning: 1.5 Degree C Warming Breach Very Soon & With Increasing Frequency. Act Now!, Countercurrents, 2023.
[6] F. Kogan, Remote Sensing Land Surface Changes: The 1981-2020 Intensive Global Warming, Springer Nature (2023).
[7] Y.-M. Wei, J.-N. Kang, L.-C. Liu, Q. Li, P.-T. Wang, J.-J. Hou, Q.-M. Liang, H. Liao, S.-F. Huang, B. Yu, A proposed global layout of carbon capture and storage in line with a 2 °C climate target, Nature Climate Change 11 (2021) 112-118.
[8] K. Anderson, G. Peters, The trouble with negative emissions, Science 354 (2016) 182-183.
[9] G. Centi, S. Perathoner, Green carbon dioxide: advances in CO_2 utilization, John Wiley & Sons (2014).
[10] S.J. Davis, N.S. Lewis, M. Shaner, S. Aggarwal, D. Arent, I.L. Azevedo, S.M. Benson, T. Bradley, J. Brouwer, Y.M. Chiang, C.T.M. Clack, A. Cohen, S. Doig, J. Edmonds, P. Fennell, C.B. Field, B. Hannegan, B.M. Hodge, M.I. Hoffert, E. Ingersoll, P. Jaramillo, K.S. Lackner, K.J. Mach, M. Mastrandrea, J. Ogden, P.F. Peterson, D.L. Sanchez, D. Sperling, J. Stagner, J.E. Trancik, C.J. Yang, K. Caldeira, Net-zero emissions energy systems, Science 360 (2018) 1419.
[11] F. Wang, J.D. Harindintwali, Z. Yuan, M. Wang, F. Wang, S. Li, Z. Yin, L. Huang, Y. Fu, L. Li, S.X. Chang, L. Zhang, J. Rinklebe, Z. Yuan, Q. Zhu, L. Xiang, D.C.W. Tsang, L. Xu, X. Jiang, J. Liu, N. Wei, M. Kastner, Y. Zou, Y.S. Ok, J. Shen, D. Peng, W. Zhang, D. Barcelo, Y. Zhou, Z. Bai, B. Li, B. Zhang, K. Wei, H. Cao, Z. Tan, L.B. Zhao, X. He, J. Zheng, N. Bolan, X. Liu, C. Huang, S. Dietmann, M. Luo, N. Sun, J. Gong, Y. Gong, F. Brahushi, T. Zhang, C. Xiao, X. Li, W. Chen, N. Jiao, J. Lehmann, Y.G. Zhu, H. Jin, A. Schaffer, J.M. Tiedje, J.M. Chen, Technologies and perspectives for achieving carbon neutrality, The Innovation 2 (2021) 100180.
[12] H.D. Matthews, S. Wynes, Current global efforts are insufficient to limit warming to 1.5 degrees C, Science 376 (2022) 1404-1409.
[13] Z. Gong, Carbon Capture, Utilization and Storage (CCUS) Technology Development, Academic Journal of Science and Technology 9 (2024) 32-35.
[14] X. Shang, G. Liu, X. Su, Y. Huang, T. Zhang, A review of the recent progress on direct heterogeneous catalytic CO_2 hydrogenation to gasoline-range hydrocarbons, EES Catalysis 1 (2023) 353-368.
[15] C. Steinlechner, A.F. Roesel, E. Oberem, A. Päpcke, N. Rockstroh, F. Gloaguen, S. Lochbrunner, R. Ludwig, A. Spannenberg, H. Junge, R. Francke, M. Beller, Selective Earth-Abundant System for CO_2 Reduction: Comparing Photo- and Electrocatalytic Processes, ACS Catalysis 9 (2019) 2091-2100.

[16] Y. Zheng, J. Wang, B. Yu, W. Zhang, J. Chen, J. Qiao, J. Zhang, A review of high temperature co-electrolysis of H_2O and CO_2 to produce sustainable fuels using solid oxide electrolysis cells (SOECs): advanced materials and technology, Chem Soc Rev 46 (2017) 1427-1463.
[17] J. Shi, Y. Jiang, Z. Jiang, X. Wang, X. Wang, S. Zhang, P. Han, C. Yang, Enzymatic conversion of carbon dioxide, Chem Soc Rev 44 (2015) 5981-6000.
[18] M. Ronda-Lloret, Y. Wang, P. Oulego, G. Rothenberg, X. Tu, N.R. Shiju, CO_2 Hydrogenation at Atmospheric Pressure and Low Temperature Using Plasma-Enhanced Catalysis over Supported Cobalt Oxide Catalysts, ACS Sustainable Chemistry & Engineering 8 (2020) 17397-17407.
[19] L. Ge, H. Rabiee, M. Li, S. Subramanian, Y. Zheng, J.H. Lee, T. Burdyny, H. Wang, Electrochemical CO_2 reduction in membrane-electrode assemblies, Chem 8 (2022) 663-692.
[20] F. Xie, R. Chen, X. Zhu, Q. Liao, D. Ye, B. Zhang, Y. Yu, J. Li, CO_2 utilization: Direct power generation by a coupled system that integrates photocatalytic reduction of CO_2 with photocatalytic fuel cell, Journal of CO_2 Utilization 32 (2019) 31-36.
[21] R. Daiyan, I. MacGill, R. Amal, Opportunities and Challenges for Renewable Power-to-X, ACS Energy Letters 5 (2020) 3843-3847.
[22] R. Dittmeyer, M. Klumpp, P. Kant, G. Ozin, Crowd oil not crude oil, Nat Commun 10 (2019) 1818.
[23] C. Panzone, R. Philippe, A. Chappaz, P. Fongarland, A. Bengaouer, Power-to-Liquid catalytic CO_2 valorization into fuels and chemicals: focus on the Fischer-Tropsch route, Journal of CO_2 Utilization 38 (2020) 314-347.
[24] M.J. Bos, S.R.A. Kersten, D.W.F. Brilman, Wind power to methanol: Renewable methanol production using electricity, electrolysis of water and CO_2 air capture, Applied Energy 264 (2020) 114672.
[25] D. Hidalgo, J. Martín-Marroquín, Power-to-methane, coupling CO_2 capture with fuel production: An overview, Renewable and Sustainable Energy Reviews 132 (2020) 110057.
[26] P. Rentschler, C. Klahn, R. Dittmeyer, The Need for Dynamic Process Simulation: A Review of Offshore Power-to-X Systems, Chemie Ingenieur Technik 96 (2023) 114-125.
[27] V. Kyriakou, D. Neagu, E.I. Papaioannou, I.S. Metcalfe, M.C.M. van de Sanden, M.N. Tsampas, Co-electrolysis of H_2O and CO_2 on exsolved Ni nanoparticles for efficient syngas generation at controllable H_2/CO ratios, Applied Catalysis B: Environmental 258 (2019) 117950.
[28] S.R. Foit, I.C. Vinke, L.G.J. de Haart, R.A. Eichel, Power-to-Syngas: An Enabling Technology for the Transition of the Energy System?, Angew Chem Int Ed Engl 56 (2017) 5402-5411.
[29] J.-B. Vennekoetter, R. Sengpiel, M. Wessling, Beyond the catalyst: How electrode and reactor design determine the product spectrum during electrochemical CO_2 reduction, Chemical Engineering Journal 364 (2019) 89-101.
[30] D.T. Whipple, P.J.A. Kenis, Prospects of CO_2 Utilization via Direct Heterogeneous Electrochemical Reduction, The Journal of Physical Chemistry Letters 1 (2010) 3451-3458.
[31] S. Verma, S. Lu, P.J.A. Kenis, Co-electrolysis of CO_2 and glycerol as a pathway to carbon chemicals with improved technoeconomics due to low electricity consumption, Nature Energy 4 (2019) 466-474.
[32] R. Zhao, Y. Wang, G. Ji, J. Zhong, F. Zhang, M. Chen, S. Tong, P. Wang, Z. Wu, B. Han, Z. Liu, Partially Nitrided Ni Nanoclusters Achieve Energy-Efficient Electrocatalytic CO_2 Reduction to CO at Ultralow Overpotential, Advanced Materials 35 (2023) 2205262.
[33] Y. Kang, T. Kim, K.Y. Jung, K.T. Park, Recent Progress in Electrocatalytic CO_2 Reduction to Pure Formic Acid Using a Solid-State Electrolyte Device, Catalysts 13 (2023) 955.

[34] J. Fu, K. Liu, K. Jiang, H. Li, P. An, W. Li, N. Zhang, H. Li, X. Xu, H. Zhou, D. Tang, X. Wang, X. Qiu, M. Liu, Graphitic Carbon Nitride with Dopant Induced Charge Localization for Enhanced Photoreduction of CO_2 to CH_4, Advanced Science 6 (2019) 1900796.
[35] X. Wang, A. Xu, F. Li, S.F. Hung, D.H. Nam, C.M. Gabardo, Z. Wang, Y. Xu, A. Ozden, A.S. Rasouli, A.H. Ip, D. Sinton, E.H. Sargent, Efficient Methane Electrosynthesis Enabled by Tuning Local CO_2 Availability, J Am Chem Soc 142 (2020) 3525-3531.
[36] J. Zhao, Z. Chen, J. Zhao, Metal-free graphdiyne doped with sp-hybridized boron and nitrogen atoms at acetylenic sites for high-efficiency electroreduction of CO_2 to CH_4 and C_2H_4, Journal of Materials Chemistry A 7 (2019) 4026-4035.
[37] J. Li, A. Ozden, M. Wan, Y. Hu, F. Li, Y. Wang, R.R. Zamani, D. Ren, Z. Wang, Y. Xu, D.H. Nam, J. Wicks, B. Chen, X. Wang, M. Luo, M. Graetzel, F. Che, E.H. Sargent, D. Sinton, Silica-copper catalyst interfaces enable carbon-carbon coupling towards ethylene electrosynthesis, Nat Commun 12 (2021) 2808.
[38] H. Yang, Y. Wu, G. Li, Q. Lin, Q. Hu, Q. Zhang, J. Liu, C. He, Scalable Production of Efficient Single-Atom Copper Decorated Carbon Membranes for CO_2 Electroreduction to Methanol, J Am Chem Soc 141 (2019) 12717-12723.
[39] Y.C. Xiao, C.M. Gabardo, S. Liu, G. Lee, Y. Zhao, C.P. O'Brien, R.K. Miao, Y. Xu, J.P. Edwards, M. Fan, J.E. Huang, J. Li, P. Papangelakis, T. Alkayyali, A. Sedighian Rasouli, J. Zhang, E.H. Sargent, D. Sinton, Direct carbonate electrolysis into pure syngas, EES Catalysis 1 (2023) 54-61.
[40] F. Marques Mota, D.H. Kim, From CO_2 methanation to ambitious long-chain hydrocarbons: alternative fuels paving the path to sustainability, Chem Soc Rev 48 (2019) 205-259.
[41] J. Lin, Y. Zhang, P. Xu, L. Chen, CO_2 electrolysis: Advances and challenges in electrocatalyst engineering and reactor design, Materials Reports: Energy 3 (2023) 100194.
[42] Y. Pei, H. Zhong, F. Jin, A brief review of electrocatalytic reduction of CO2—Materials, reaction conditions, and devices, Energy Science & Engineering 9 (2021) 1012-1032.
[43] N. Du, C. Roy, R. Peach, M. Turnbull, S. Thiele, C. Bock, Anion-Exchange Membrane Water Electrolyzers, Chemical Reviews 122 (2022) 11830-11895.
[44] J. Park, Y.-j. Ko, C. Lim, H. Kim, B.K. Min, K.-Y. Lee, J.H. Koh, H.-S. Oh, W.H. Lee, Strategies for CO_2 electroreduction in cation exchange membrane electrode assembly, Chemical Engineering Journal 453 (2023) 139826.
[45] D.A. Salvatore, C.M. Gabardo, A. Reyes, C.P. O'Brien, S. Holdcroft, P. Pintauro, B. Bahar, M. Hickner, C. Bae, D. Sinton, E.H. Sargent, C.P. Berlinguette, Designing anion exchange membranes for CO_2 electrolysers, Nature Energy 6 (2021) 339-348.
[46] W. Yuan, Y. Ma, H. Wu, L. Cheng, Single-atom catalysts for CO oxidation, CO_2 reduction, and O_2 electrochemistry, Journal of Energy Chemistry 65 (2022) 254-279.
[47] S. Rasul, D.H. Anjum, A. Jedidi, Y. Minenkov, L. Cavallo, K. Takanabe, A highly selective copper-indium bimetallic electrocatalyst for the electrochemical reduction of aqueous CO_2 to CO, Angew Chem Int Ed Engl 54 (2015) 2146-2150.
[48] H. Zhong, K. Fujii, Y. Nakano, F. Jin, Effect of CO_2 bubbling into aqueous solutions used for electrochemical reduction of CO_2 for energy conversion and storage, The Journal of Physical Chemistry C 119 (2015) 55-61.
[49] L. Fan, C. Xia, F. Yang, J. Wang, H. Wang, Y. Lu, Strategies in catalysts and electrolyzer design for electrochemical CO_2 reduction toward C_{2+} products, Science Advance 6 (2020) eaay3111.
[50] A.D. Handoko, F. Wei, Jenndy, B.S. Yeo, Z.W. Seh, Understanding heterogeneous electrocatalytic carbon dioxide reduction through operando techniques, Nature Catalysis 1 (2018) 922-934.
[51] F. Pan, Y. Yang, Designing CO_2 reduction electrode materials by morphology and interface engineering, Energy & Environmental Science 13 (2020) 2275-2309.

[52] T. Zheng, M. Zhang, L. Wu, S. Guo, X. Liu, J. Zhao, W. Xue, J. Li, C. Liu, X. Li, Q. Jiang, J. Bao, J. Zeng, T. Yu, C. Xia, Upcycling CO_2 into energy-rich long-chain compounds via electrochemical and metabolic engineering, Nature Catalysis 5 (2022) 388-396.
[53] W. Lai, Y. Qiao, J. Zhang, Z. Lin, H. Huang, Design strategies for markedly enhancing energy efficiency in the electrocatalytic CO_2 reduction reaction, Energy & Environmental Science 15 (2022) 3603-3629.
[54] Z. Sun, T. Ma, H. Tao, Q. Fan, B. Han, Fundamentals and Challenges of Electrochemical CO_2 Reduction Using Two-Dimensional Materials, Chem 3 (2017) 560-587.
[55] S. Garg, M. Li, A.Z. Weber, L. Ge, L. Li, V. Rudolph, G. Wang, T.E. Rufford, Advances and challenges in electrochemical CO_2 reduction processes: an engineering and design perspective looking beyond new catalyst materials, Journal of Materials Chemistry A 8 (2020) 1511-1544.
[56] Y.Y. Birdja, E. Pérez-Gallent, M.C. Figueiredo, A.J. Göttle, F. Calle-Vallejo, M.T.M. Koper, Advances and challenges in understanding the electrocatalytic conversion of carbon dioxide to fuels, Nature Energy 4 (2019) 732-745.
[57] L. Li, X. Li, Y. Sun, Y. Xie, Rational design of electrocatalytic carbon dioxide reduction for a zero-carbon network, Chemical Society Reviews 51 (2022) 1234-1252.
[58] M.S. Sajna, S. Zavahir, A. Popelka, P. Kasak, A. Al-Sharshani, U. Onwusogh, M. Wang, H. Park, D.S. Han, Electrochemical system design for CO_2 conversion: A comprehensive review, Journal of Environmental Chemical Engineering 11 (2023) 110467.
[59] L. Wang, W. Chen, D. Zhang, Y. Du, R. Amal, S. Qiao, J. Wu, Z. Yin, Surface strategies for catalytic CO_2 reduction: from two-dimensional materials to nanoclusters to single atoms, Chem Soc Rev 48 (2019) 5310-5349.
[60] H. Zhou, K. Liu, H. Li, M. Cao, J. Fu, X. Gao, J. Hu, W. Li, H. Pan, J. Zhan, Q. Li, X. Qiu, M. Liu, Recent advances in different-dimension electrocatalysts for carbon dioxide reduction, J Colloid Interface Sci 550 (2019) 17-47.
[61] Y. Hori, H. Wakebe, T. Tsukamoto, O. Koga, Electrocatalytic Process of Co Selectivity in Electrochemical Reduction of CO_2 at Metal-Electrodes in Aqueous-Media, Electrochim Acta 39 (1994) 1833-1839.
[62] Q. Wang, K. Liu, K. Hu, C. Cai, H. Li, H. Li, M. Herran, Y.R. Lu, T.S. Chan, C. Ma, J. Fu, S. Zhang, Y. Liang, E. Cortes, M. Liu, Attenuating metal-substrate conjugation in atomically dispersed nickel catalysts for electroreduction of CO_2 to CO, Nat Commun 13 (2022) 6082.
[63] A. Bagger, W. Ju, A.S. Varela, P. Strasser, J. Rossmeisl, Electrochemical CO_2 Reduction: A Classification Problem, Chemphyschem 18 (2017) 3266-3273.
[64] C. Zhu, G. Wu, A. Chen, G. Feng, X. Dong, G. Li, S. Li, Y. Song, W. Wei, W. Chen, Selective CO_2 electroreduction to multicarbon products exceeding 2 A cm^{-2} in strong acids via a hollow-fiber Cu penetration electrode, Energy & Environmental Science 17 (2024) 510-517.
[65] Z. Chen, G. Yu, B. Li, X. Zhang, M. Jiao, N. Wang, X. Zhang, L. Liu, In Situ Carbon Encapsulation Confined Nickel-Doped Indium Oxide Nanocrystals for Boosting CO_2 Electroreduction to the Industrial Level, ACS Catalysis 11 (2021) 14596-14604.
[66] M.P.L. Kang, M.J. Kolb, F. Calle-Vallejo, B.S. Yeo, The Role of Undercoordinated Sites on Zinc Electrodes for CO_2 Reduction to CO, Advanced Functional Materials 32 (2022) 2111597.
[67] Y. Chen, Z. Fan, J. Wang, C. Ling, W. Niu, Z. Huang, G. Liu, B. Chen, Z. Lai, X. Liu, B. Li, Y. Zong, L. Gu, J. Wang, X. Wang, H. Zhang, Ethylene Selectivity in Electrocatalytic CO_2 Reduction on Cu Nanomaterials: A Crystal Phase-Dependent Study, J Am Chem Soc 142 (2020) 12760-12766.
[68] G.O. Larrazabal, V. Okatenko, I. Chorkendorff, R. Buonsanti, B. Seger, Investigation of Ethylene and Propylene Production from CO_2 Reduction over Copper Nanocubes in an MEA-Type Electrolyzer, ACS Applied Materials & Interfaces 14 (2022) 7779-7787.

[69] P. Grosse, D. Gao, F. Scholten, I. Sinev, H. Mistry, B. Roldan Cuenya, Dynamic Changes in the Structure, Chemical State and Catalytic Selectivity of Cu Nanocubes during CO_2 Electroreduction: Size and Support Effects, Angew Chem Int Ed Engl 57 (2018) 6192-6197.
[70] C. Du, J.P. Mills, A.G. Yohannes, W. Wei, L. Wang, S. Lu, J.X. Lian, M. Wang, T. Guo, X. Wang, H. Zhou, C.J. Sun, J.Z. Wen, B. Kendall, M. Couillard, H. Guo, Z. Tan, S. Siahrostami, Y.A. Wu, Cascade electrocatalysis via AgCu single-atom alloy and Ag nanoparticles in CO_2 electroreduction toward multicarbon products, Nat Commun 14 (2023) 6142.
[71] M.G. Kibria, C.T. Dinh, A. Seifitokaldani, P. De Luna, T. Burdyny, R. Quintero-Bermudez, M.B. Ross, O.S. Bushuyev, F.P. Garcia de Arquer, P. Yang, D. Sinton, E.H. Sargent, A Surface Reconstruction Route to High Productivity and Selectivity in CO_2 Electroreduction toward C_{2+} Hydrocarbons, Advanced Materials 30 (2018) e1804867.
[72] M. Esmaeilirad, Z. Jiang, A.M. Harzandi, A. Kondori, M. Tamadoni Saray, C.U. Segre, R. Shahbazian-Yassar, A.M. Rappe, M. Asadi, Imidazolium-functionalized Mo_3P nanoparticles with an ionomer coating for electrocatalytic reduction of CO_2 to propane, Nature Energy 8 (2023) 891-900.
[73] Y. Chen, X.Y. Li, Z. Chen, A. Ozden, J.E. Huang, P. Ou, J. Dong, J. Zhang, C. Tian, B.H. Lee, X. Wang, S. Liu, Q. Qu, S. Wang, Y. Xu, R.K. Miao, Y. Zhao, Y. Liu, C. Qiu, J. Abed, H. Liu, H. Shin, D. Wang, Y. Li, D. Sinton, E.H. Sargent, Efficient multicarbon formation in acidic CO_2 reduction via tandem electrocatalysis, Nature Nanotechnology 19 (2024) 311-318.
[74] Q. Hao, H.-x. Zhong, J.-z. Wang, K.-h. Liu, J.-m. Yan, Z.-h. Ren, N. Zhou, X. Zhao, H. Zhang, D.-x. Liu, X. Liu, L.-w. Chen, J. Luo, X.-b. Zhang, Nickel dual-atom sites for electrochemical carbon dioxide reduction, Nature Synthesis 1 (2022) 719-728.
[75] T. Jaster, A. Gawel, D. Siegmund, J. Holzmann, H. Lohmann, E. Klemm, U.P. Apfel, Electrochemical CO_2 reduction toward multicarbon alcohols - The microscopic world of catalysts & process conditions, iScience 25 (2022) 104010.
[76] Z. Xie, E. Huang, S. Garg, S. Hwang, P. Liu, J.G. Chen, CO_2 fixation into carbon nanofibres using electrochemical–thermochemical tandem catalysis, Nature Catalysis 7 (2024) 98-109.
[77] M. Jouny, W. Luc, F. Jiao, High-rate electroreduction of carbon monoxide to multi-carbon products, Nature Catalysis 1 (2018) 748-755.
[78] R.I. Masel, Z. Liu, H. Yang, J.J. Kaczur, D. Carrillo, S. Ren, D. Salvatore, C.P. Berlinguette, An industrial perspective on catalysts for low-temperature CO_2 electrolysis, Nat Nanotechnol 16 (2021) 118-128.
[79] S. Anantharaj, S. Kundu, S. Noda, "The Fe Effect": A review unveiling the critical roles of Fe in enhancing OER activity of Ni and Co based catalysts, Nano Energy 80 (2021) 105514.
[80] X. She, L. Zhai, Y. Wang, P. Xiong, M.M.-J. Li, T.-S. Wu, M.C. Wong, X. Guo, Z. Xu, H. Li, H. Xu, Y. Zhu, S.C.E. Tsang, S.P. Lau, Pure-water-fed, electrocatalytic CO_2 reduction to ethylene beyond 1,000 h stability at 10 A, Nature Energy 9 (2024) 81-91.
[81] J. Li, Y. Kuang, X. Zhang, W.-H. Hung, C.-Y. Chiang, G. Zhu, G. Chen, F. Wang, P. Liang, H. Dai, Electrochemical acetate production from high-pressure gaseous and liquid CO_2, Nature Catalysis 6 (2023) 1151-1163.
[82] T. Yan, X. Chen, L. Kumari, J. Lin, M. Li, Q. Fan, H. Chi, T.J. Meyer, S. Zhang, X. Ma, Multiscale CO_2 Electrocatalysis to C_{2+} Products: Reaction Mechanisms, Catalyst Design, and Device Fabrication, Chemical Reviews 123 (2023) 10530-10583.
[83] M. Heßelmann, H. Minten, T. Geissler, R.G. Keller, A. Bardow, M. Wessling, Why Membranes Matter: Ion Exchange Membranes in Holistic Process Optimization of Electrochemical CO_2 Reduction, Advanced Sustainable Systems 7 (2023) 2300077.

[84] A. Ozden, F.P.G. De Arquer, J.E. Huang, J. Wicks, J. Sisler, R.K. Miao, C.P. O'Brien, G. Lee, X. Wang, A.H. Ip, E.H. Sargent, D. Sinton, Carbon-efficient carbon dioxide electrolysers, Nature Sustainability 5 (2022) 563-573.
[85] E.W. Lees, B.A.W. Mowbray, F.G.L. Parlane, C.P. Berlinguette, Gas diffusion electrodes and membranes for CO_2 reduction electrolysers, Nature Reviews Materials 7 (2021) 55-64.
[86] Q. Ye, X. Zhao, R. Jin, F. Dong, H. Xie, B. Deng, Advances and challenges in membrane electrode assembly electrolyzers for CO_2 reduction, Journal of Materials Chemistry A 11 (2023) 21498-21515.
[87] M. Ramdin, A.R.T. Morrison, M. de Groen, R. van Haperen, R. de Kler, L.J.P. van den Broeke, J.P.M. Trusler, W. de Jong, T.J.H. Vlugt, High Pressure Electrochemical Reduction of CO_2 to Formic Acid/Formate: A Comparison between Bipolar Membranes and Cation Exchange Membranes, Industrial & Engineering Chemistry Research 58 (2019) 1834-1847.
[88] W. Wu, L. Xu, Q. Lu, J. Sun, Z. Xu, C. Song, J.C. Yu, Y. Wang, Addressing the Carbonate Issue: Electrocatalysts for Acidic CO_2 Reduction Reaction, Advanced Materials 37 (2025) 2312894.
[89] Z. Ma, Z. Yang, W. Lai, Q. Wang, Y. Qiao, H. Tao, C. Lian, M. Liu, C. Ma, A. Pan, H. Huang, CO_2 electroreduction to multicarbon products in strongly acidic electrolyte via synergistically modulating the local microenvironment, Nat Commun 13 (2022) 7596.
[90] E.K. Volk, M.E. Kreider, S. Kwon, S.M. Alia, Recent progress in understanding the catalyst layer in anion exchange membrane electrolyzers – durability, utilization, and integration, EES Catalysis 2 (2024) 109-137.
[91] F.P. Garcia de Arquer, C.T. Dinh, A. Ozden, J. Wicks, C. McCallum, A.R. Kirmani, D.H. Nam, C. Gabardo, A. Seifitokaldani, X. Wang, Y.C. Li, F. Li, J. Edwards, L.J. Richter, S.J. Thorpe, D. Sinton, E.H. Sargent, CO_2 electrolysis to multicarbon products at activities greater than 1 A cm^{-2}, Science 367 (2020) 661-666.
[92] C.T. Dinh, T. Burdyny, M.G. Kibria, A. Seifitokaldani, C.M. Gabardo, F.P. Garcia de Arquer, A. Kiani, J.P. Edwards, P. De Luna, O.S. Bushuyev, C. Zou, R. Quintero-Bermudez, Y. Pang, D. Sinton, E.H. Sargent, CO_2 electroreduction to ethylene via hydroxide-mediated copper catalysis at an abrupt interface, Science 360 (2018) 783-787.
[93] H. Shin, K.U. Hansen, F. Jiao, Techno-economic assessment of low-temperature carbon dioxide electrolysis, Nature Sustainability 4 (2021) 911-919.
[94] C. McCallum, C.M. Gabardo, C.P. O'Brien, J.P. Edwards, J. Wicks, Y. Xu, E.H. Sargent, D. Sinton, Reducing the crossover of carbonate and liquid products during carbon dioxide electroreduction, Cell Reports Physical Science 2 (2021) 100522.
[95] E.R. Cofell, U.O. Nwabara, S.S. Bhargava, D.E. Henckel, P.J.A. Kenis, Investigation of Electrolyte-Dependent Carbonate Formation on Gas Diffusion Electrodes for CO_2 Electrolysis, ACS Applied Materials & Interfaces 13 (2021) 15132-15142.
[96] N. Wang, R.K. Miao, G. Lee, A. Vomiero, D. Sinton, A.H. Ip, H. Liang, E.H. Sargent, Suppressing the liquid product crossover in electrochemical CO_2 reduction, SmartMat 2 (2021) 12-16.
[97] C.P. O'Brien, R.K. Miao, S. Liu, Y. Xu, G. Lee, A. Robb, J.E. Huang, K. Xie, K. Bertens, C.M. Gabardo, J.P. Edwards, C.-T. Dinh, E.H. Sargent, D. Sinton, Single Pass CO_2 Conversion Exceeding 85% in the Electrosynthesis of Multicarbon Products via Local CO_2 Regeneration, ACS Energy Letters 6 (2021) 2952-2959.
[98] A. Brunetti, E. Fontananova, CO_2 Conversion by Membrane Reactors, J Nanosci Nanotechnol 19 (2019) 3124-3134.
[99] L. Hu, X. Sai, X. Liu, Z. Chen, G. Wang, X. Yi, Influence of Environmental Conditions on Electrocatalytic CO_2 Reduction, ChemCatChem 16 (2024) e202301335.

[100] X. She, Y. Wang, H. Xu, S. Chi Edman Tsang, S. Ping Lau, Challenges and Opportunities in Electrocatalytic CO_2 Reduction to Chemicals and Fuels, Angew Chem Int Ed Engl 61 (2022) e202211396.
[101] R. Haaring, P.W. Kang, Z. Guo, J.W. Lee, H. Lee, Developing Catalysts Integrated in Gas-Diffusion Electrodes for CO_2 Electrolyzers, Acc Chem Res 56 (2023) 2595-2605.
[102] C.G. Vayenas, R.E. White, M.E. Gamboa-Aldeco, Modern aspects of electrochemistry 42, Springer Science & Business Media2008.
[103] T. Burdyny, W.A. Smith, CO_2 reduction on gas-diffusion electrodes and why catalytic performance must be assessed at commercially-relevant conditions, Energy & Environmental Science 12 (2019) 1442-1453.
[104] D. Higgins, C. Hahn, C. Xiang, T.F. Jaramillo, A.Z. Weber, Gas-Diffusion Electrodes for Carbon Dioxide Reduction: A New Paradigm, ACS Energy Letters 4 (2018) 317-324.
[105] B. Endrődi, G. Bencsik, F. Darvas, R. Jones, K. Rajeshwar, C. Janáky, Continuous-flow electroreduction of carbon dioxide, Progress in Energy and Combustion Science 62 (2017) 133-154.
[106] Z. Xing, K. Shi, X. Hu, X. Feng, Beyond catalytic materials: Controlling local gas/liquid environment in the catalyst layer for CO_2 electrolysis, Journal of Energy Chemistry 66 (2022) 45-51.
[107] Q. Xu, B.O. Joensen, N.C. Kani, A. Sartori, T. Willson, J.R. Varcoe, L. Riillo, A. Ramunni, J. Drnec, I. Chorkendorff, B. Seger, Electrolyte Effects in Membrane-Electrode-Assembly CO Electrolysis, Angew Chem Int Ed Engl 64 (2025) e202501505.
[108] P. Ganji, R.A. Borse, J. Xie, A.G.A. Mohamed, Y. Wang, Toward Commercial Carbon Dioxide Electrolysis, Advanced Sustainable Systems 4 (2020) 2000096.
[109] Y. Cheng, P. Hou, X. Wang, P. Kang, CO_2 Electrolysis System under Industrially Relevant Conditions, Acc Chem Res 55 (2022) 231-240.
[110] H. Yang, J.J. Kaczur, S.D. Sajjad, R.I. Masel, Electrochemical conversion of CO_2 to formic acid utilizing Sustainion™ membranes, Journal of CO_2 Utilization 20 (2017) 208-217.
[111] J.J. Kaczur, H. Yang, Z. Liu, S.D. Sajjad, R.I. Masel, Carbon Dioxide and Water Electrolysis Using New Alkaline Stable Anion Membranes, Front Chem 6 (2018) 263.
[112] D. Segets, C. Andronescu, U.P. Apfel, Accelerating CO_2 electrochemical conversion towards industrial implementation, Nature Communications 14 (2023) 7950.
[113] K. Ye, G. Zhang, X. Ma, C. Deng, X. Huang, C. Yuan, G. Meng, W. Cai, K. Jiang, Resolving local reaction environment toward an optimized CO_2-to-CO conversion performance, Energy & Environmental Science 15 (2022) 749-759.
[114] S.Y. Zhong, P.F. Sui, P. Holtappels, A. Navarrete, F.W. Li, R. Dittmeyer, Robust and efficient electroreduction of CO_2 to CO in a modified zero-gap electrochemical cell, Chemical Engineering Journal 244 (2025) 161119.
[115] Y.C. Tan, K.B. Lee, H. Song, J. Oh, Modulating Local CO_2 Concentration as a General Strategy for Enhancing C-C Coupling in CO_2 Electroreduction, Joule 4 (2020) 1104-1120.
[116] J. Choi, H. Lim, S. Surendran, S. Park, J. Shim, G.H. Jeong, U. Sim, Harnessing electrochemical CO_2 reduction and assisted water electrolysis via constrained thermodynamic modeling, Phys Chem Chem Phys 27 (2025) 17198-17211.
[117] A.J. Martín, G.O. Larrazábal, J. Pérez-Ramírez, Towards sustainable fuels and chemicals through the electrochemical reduction of CO2: lessons from water electrolysis, Green Chemistry 17 (2015) 5114-5130.
[118] W.H. Lee, Y.J. Ko, Y. Choi, S.Y. Lee, C.H. Choi, Y.J. Hwang, B.K. Min, P. Strasser, H.S. Oh, Highly selective and scalable CO to CO - Electrolysis using coral-nanostructured Ag catalysts in zero-gap configuration, Nano Energy 76 (2020) 105030.

[119] P.C. Chen, C. Chen, Y. Yang, A.L. Maulana, J. Jin, J. Feijoo, P. Yang, Chemical and Structural Evolution of AgCu Catalysts in Electrochemical CO_2 Reduction, J Am Chem Soc 145 (2023) 10116-10125.
[120] M.G. Kibria, J.P. Edwards, C.M. Gabardo, C.T. Dinh, A. Seifitokaldani, D. Sinton, E.H. Sargent, Electrochemical CO_2 Reduction into Chemical Feedstocks: From Mechanistic Electrocatalysis Models to System Design, Advanced Materials 31 (2019) 1807166.
[121] Y. Liang, F. Li, R.K. Miao, S. Hu, W. Ni, S. Zhang, Y. Liu, Y. Bai, H. Wan, P. Ou, X.-Y. Li, N. Wang, S. Park, F. Li, J. Zeng, D. Sinton, E.H. Sargent, Efficient ethylene electrosynthesis through C–O cleavage promoted by water dissociation, Nature Synthesis 3 (2024) 1104-1112.
[122] X. Wang, Z. Wang, T.T. Zhuang, C.T. Dinh, J. Li, D.H. Nam, F. Li, C.W. Huang, C.S. Tan, Z. Chen, M. Chi, C.M. Gabardo, A. Seifitokaldani, P. Todorovic, A. Proppe, Y. Pang, A.R. Kirmani, Y. Wang, A.H. Ip, L.J. Richter, B. Scheffel, A. Xu, S.C. Lo, S.O. Kelley, D. Sinton, E.H. Sargent, Efficient upgrading of CO to C_3 fuel using asymmetric C-C coupling active sites, Nature Communications 10 (2019) 5186.
[123] D. Dhamo, J. Kühn, S. Lüttin, M. Rubin, R. Dittmeyer, Coupling the high-temperature Fischer-Tropsch synthesis and the skeletal isomerization reaction at optimal operation conditions in the Power-to-Fuels process route for the production of sustainable aviation gasoline, Sustainable Energy & Fuels 8 (2024) 2094-2103.
[124] L. Weng, A.T. Bell, A.Z. Weber, Towards membrane-electrode assembly systems for CO_2 reduction: a modeling study, Energy & Environmental Science 12 (2019) 1950-1968.
[125] S. Brückner, Q. Feng, W. Ju, D. Galliani, A. Testolin, M. Klingenhof, S. Ott, P. Strasser, Design and diagnosis of high-performance CO_2-to-CO electrolyzer cells, Nature Chemical Engineering 1 (2024) 229-239.
[126] X. Zhao, H. Xie, B. Deng, L. Wang, Y. Li, F. Dong, Enhanced CO_2 reduction with hydrophobic cationic-ionomer layer-modified zero-gap MEA in acidic electrolyte, Chemical Communications 60 (2024) 542-545.
[127] R. Shi, J. Guo, X. Zhang, G.I.N. Waterhouse, Z. Han, Y. Zhao, L. Shang, C. Zhou, L. Jiang, T. Zhang, Efficient wettability-controlled electroreduction of CO_2 to CO at Au/C interfaces, Nature Communications 11 (2020) 3028.
[128] Z. Xing, L. Hu, D.S. Ripatti, X. Hu, X. Feng, Enhancing carbon dioxide gas-diffusion electrolysis by creating a hydrophobic catalyst microenvironment, Nature Communications 12 (2021) 136.
[129] Y. Zhong, X. Kong, Z. Song, Y. Liu, L. Peng, L. Zhang, X. Luo, J. Zeng, Z. Geng, Adjusting Local CO Confinement in Porous-Shell Ag@Cu Catalysts for Enhancing C-C Coupling toward CO_2 Eletroreduction, Nano Letters 22 (2022) 2554-2560.
[130] Y. Ma, W. Niu, W. Shi, X. Huang, Y. Liu, J. Chen, L. Xue, B. Zhang, Amorphous carbon coating enhances activity of high rate CO_2 electroreduction to CO, Journal of Materials Chemistry A 11 (2023) 12114-12120.
[131] H. Rabiee, L. Ge, X.Q. Zhang, S.H. Hu, M.R. Li, Z.G. Yuan, Gas diffusion electrodes (GDEs) for electrochemical reduction of carbon dioxide, carbon monoxide, and dinitrogen to value-added products: a review, Energy & Environmental Science 14 (2021) 1959-2008.
[132] W. Lee, Y.E. Kim, M.H. Youn, S.K. Jeong, K.T. Park, Catholyte-Free Electrocatalytic CO_2 Reduction to Formate, Angew Chem Int Ed Engl 57 (2018) 6883-6887.
[133] H.W. Shafaque, J.K. Lee, K. Krause, C. Lee, K.F. Fahy, P. Shrestha, M. Balakrishnan, A. Bazylak, Temperature enhances the ohmic and mass transport behaviour in membrane electrode assembly carbon dioxide electrolyzers, Energ Convers Manage 243 (2021) 114302.

[134] S. Garg, Q. Xu, A.B. Moss, M. Mirolo, W. Deng, I. Chorkendorff, J. Drnec, B. Seger, How alkali cations affect salt precipitation and CO_2 electrolysis performance in membrane electrode assembly electrolyzers, Energy & Environmental Science 16 (2023) 1631-1643.
[135] M. Ramdin, O.A. Moultos, L.J.P. van den Broeke, P. Gonugunta, P. Taheri, T.J.H. Vlugt, Carbonation in Low-Temperature CO_2 Electrolyzers: Causes, Consequences, and Solutions, Industrial & Engineering Chemistry Research 62 (2023) 6843-6864.
[136] A. Reyes, R.P. Jansonius, B.A.W. Mowbray, Y. Cao, D.G. Wheeler, J. Chau, D.J. Dvorak, C.P. Berlinguette, Managing Hydration at the Cathode Enables Efficient CO_2 Electrolysis at Commercially Relevant Current Densities, ACS Energy Letters 5 (2020) 1612-1618.
[137] K. Liu, W.A. Smith, T. Burdyny, Introductory Guide to Assembling and Operating Gas Diffusion Electrodes for Electrochemical CO_2 Reduction, ACS Energy Letters 4 (2019) 639-643.
[138] S. Lyu, L. Wang, Z. Li, S. Yin, J. Chen, Y. Zhang, J. Li, Y. Wang, Stabilization of epsilon-iron carbide as high-temperature catalyst under realistic Fischer-Tropsch synthesis conditions, Nature Communications 11 (2020) 6219.
[139] L. Huang, G. Gao, C. Yang, X.Y. Li, R.K. Miao, Y. Xue, K. Xie, P. Ou, C.T. Yavuz, Y. Han, G. Magnotti, D. Sinton, E.H. Sargent, X. Lu, Pressure dependence in aqueous-based electrochemical CO_2 reduction, Nature Communications 14 (2023) 2958.
[140] N.C. Kani, S. Olusegun, R. Chauhan, J.A. Gauthier, M.R. Singh, High-pressure electrochemistry: a new frontier in decarbonization, EES Catalysis 2 (2024) 507-521.
[141] C.-T. Dinh, F.P. García de Arquer, D. Sinton, E.H. Sargent, High Rate, Selective, and Stable Electroreduction of CO_2 to CO in Basic and Neutral Media, ACS Energy Letters 3 (2018) 2835-2840.
[142] M. Sassenburg, M. Kelly, S. Subramanian, W.A. Smith, T. Burdyny, Zero-Gap Electrochemical CO_2 Reduction Cells: Challenges and Operational Strategies for Prevention of Salt Precipitation, ACS Energy Letters 8 (2023) 321-331.
[143] G. Wen, B. Ren, X. Wang, D. Luo, H. Dou, Y. Zheng, R. Gao, J. Gostick, A. Yu, Z. Chen, Continuous CO_2 electrolysis using a CO_2 exsolution-induced flow cell, Nature Energy 7 (2022) 978-988.
[144] J. Disch, L. Bohn, L. Metzler, S. Vierrath, Strategies for the mitigation of salt precipitation in zero-gap CO_2 electrolyzers producing CO, Journal of Materials Chemistry A 11 (2023) 7344-7357.
[145] C.M. Gabardo, C.P. O'Brien, J.P. Edwards, C. McCallum, Y. Xu, C.T. Dinh, J. Li, E.H. Sargent, D. Sinton, Continuous Carbon Dioxide Electroreduction to Concentrated Multi-carbon Products Using a Membrane Electrode Assembly, Joule 3 (2019) 2777-2791.
[146] S.D. Ebbesen, S.H. Jensen, A. Hauch, M.B. Mogensen, High temperature electrolysis in alkaline cells, solid proton conducting cells, and solid oxide cells, Chemical Reviews 114 (2014) 10697-10734.
[147] G.A. El-Nagar, F. Haun, S. Gupta, S. Stojkovikj, M.T. Mayer, Unintended cation crossover influences CO_2 reduction selectivity in Cu-based zero-gap electrolysers, Nature Communications 14 (2023) 2062.
[148] D.F. Gao, R.M. Arán-Ais, H.S. Jeon, B. Roldan Cuenya, Rational catalyst and electrolyte design for CO_2 electroreduction towards multicarbon products, Nature Catalysis 2 (2019) 198-210.
[149] A. Xu, N. Govindarajan, G. Kastlunger, S. Vijay, K. Chan, Theories for Electrolyte Effects in CO_2 Electroreduction, Acc Chem Res 55 (2022) 495-503.
[150] J.H. Montoya, C. Shi, K. Chan, J.K. Norskov, Theoretical Insights into a CO Dimerization Mechanism in CO_2 Electroreduction, J Phys Chem Lett 6 (2015) 2032-2037.

[151] A.S. Varela, W. Ju, A. Bagger, P. Franco, J. Rossmeisl, P. Strasser, Electrochemical Reduction of CO_2 on Metal-Nitrogen-Doped Carbon Catalysts, ACS Catalysis 9 (2019) 7270-7284.
[152] Y. Zheng, A. Vasileff, X. Zhou, Y. Jiao, M. Jaroniec, S.Z. Qiao, Understanding the Roadmap for Electrochemical Reduction of CO_2 to Multi-Carbon Oxygenates and Hydrocarbons on Copper-Based Catalysts, J Am Chem Soc 141 (2019) 7646-7659.
[153] S. Nitopi, E. Bertheussen, S.B. Scott, X. Liu, A.K. Engstfeld, S. Horch, B. Seger, I.E.L. Stephens, K. Chan, C. Hahn, J.K. Norskov, T.F. Jaramillo, I. Chorkendorff, Progress and Perspectives of Electrochemical CO_2 Reduction on Copper in Aqueous Electrolyte, Chem Rev 119 (2019) 7610-7672.
[154] J.Y.T. Kim, C. Sellers, S. Hao, T.P. Senftle, H. Wang, Different distributions of multi-carbon products in CO_2 and CO electroreduction under practical reaction conditions, Nature Catalysis 6 (2023) 1115-1124.
[155] K. Qi, Y. Zhang, N. Onofrio, E. Petit, X. Cui, J. Ma, J. Fan, H. Wu, W. Wang, J. Li, J. Liu, Y. Zhang, Y. Wang, G. Jia, J. Wu, L. Lajaunie, C. Salameh, D. Voiry, Unlocking direct CO_2 electrolysis to C_3 products via electrolyte supersaturation, Nature Catalysis 6 (2023) 319-331.
[156] A. Gawel, T. Jaster, D. Siegmund, J. Holzmann, H. Lohmann, E. Klemm, U.P. Apfel, Electrochemical CO_2 reduction - The macroscopic world of electrode design, reactor concepts & economic aspects, iScience 25 (2022) 104011.
[157] Z.Z. Niu, F.Y. Gao, X.L. Zhang, P.P. Yang, R. Liu, L.P. Chi, Z.Z. Wu, S. Qin, X. Yu, M.R. Gao, Hierarchical Copper with Inherent Hydrophobicity Mitigates Electrode Flooding for High-Rate CO_2 Electroreduction to Multicarbon Products, Journal of the American Chemical Society 143 (2021) 8011-8021.
[158] M. Wang, L. Lin, Z. Zheng, Z. Jiao, W. Hua, G. Wang, X. Ke, Y. Lian, F. Lyu, J. Zhong, Z. Deng, Y. Peng, Hydrophobized electrospun nanofibers of hierarchical porosity as the integral gas diffusion electrode for full-pH CO_2 electroreduction in membrane electrode assemblies, Energy & Environmental Science 16 (2023) 4423-4431.
[159] B. Endrődi, E. Kecsenovity, A. Samu, T. Halmágyi, S. Rojas-Carbonell, L. Wang, Y. Yan, C. Janáky, High carbonate ion conductance of a robust PiperION membrane allows industrial current density and conversion in a zero-gap carbon dioxide electrolyzer cell, Energy & Environmental Science 13 (2020) 4098-4105.
[160] B. Endrodi, E. Kecsenovity, A. Samu, F. Darvas, R.V. Jones, V. Torok, A. Danyi, C. Janaky, Multilayer Electrolyzer Stack Converts Carbon Dioxide to Gas Products at High Pressure with High Efficiency, ACS Energy Letters 4 (2019) 1770-1777.
[161] D. Mardiansyah, T. Badloe, K. Triyana, M.Q. Mehmood, N. Raeis-Hosseini, Y. Lee, H. Sabarman, K. Kim, J. Rho, Effect of temperature on the oxidation of Cu nanowires and development of an easy to produce, oxidation-resistant transparent conducting electrode using a PEDOT:PSS coating, Scientific Reports 8 (2018) 10639.
[162] V.D.B.C. Dasireddy, S.Š. Neja, L. Blaž, Correlation between synthesis pH, structure and $Cu/MgO/Al_2O_3$ heterogeneous catalyst activity and selectivity in CO_2 hydrogenation to methanol, Journal of CO_2 Utilization 28 (2018) 189-199.
[163] C. Han, L. Ge, C. Chen, Y. Li, Z. Zhao, X. Xiao, Z. Li, J. Zhang, Site-selected synthesis of novel Ag@AgCl nanoframes with efficient visible light induced photocatalytic activity, Journal of Materials Chemistry A 2 (2014) 12594-12600.
[164] R.E. Vos, K.E. Kolmeijer, T.S. Jacobs, W. van der Stam, B.M. Weckhuysen, M.T.M. Koper, How Temperature Affects the Selectivity of the Electrochemical CO_2 Reduction on Copper, ACS Catalysis 13 (2023) 8080-8091.
[165] A.M.P. Sakita, E.A. Ticianelli, The role of cation exchange membrane characteristics in CO_2 electrolysis to CO using acid anolyte, Electrochim Acta 509 (2025) 145308.

[166] M.G. Ha, C. Lim, C. Oh, H. Kim, J.-Y. Choi, W.H. Lee, H.-S. Oh, Efficient and durable porous Membrane-Based CO_2 electrolysis for commercial Zero-Gap electrolyzer stack systems, Chemical Engineering Journal 496 (2024) 154060.
[167] D. Hursan, C. Janaky, Operando characterization of continuous flow CO_2 electrolyzers: current status and future prospects, Chemical Communications 59 (2023) 1395-1414.
[168] R. Qiu, J. Jia, L. Peng, R. Li, S. Yan, J. Li, J. Zhang, D.T. Sun, Z. Lan, T. Xue, G. Xu, L. Cui, Z. Lv, C. Li, Y. Hong, Y. Guo, B. Ren, S. Yang, J. Li, B. Han, Enhanced electroreduction of CO_2 to ethanol via enriched intermediates at high CO_2 pressures, Green Chemistry 25 (2023) 684-691.
[169] J. Li, Y. Kuang, Y. Meng, X. Tian, W.H. Hung, X. Zhang, A. Li, M. Xu, W. Zhou, C.S. Ku, C.Y. Chiang, G. Zhu, J. Guo, X. Sun, H. Dai, Electroreduction of CO_2 to Formate on a Copper-Based Electrocatalyst at High Pressures with High Energy Conversion Efficiency, Journal of the American Chemical Society 142 (2020) 7276-7282.
[170] E.J. Dufek, T.E. Lister, S.G. Stone, M.E. McIlwain, Operation of a Pressurized System for Continuous Reduction of CO_2, Journal of The Electrochemical Society 159 (2012) F514-F517.
[171] Y. Chen, T. Ma, F. Wang, Y. Liu, Effect of Pressure on the Gas Diffusion Electrodes during CO_2 Reduction Reaction, Industrial & Engineering Chemistry Research 63 (2024) 15546-15553.
[172] D.G. Wheeler, B.A.W. Mowbray, A. Reyes, F. Habibzadeh, J.F. He, C.P. Berlinguette, Quantification of water transport in a CO_2 electrolyzer, Energy & Environmental Science 13 (2020) 5126-5134.
[173] S. Messias, M.M. Sousa, M. Nunes da Ponte, C.M. Rangel, T. Pardal, A.S. Reis Machado, Electrochemical production of syngas from CO_2 at pressures up to 30 bar in electrolytes containing ionic liquid, Reaction Chemistry & Engineering 4 (2019) 1982-1990.
[174] T. Li, M. Shao, A minireview on electrochemical CO_2 conversion based on carbonate/bicarbonate media, EES Catalysis 2 (2024) 564-572.
[175] A.S. Varela, M. Kroschel, T. Reier, P. Strasser, Controlling the selectivity of CO_2 electroreduction on copper: The effect of the electrolyte concentration and the importance of the local pH, Catalysis Today 260 (2016) 8-13.
[176] G. Kastlunger, H.H. Heenen, N. Govindarajan, Combining First-Principles Kinetics and Experimental Data to Establish Guidelines for Product Selectivity in Electrochemical CO_2 Reduction, ACS Catalysis 13 (2023) 5062-5072.
[177] C. Chen, Y. Li, S. Yu, S. Louisia, J. Jin, M. Li, M.B. Ross, P. Yang, Cu-Ag Tandem Catalysts for High-Rate CO_2 Electrolysis toward Multicarbons, Joule 4 (2020) 1688-1699.
[178] S.Y. Zhong, W.W. Yang, S.D. Liu, R. Dittmeyer, Synergistic electroreduction of CO_2 to C_1-C_3 gas products in a pressure-tolerant MEA system, International Journal of Hydrogen Energy 119 (2025) 73-81.
[179] D.L.T. Nguyen, Y. Kim, Y.J. Hwang, D.H. Won, Progress in development of electrocatalyst for CO_2 conversion to selective CO production, Carbon Energy 2 (2019) 72-98.
[180] C. Martens, B. Schmid, H. Tempel, R.-A. Eichel, CO_2 flow electrolysis – limiting impact of heat and gas evolution in the electrolyte gap on current density, Green Chemistry 25 (2023) 7794-7806.
[181] S. Hernandez-Aldave, E. Andreoli, Fundamentals of Gas Diffusion Electrodes and Electrolysers for Carbon Dioxide Utilisation: Challenges and Opportunities, Catalysts 10 (2020) 713.
[182] S. Hao, A. Elgazzar, S.K. Zhang, T.U. Wi, F.Y. Chen, Y. Feng, P. Zhu, H. Wang, Acid-humidified CO_2 gas input for stable electrochemical CO_2 reduction reaction, Science 388 (2025) 1182.
[183] S. Zhong, I. Ait Aissa, G. Huang, P. Holtappels, S. Liu, R. Dittmeyer, Experimental study of operating parameters in zero-gap CO_2 electrolysis, Frontiers in Catalysis 5 (2025).

[184] I. Sullivan, A. Goryachev, I.A. Digdaya, X. Li, H.A. Atwater, D.A. Vermaas, C. Xiang, Coupling electrochemical CO_2 conversion with CO_2 capture, Nature Catalysis 4 (2021) 952-958.
[185] Y. Song, X. Zhang, K. Xie, G. Wang, X. Bao, High-Temperature CO_2 Electrolysis in Solid Oxide Electrolysis Cells: Developments, Challenges, and Prospects, Advanced Materials (2019) 1902033.
[186] M. Baudy, O. Rondeau, A. Jaafar, C. Turpin, S. Abbou, M. Grignon, A. Escande, S. Rigal, Methodology for readjusting the voltage according to the operating conditions of a high temperature proton exchange membrane fuel cell, 2021 International Conference on Electrical, Computer and Energy Technologies (ICECET), 2021, pp. 1-6.
[187] D. Vivona, A. Casalegno, A. Baricci, Validation of a pseudo 2D analytical model for high temperature PEM fuel cell impedance valid at typical operative conditions, Electrochim Acta 310 (2019) 122-135.
[188] P. Ribeirinha, M. Abdollahzadeh, A. Pereira, F. Relvas, M. Boaventura, A. Mendes, High temperature PEM fuel cell integrated with a cellular membrane methanol steam reformer: Experimental and modelling, Applied Energy 215 (2018) 659-669.
[189] M. Liu, M. Liu, X. Wang, S.M. Kozlov, Z. Cao, P. De Luna, H. Li, X. Qiu, K. Liu, J. Hu, C. Jia, P. Wang, H. Zhou, J. He, M. Zhong, X. Lan, Y. Zhou, Z. Wang, J. Li, A. Seifitokaldani, C.T. Dinh, H. Liang, C. Zou, D. Zhang, Y. Yang, T.-S. Chan, Y. Han, L. Cavallo, T.-K. Sham, B.-J. Hwang, E.H. Sargent, Quantum-Dot-Derived Catalysts for CO_2 Reduction Reaction, Joule 3 (2019) 1703-1718.
[190] P. De Luna, R. Quintero-Bermudez, C.-T. Dinh, M.B. Ross, O.S. Bushuyev, P. Todorović, T. Regier, S.O. Kelley, P. Yang, E.H. Sargent, Catalyst electro-redeposition controls morphology and oxidation state for selective carbon dioxide reduction, Nature Catalysis 1 (2018) 103-110.

Publications

1. **S. Zhong**, P. Sui, P. Holtappels, A. Navarrete, F. Li, R. Dittmeyer, Robust and efficient electroreduction of CO_2 to CO in a modified zero-gap electrochemical cell, *Chemical Engineering Journal* 509 (2025) 161119.
2. **S. Zhong**, W. Yang, S. Liu, R. Dittmeyer, Synergistic electroreduction of CO_2 to C_1-C_3 gas products in a pressure-tolerant MEA system, *International Journal of Hydrogen Energy* 119 (2025) 73-81.
3. **S. Zhong**, I. Aissa, G. Huang, P. Holtappels, S. Liu, R. Dittmeyer, Experimental study of operating conditions affecting CO_2 electrolysis performance in a zero-gap electrolyzer, *Frontiers in Catalysis* 5 (2025).